

UNIVERSITÀ DEGLI STUDI DELLA TUSCIA DI VITERBO

DIPARTIMENTO DI SCIENZE AGRARIE E FORESTALI

Corso di Dottorato di Ricerca in

Ecosistemi e Sistemi Produttivi –XXIX° Ciclo.

**INTERMEDIATE TEMPERATURE SOLID OXIDE FUEL CELLS FED WITH SYNGAS: AN EVALUATION
OF ELECTROCHEMICAL PHENOMENA**

s.s.d. ING-IND/09

Tesi di dottorato di:

Dott. Davide Pumiglia

Coordinatore del corso

Prof. Alessandro Sorrentino

Tutore

Prof. Maurizio Carlini

Co-tutore

Dott. Stephen J. McPhail

A. A. 2016/2017

ABSTRACT

One of the most interesting features of Solid Oxide Fuel Cells (SOFCs) is the capability to produce electrical and thermal energy starting from syngas sources, such as the gasification of biomass or the reforming of natural gas, with uncommonly high efficiencies.

Stable and safe operation of SOFC systems fed with syngas is currently an issue, under determined operating conditions, the endurance performance of the cell can be hindered, even to the point of critical failure. The number and the complexity of the intertwined chemical, electrochemical and thermo-fluid dynamic mechanisms driving the energy conversion of syngas into electrical power and heat call for more accurate analysis tools and techniques so as to correctly address the role of these mechanisms in the immediate and endurance performance, and thus going beyond the state-of-art.

An in-depth characterization of the processes occurring within SOFCs operating with syngas has been achieved by means of homogeneous testing protocols, innovative testing equipment and complex analysis methods, some of them applied while *in operando*.

The Distribution of Relaxation Times (DRT) method applied to Electrochemical Impedance Spectroscopy (EIS) measurements carried out over a wide range of operating conditions allowed the recognition of the single physicochemical processes and their contribution to the overall performances, the estimation of parameters related to the different processes, and the evaluation of degradation effects caused by a long operation of SOFC fed with clean and contaminated syngas.

Measurements with an innovative, in-house built experimental set-up, allowing to perform localized sampling of gas compositions and temperatures directly *in operando* have been realized, optimized and employed in the study of the thermal and concentration gradients arising along the anode surface. Chemical and thermal mapping of the anode surface have been obtained under different operating conditions, both with hydrogen and syngas fuels, highlighting the evolution, the competition and the impact of the different reactions with a spatial resolution.

The obtained results provide an in-depth picture of the most important factors affecting the overall performances of syngas-fed SOFC cells, opening new perspectives for the investigation of SOFC systems.

ACKNOWLEDGEMENTS

The work hereby presented, that concludes my PhD course, could not have been taken shape without the contribution of those who guided, accompanied and supported me throughout this long path.

First and foremost, I would like to thank my supervisor, Prof. Maurizio Carlini, for giving me this opportunity and for his essential support during the entire PhD course.

I am deeply grateful to Dr. Eng. Stephen J. McPhail who, as my co-supervisor, mentor and friend, has promoted my professional and personal development with constant and unconditioned trust.

I would also like to thank all ENEA researchers I have had the pleasure to collaborate with, for their precious contributions to this work.

To my PhD colleague and childhood friend Andrea, who has shown me how good friends always get together again.

To my colleagues, to have shared with me joy and sorrow of the lab but, above all, because I have found in you more than just good colleagues, I have found precious friends.

To all of my friends, old and new, for having sustained and borne me: now that I would like to thank you one by one, I realize that you are so many, that I am really lucky for having you in my life, and that I am too lazy to write something profound for each one of you!

To my family, for sustaining and trusting me every day during these last years, as you have done for every day of my life.

Contents

1. INTRODUCTION	10
1.1. Goals of this work	11
1.2. Outline	12
2. FUNDAMENTALS	13
2.1. Operating principles of Solid Oxide Fuel Cells	13
2.1.1. Cell potential	14
2.1.2. Electrochemical losses	16
2.2. Materials and Design	20
2.2.1. Electrolyte	21
2.2.2. Anode	22
2.2.3. Cathode	23
2.2.4. Interconnects	24
2.2.5. Sealants	25
2.2.6. Tubular SOFCs	25
2.2.7. Planar SOFCs	26
2.3. Fuel Flexibility	28
2.3.1. Non-conventional Fuels: syngas	29
2.3.2. Operation of SOFC with syngas	30
2.3.3. Fuel impurities	32
3. ANALYSIS TOOLS AND TECHNIQUES	34
3.1. Polarization curves	34
3.2. Electrochemical Impedance Spectroscopy (EIS)	35
3.2.1. Principles of EIS	35
3.2.2. EIS measurements on SOFCs	36
3.3. Distribution of Relaxation Times (DRT) method: deconvolution of signals	38
3.4. Complex Non-linear Least Squares (CNLS) fit	43
3.4.1. Equivalent circuit elements	44

3.4.2. Fitting strategy based on DRT	47
3.5. Other characterization techniques	51
4. EXPERIMENTAL MATERIALS, METHODS AND PROCEDURES	54
4.1. Tested samples	54
4.2. Button cell test station	56
4.3. Multisampling cell housing	57
4.3.1. Design and Realization	57
4.3.2. Materials and Manufacturing	58
4.3.3. Placement and role of components	60
4.3.4. SOFC cell assembly	62
4.4. Single cell test station	64
4.5. Preliminary testing procedures	65
4.5.1. Button cells	65
4.5.2. Single cells	66
4.6. Button cells testing conditions	67
4.6.1. Process identification	67
4.6.2. Endurance performance in syngas	70
4.6.3. Tar contamination	70
4.7. Single cell testing conditions	71
4.7.1. Validation of the multisampling set-up	71
4.7.2. Hydrogen operation	72
4.7.3. Syngas operation	73
5. RESULTS AND DISCUSSION	75
5.1. Process identification	76
5.1.1. Fuel comparison	77
5.1.2. H ₂ /H ₂ O operation	78
5.1.3. CO/CO ₂ operation	80
5.1.4. Syngas operation	82
5.1.5. Oxygen variation	84
5.1.6. Current load variation	85
5.1.7. Resume of the identified processes	87
5.2. Estimation of operating parameters	88

5.2.1. H ₂ /H ₂ O operation	90
5.2.2. CO/CO ₂ operation	101
5.2.3. Syngas operation	109
5.2.4. Resume of the estimated parameters	115
5.3. Endurance performance in syngas	117
5.3.1. Degradation of cell performances	117
5.3.2. Post-mortem analysis	120
5.3.3. Resume of endurance performances in syngas	122
5.4. Tar contamination	123
5.4.1. Effects of tar concentration	123
5.4.2. Degradation of cell performances	126
5.4.3. Post-mortem analysis	130
5.4.4. Resume of tar contamination	134
5.5. Reactions evolution on anode surface	135
5.5.1. Validation of the multisampling set-up	137
5.5.2. Hydrogen operation	138
5.5.3. Syngas Operation	141
5.5.4. Resume of the reactions evolution on anode surface	146
6. CONCLUSIONS	148
PUBLICATIONS	152
BIBLIOGRAPHY	155

1. INTRODUCTION

Within the recent global efforts to develop a new energy production and distribution market based on the reduction of green house gas emissions¹, reduction of the consumption of fossil fuels, increased generation of power and heat from renewable sources, and enhancement of the energy conversion and distribution efficiency², electrochemical power generating systems such as fuel cells are driving in the last 20 years an increasing attention. Among the broad range of fuel cell typologies, Solid Oxide Fuel Cells (SOFCs) result the most promising in terms of global heat and power conversion efficiencies, wide range of applicability and cost effectiveness^{3, 4}.

In contrast to most traditional powering systems such as turbines and internal combustion engines, and more so than other fuel cell types, SOFC technology-based devices exhibit high efficiencies regardless of the scale⁵. This technology stands out over the rest of its competitors also due to a number of valuable properties. Besides insignificant emissions of NO_x, SO_x and particulate matter, very reduced CO₂ emissions (only in the case of hydrocarbon fuels), silent and vibration free operation, the most outstanding property is its fuel flexibility⁶, which makes SOFCs attractive for their application with non-conventional fuels, cheaper and more accessible than pure H₂.

In fact, thanks to the high operating temperatures (ranging between 600 and 1000°C) and due to the presence of a metal catalyst (generally Ni), the production of electricity and heat may be realized with uncommonly high efficiencies starting from carbon-based fuels, such as natural gas and hydrocarbon fuels, but also from those fuels like syngas and bio-syngas generated from the gasification of coal or biomasses, or from the anaerobic digestion of organic wastes, thus making this technology a fundamental pillar of a novel energy market based on the waste to energy chain⁷.

Nevertheless, to make this technology competitive with other power generating systems currently present in the market, the next generation of SOFC-based systems must fulfil two important goals: an increased life-span and a considerable reduction of production costs⁸.

To achieve these tasks, it is mandatory to have access to a deep comprehension of all the mechanisms occurring within a SOFC while in operation, especially when this device is fed with complex multi-component fuels such as syngas and bio-syngas, where the number of chemical

and electrochemical reactions that affect the heat and power generation, and the physical quantities that regulate them, increase.

The possibility to measure physical quantities directly *in operando*, opens new possibilities to achieve the required characteristics for this technology to enter the energy market in an effective way, by developing new generations of cells based on novel materials and morphologies, tailor the operating conditions to achieve longer and safe operation, especially with carbon-containing fuels such as syngas and bio-syngas, and develop new and reliable predictive computational models based on experimental data able to predict the performance of the fuel cell over a broad range of operative conditions (temperature, pressure, gas composition), and experimentally validate their results.

1.1. Goals of this work

The main goal of this work is to deeply investigate the chemical and electrochemical processes occurring during the operation of a new generation of SOFC, Intermediate Temperature Solid Oxide Fuel Cells, when fed with different syngas compositions.

To do so, along with conventional characterization techniques such as polarization curves and electrochemical impedance spectroscopy (EIS), novel analysis tools and techniques are presented, developed and employed in this work: the first one is a deconvolution method for EIS measurements known as Distribution of Relaxation Times (DRT), that allows a clear identification of the single processes contributing to the overall polarization losses of the cell. The second one is an innovative, in-house built, multisampling set-up which allows the contemporaneous measurements of gas compositions and temperatures with a spatial resolution along the anode surface, making it possible to study the evolution of all the reactions occurring at the fuel electrode and investigating the concentration and thermal gradient arising at different operating conditions.

By means of these two advanced investigating tools, a number of different aspects of the coupling of syngas fuels with IT-SOFC systems were studied, resulting in an in-depth comprehension of the single physicochemical processes and their effect on the overall performances, of the thermal and chemical gradients arising during the operation, and of the degradation effects caused by a long operation with clean and contaminated syngas.. The contents of this doctoral thesis are resumed in the following Section.

1.2. Outline

In this work, an initial description of the operating principles of SOFCs, general aspects about the materials and designs related to this technology, and applicability with carbon-based fuels are briefly resumed in Chapter 2.

In Chapter 3 a description of the principal characterization techniques employed in this work is provided, with particular attention dedicated to the novel DRT methodology and all its useful implications in the analysis of the EIS measurements.

The experimental campaigns, the testing procedures, the characteristics of the samples, and the experimental apparatus employed are reported in Chapter 4; within this chapter, the novel multisampling housing developed in-house is described in detail, along with the details of the experimental campaign carried out with it.

In Chapter 5, the experimental results and the discussions related to them are widely reported. In particular, in the first part, the DRT methodology demonstrated to be extremely instrumental in the qualitative separation of all the processes that contribute to the polarization losses within an IT-SOFC fed with three different types of fuels: humidified hydrogen, carbon monoxide, and syngas. Starting from these results, an accurate equivalent circuit model (ECM) was defined and employed in a CNLS fitting procedure over the broad range of experimental spectra collected in different operating conditions, allowing to obtain a set of operating parameters for the three types of fuel employed. The same methodology was then employed in the study of the endurance performances of an IT-SOFC sample fed with a clean syngas, and in the investigations of the poisoning effects of a tar contaminant in the fuel stream.

In the second part, the novel multisampling set-up has been first validated in terms of the cell's immediate performances, and then was employed in the study of the surface evolution of the reactions at the anode side in both dry H₂ and simulated syngas composition coming from the external steam reforming of natural gas, highlighting interesting aspects about the generation of local thermo-chemical gradients and about the competitiveness of the different reactions with syngas fuel, depending on the operating conditions.

Finally in Chapter 6, the results obtained from the experimental investigations are resumed and some conclusions are provided.

2. FUNDAMENTALS

The fundamental aspects of the operating principles of a generic SOFC are summarized in this chapter, with particular attention to those concepts that will be instrumental for the explanation of the experimental results within this work. In particular more details will be provided on the electrochemical loss mechanisms of SOFCs, and on the main reactions and mechanisms occurring in SOFCs fed with non conventional fuels. For more detailed information about the general operating principles of SOFC, the reader is referred to the relevant handbooks^{9, 10, 11}.

2.1. Operating principles of Solid Oxide Fuel Cells

Solid oxide fuel cells are electrochemical devices that promote electrochemical conversion of the energy content of a fuel, the most common being H_2 , directly to electrical and thermal energy, avoiding the intermediate steps of combustion – thermal energy – mechanical energy – electrical energy, that are present in conventional power generating systems based on internal combustion engines.

In Figure 2.1 a schematic representation of the principal mechanism of operation of a solid oxide fuel cell is depicted. In this representation, it is considered that only pure H_2 is provided to the anode (negative electrode) and air is provided at the cathode (positive electrode).

The fuel (H_2) flows through the porous structure of the anode, and reaches the interface with the electrolyte. In the region known as triple phase boundary (TPB), where the gas, the electronic conducting phase (metal catalyst) and the ionic conducting phase meet, the hydrogen is oxidized at the catalytic active sites to water (H_2O) by the oxygen ions (O^{2-}) coming from the electrolyte layer, releasing 2 electrons (e^-) to the external circuit. The electrons are then transferred to the cathode side, where they reduce the oxygen present in the air. Thanks to peculiar properties of the cathode materials (explained in the following Section), the O^{2-} ions pass through the cathode layer and reach the electrolyte layer which, being a ionic conductor, move the O^{2-} ions to the TPB region, where they are ready for the oxidation of the incoming fuel.

What is explained above can be easily summarized considering the electrochemical semi-reactions occurring at the anode and at the cathode side:

When H_2 is used as a fuel, the anode semi-reaction is described by means of Equation 2.1.



At the cathode of an SOFC the reduction of oxygen into its anion can be expressed as:



The overall electrochemical reaction for the conversion of the fuel to its product is expressed as a sum of the two previous semi-reactions, giving in turn Equation 2.3:

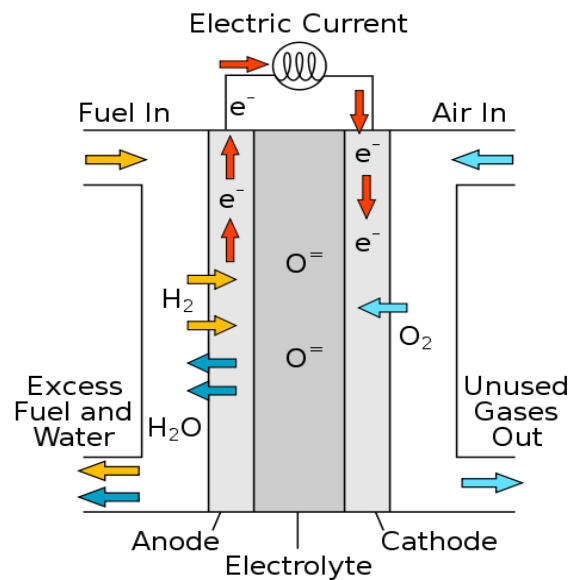


Figure 2.1 – Schematic representation of a solid oxide fuel cell operating mechanism, considering the oxidation reaction of H_2 .

2.1.1. Cell potential

The maximum potential difference in a fuel cell is given by the reversible cell potential, which is obtained under thermodynamically reversible conditions.

Consider the generic reaction:



where a, b, c and d are the stoichiometric coefficients of species A, B, C and D respectively.

The Gibbs free energy (ΔG) – which is a function of state – expresses the tendency of a reaction to occur under constant temperature and pressure conditions. When $\Delta G < 0$ the reaction is said to be spontaneous hence it is shifted towards the product formation, when $\Delta G = 0$ the reaction is in equilibrium and when $\Delta G > 0$ the reaction is shifted towards the formation of reactants. The Gibbs free energy can be expressed in terms of the activities of the reactants and products, namely ¹⁰:

$$\Delta G = \Delta G^0 + RT \ln(\prod_i \gamma_i [i]^k) \quad (2.5)$$

where ΔG^0 is the Gibbs free energy under standard operating temperature and pressure conditions, R is the ideal gas constant, T the operating temperature, $[i]$ is the concentration of species i , k its stoichiometric coefficient, considered positive for the products and negative for the reactants, and γ_i its activity coefficient.

For electrochemical devices, and thus for electrochemical reactions, the electrical potential difference E between two electrodes is related to ΔG by the following equation ¹⁰:

$$\Delta G = -n_e F E \quad (2.6)$$

where n_e is the number of electrons transferred in the reaction and F is Faraday's constant.

The Nernst equation combines Eq. (2.5) and Eq. (2.6) in order to obtain the maximum theoretical potential difference in an electrochemical device, specifically ¹⁰:

$$E_N = -\frac{\Delta G^0}{n_e F} + \frac{RT}{n_e F} \ln \left(\frac{[A]^a [B]^b}{[C]^c [D]^d} \right) + \frac{RT}{n_e F} \ln \left(\frac{\gamma_A^a \cdot \gamma_B^b}{\gamma_C^c \cdot \gamma_D^d} \right) \quad (2.7)$$

The high operating temperatures of SOFCs (700-900 °C) and the relatively low operating pressures (1-3 bar) allow to approximate the behaviour of the species as ideal gases; hence the activity coefficients take on a value of one and the species concentrations can be replaced by their partial pressures. Considering the overall reaction for the oxidation of H₂ reported in Equation 2.3 the open circuit voltage takes on the following expression ¹⁰:

$$E_N^{OCV} = -\frac{\Delta G^0}{2F} + \frac{RT}{2F} \ln \left(\frac{p_{H_2,bulk} \cdot p_{O_2,bulk}^{0.5}}{p_{H_2O,bulk}} \right) \quad (2.8)$$

Where $p_{i,bulk}$ denotes the partial pressure of species i in the bulk composition, that is to say the composition under open circuit voltage (OCV).

2.1.2 Electrochemical losses

When the cell is operating and generating current, a number of different polarization losses caused by irreversible mechanisms make the theoretical Nernst potential of the cell drop to a value of voltage V which depends on the operating point. There are three principal losses: the activation losses, the ohmic losses and the concentration losses. The first and the latter are generated at both the anode and the cathode side, while the ohmic losses encompass the ohmic behavior of all the conducting phases. Each irreversibility generates a so called overpotential η_i , which is subtracted from the maximum theoretical Nernst potential: the resulting cell voltage will be then expressed as follows ¹¹:

$$V_{cell} = E_N^{OCV} - (\eta_{act,a} + \eta_{act,c}) - \eta_{ohm} - (\eta_{conc,a} + \eta_{conc,c}) - \eta_{leak} \quad (2.9)$$

Activation polarization

Activation overpotentials in the anode ($\eta_{act,a}$) and cathode ($\eta_{act,c}$) are associated with overcoming the energy barriers at the active sites which prevent reactions taking place spontaneously. The larger the activation energy, the bigger the energy supply needed from the reactants to surpass these barriers.

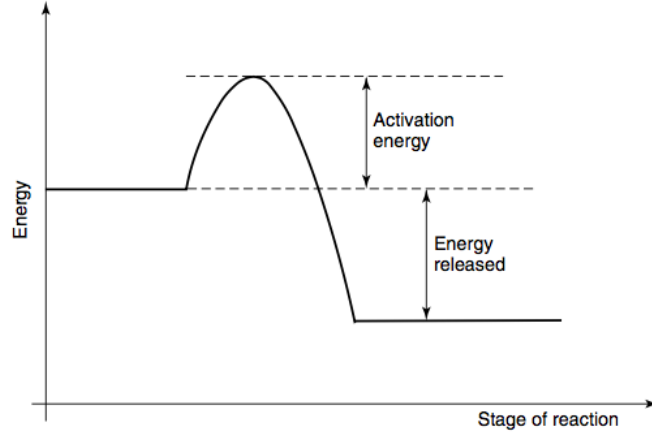


Figure 2.2. Schematic diagram of the stages of reaction as a function of the energy¹¹.

For electrochemical cells, the equation that relates the current density to the overpotential generated at an electrode is the Butler – Volmer equation¹⁰:

$$j = j_0 \left[\exp\left(\frac{\alpha F \eta}{RT}\right) - \exp\left(\frac{(1-\alpha) F \eta}{RT}\right) \right] \quad (2.10)$$

where j is the current density, j_0 is the exchange current density, and α is the charge transfer coefficient at the electrode. The exchange current densities are in turn defined as follows, applying an Arrhenius-type equation for both anode and cathode exchange current densities:

$$j_{0,an} = j_{0,an}^{pre} \left(\frac{p_{H_2}}{p_{H_2,ref}}\right)^{\gamma_{H_2}} \left(\frac{p_{H_2O}}{p_{H_2O,ref}}\right)^{\gamma_{H_2O}} \exp\left(-\frac{E_{act,anode}}{RT}\right) \quad (2.11)$$

$$j_{0,cat} = j_{0,cat}^{pre} \left(\frac{p_{O_2}}{p_{O_2,ref}}\right)^{\gamma_{O_2}} \exp\left(-\frac{E_{act,cathode}}{RT}\right) \quad (2.12)$$

where $j_{0,an}^{pre}$ and $j_{0,cat}^{pre}$ are the exchange transfer current density pre-exponential factors in the anode and cathode respectively, $E_{act,anode}$ and $E_{act,cathode}$ the activation energies for anode and cathode, $p_{i,ref}$ the reference partial pressures which can all be considered to be equal to the ambient pressure, and γ_i is the reaction order of species i .

When the exchange current density $j_0 \geq 4j_0^{pre}$, Equation 2.10 can be simplified and takes on the name of the Tafel equation, which expresses the activation overpotential as a function of the current density:

$$\eta_{act} = \frac{RT}{\alpha nF} \ln \frac{j}{j_0} \quad (2.13)$$

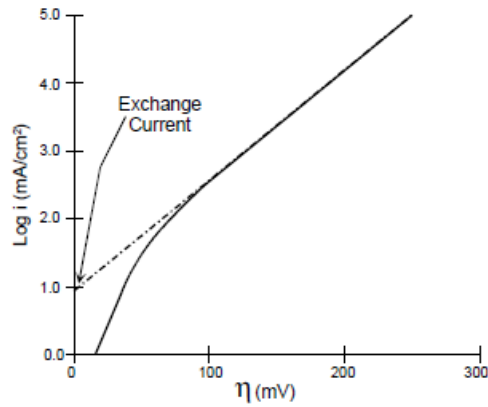


Figure 2.2. Example of a generic Tafel plot ¹⁰.

With this linearization it is possible to estimate the values of α and of j_0 from the slope and the intercept of the curve extrapolated for $\eta = 0$.

Ohmic polarization

The ohmic polarization is caused by the conduction of charge through the ionic and electric conductors within the cell. The electrolyte and the electrode layers in a SOFC obey Ohm's law:

$$\eta_{ohm} = iR_{ohm} \quad (2.14)$$

Where i is the current and R_{ohm} contains the contributions of the ionic conduction, the electronic conduction, and the contact resistance, so that:

$$R_{ohm} = R_{ion} + R_{el} + R_{cont} \quad (2.15)$$

However, in typical SOFCs the resistance associated to the conduction of O^{2-} ions through the electrolyte layer results the major contribution, so that it is generally valid to consider the ohmic contribution to the voltage loss equal to that related to the electrolyte:

$$R_{ohm} \cong R_{ion} \cong R_{electrolyte} \quad (2.16)$$

Concentration polarization

For high utilization factors of the cell, hence for high current densities, the fuel is rapidly consumed in the TPB region; if the request of new H_2 at the TPB is higher than that provided by the diffusion of gas through the porous matrix of the anode, the local undersupply of fuel results in a drop of the cell voltage.

The mass transfer through a porous electrode can be expressed by means of Fick's first law ¹⁰:

$$j = \frac{nFD_i(C_i^{bulk} - C_i^{TPB})}{l} \quad (2.17)$$

where D_i is the diffusion coefficient of the species i , C_i^{bulk} and C_i^{TPB} are the concentrations of the species i in the bulk of the electrode and at the three phase boundary respectively, and l is the thickness of the diffusing layer.

The maximum current, or the limit current, that can theoretically be obtained is when $C_i^{TPB} = 0$, so:

$$j_L = \frac{nFD_i C_i^{bulk}}{l} \quad (2.18)$$

Combining Equations 2.17 and 2.18 it results:

$$\frac{C_i^{TPB}}{C_i^{bulk}} = 1 - \frac{j}{j_L} \quad (2.19)$$

By applying the Nernst equation (Equation 2.7), the concentration overpotential can be expressed as:

$$\eta_{conc} = \frac{RT}{nF} \ln \left(\frac{C_i^{TPB}}{C_i^{bulk}} \right) = \frac{RT}{nF} \ln \left(1 - \frac{j}{j_L} \right) \quad (2.20)$$

Leakage overpotential

Electrolytes are never perfectly fully dense gas barriers, thus leading to fuel crossover from anode to cathode reducing the maximum theoretical voltage. Furthermore, these are never ideal electrical insulators, therefore internal currents appear which further increase the Ohmic losses.

These effects – fuel crossover and internal currents – are essentially equivalent. The crossing over of one hydrogen molecule from anode to cathode where it reacts, wasting two electrons, amounts to exactly the same as two electrons crossing from anode to cathode internally, rather than as an external circuit.

In Equation 2.9, these contributions are contained in the so-called leakage overpotential (η_{leak}); nevertheless these are neglected in many occasions as their effect is insignificant when compared with the rest of overpotentials ¹¹.

2.2. Materials and Designs

Solid oxide fuel cells are, at the state of art, multilayered structures of anode, electrolyte and cathode. Depending on the materials, typology and design of the cell, the operating conditions, their durability and their resistance to fuel contaminants may significantly vary.

Furthermore, when single cells are connected in series to form a stack of the desired power output, other fundamental components are needed: the interconnects layer, or bipolar plates, and, in the case of planar cells, the sealant layers. In the following Sections, a brief description is

provided of the most important types and proprieties of the materials employed for the state-of-art SOFC cells and stack, along with the different typologies of cells.

2.2.1. Electrolyte

The general requirements for an electrolyte in an SOFC are high ionic conductivity, null electronic conductivity, chemical stability in both oxidizing and reducing environments, good mechanical proprieties and long term stability. Moreover, the electrolyte layer must be gas tight in order to avoid cross leakage of the fuel and the oxidant gas.

The most conventional material for SOFC electrolytes is the 8YSZ (8YSZ: 8% Ytria-Stabilized Zirconia), which possesses a good conductivity of $0.5 \text{ S}\cdot\text{cm}^{-1}$, measured at $T = 800^\circ\text{C}$. Other percentages of Y_2O_3 content have been tried, but the best performing composition, both in terms of conductivity values and stability after annealing is the 8%^{12, 13}. Even though its conductivity is not the highest achievable, compared to other candidates for electrolyte materials, it still best matches high conductivity, good thermal expansion coefficient (TEC), good chemical and mechanical stability over a wide range of oxygen partial pressures and temperatures, and at relatively low costs. The nominal operating temperature for cells based on this electrolyte material ranges from 750 to 900°C , depending on the electrolyte layer thickness.

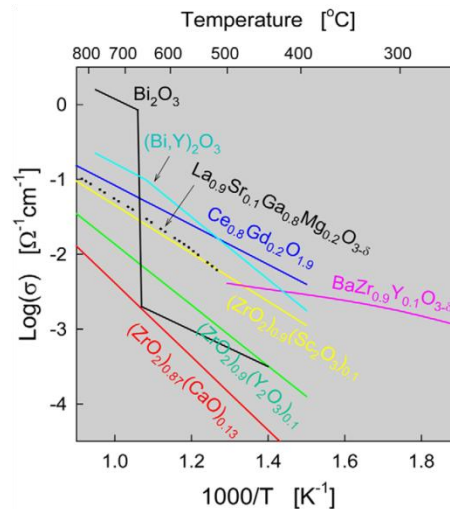


Figure 2.3. Conductivities of selected electrolyte materials

Scandia Stabilized Zirconia (ScSZ) is an alternative to YSZ, especially for use at intermediate temperature, because of its higher conductivity^{14, 15}; until now, however, the lower price and the wider availability of yttria mean that it is much more frequently used as a stabiliser in contrast to scandia.

Another important candidate for the electrolyte material are Gadolinia Doped Ceria (GDC) and Samaria Doped Ceria (SDC) which possess very high ionic conductivity, even at very reduced operating temperature (550 °C). Nevertheless, they also exhibit part of electronic conduction which is attributed to the reduction of Ce^{4+} to Ce^{3+} at low oxygen partial pressures, and also the poor sintering proprieties make them react with other cell materials, especially with YSZ when it is employed as a diffusive barrier at the cathode side^{16, 17}.

2.2.2. Anode

The most commonly applied anode material is a Ni/YSZ cermet¹⁸, which is a mixture of nickel oxide and YSZ powders that, after the sintering of the material and a reduction procedure during the start-up phase of the cell or stack, results in a final structure in which the skeleton of YSZ stabilizes the porosity of the electrode and provides the separation of finely dispersed metallic Ni particles, that act as a catalyst for the oxidation reaction of the hydrogen. In the most diffused typologies of SOFC cells, the planar anode supported cells (AS-SOFCs), the Ni-YSZ is prepared in two different morphologies: the first, thicker one (up to several hundred μm) is the anode substrate, which acts as a support for the whole cell, and possesses a high porosity in order to minimize the mass transport losses. The second structure is a thinner layer (c.a. 10-20 μm), the so called Anode Functional Layer (AFL), which consist of smaller sintered YSZ particles in which the fine Ni catalytic particles are dispersed, in order to extend to the maximum the active surface of the three phase boundary region, at the interface with the electrolyte, in order to minimize the activation polarization losses. This structure results in stable, good performing and low cost anodes.

Nevertheless, even though Ni is a good catalyst for the H_2 oxidation, it suffers from carbon deposition when SOFCs are fed with carbon based, non-conventional fuels; moreover, it is extremely sensitive to the poisoning effects of contaminants such as sulphur and tar compounds (see Section 2.3).

For this reason, other materials have been investigated, especially ceria based ones. CeO_2 anodes can electrochemically oxidize dry methane as the presence of mobile lattice oxygen reduces the rate of carbon deposits. For this particular feature, Ni-Gadolinia Doped Ceria (GDC), Samaria Doped Ceria (SDC) or Yttria Doped Ceria (YDC) have been studied for the application in SOFC anodes; nevertheless, lattice expansion due to $\text{Ce}^{4+} / \text{Ce}^{3+}$ reduction still represents a problem in terms of stability of CeO_2 anode based SOFCs^{19, 20}.

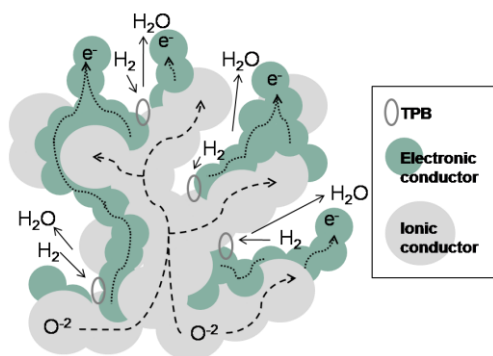


Figure 2.4. Diagram of a state-of-the-art cermet anode illustrating the paths of electrons and O^{2-} ions in the structure.

2.2.3. Cathode

Cathode materials should possess high electrical conductivity and high electrocatalytic activity for the oxygen reduction reaction.

Perovskite materials of ABO_3 type are generally used as cathode material. Among them, Lanthanum Manganite (LaMnO_3) with substitutions of Strontium or Calcium at the A-site have been widely employed²¹.

Mixed Ionic-Electronic Conductors (MIEC) are also drawing much attention as cathode materials. Lanthanum or Strontium Cobaltites, $(\text{La}, \text{Sr})\text{CoO}_3$ show higher cathodic performances than $(\text{La}, \text{Sr})\text{MnO}_3$, even though the matching of the thermal expansion coefficient (TEC) with YSZ is lower²². As a compromise between expansion mismatch and electrochemical performance, the composition $\text{La}_{0.6}\text{Sr}_{0.4}\text{Fe}_{0.8}\text{Co}_{0.2}\text{O}_3$ (LSCF) has been established as a good cathodic material²³. The advantage of such mixed ionic-electronic conducting cathodes is their increased reactive catalytic surface area over the whole perovskite grain.

2.2.4. Interconnects

The interconnect in SOFC stacks is the component which electrically connects the single cells and in planar systems it additionally separates the gas compartments. It requires a number of different proprieties to be achieved, such as good electrical conductivity, gas tightness, chemical compatibility with the adjacent electrodes, high corrosion resistance to the gases, good TEC matching and low costs.

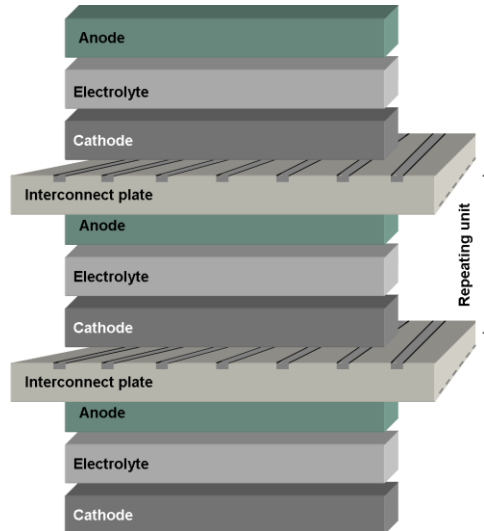


Figure 2.5. Bipolar plates in a planar SOFC stack²⁴.

Principally, interconnects can be divided into two classes of constituent materials: ceramic and metallic materials.

All ceramic interconnects are based on LaCrO_3 . It is stable but possesses a good electrical conductivity only at temperatures above $800\text{ }^\circ\text{C}$. Moreover their cost is significantly high, and since the general trend in SOFC systems is to reduce the operating temperatures, in order to reduce costs and ensure longer operations, this type of materials have lost their appeal in favour of metallic interconnects.

Metallic alloys have replaced ceramic interconnects due to their ease of manufacture, lower material cost and most importantly, higher electronic and thermal conductivities. However, these metallic alloys present a critical issue during long-term operation of the fuel cell stack: volatilization of Cr-containing species (e.g. CrO_3 and $\text{Cr}(\text{OH})_2\text{O}_2$) that end up depositing on the surface of the cathode leading to a rapid deterioration of the O_2 reduction rate^{25, 26}.

2.2.5. Sealants

In planar SOFC stacks, gaskets are required to avoid leakages of gases between the bipolar plates and the electrodes. Seals should be electrically insulating, chemically compatible with different oxide and metallic cell components and stable under thermal cycling between room temperature and operating temperature.

There are two classes of seals: rigid and compressive.

Glass or glass ceramics²⁷ have demonstrated to be chemically stable in both oxidizing and reducing environments. However, due to the addition of barium or calcium silicates to fulfil the requirements of thermal expansion coefficient, diffusion and segregation of species may occur during long term operation at the interface with the cell²⁸.

Besides glass-ceramics, compressive seals have also been investigated. They are generally metallic gaskets or mica-based materials²⁹. To achieve low leakage rates they generally require high mechanical loads, but possess however a good matching of TEC and chemical stability.

2.2.6 Tubular SOFCs

Tubular SOFCs are cylindrically shaped with a length comprised between 1.5 – 2 m for most of their applications. This geometry comprises three cylindrical and concentric layers of anode-electrolyte and cathode materials, that generate a rigid tube with only one opened extremity. Depending on the external layer, the fuel (or air) is fed by a coaxial tube, while the air (or fuel) flows over the external part of the cell.

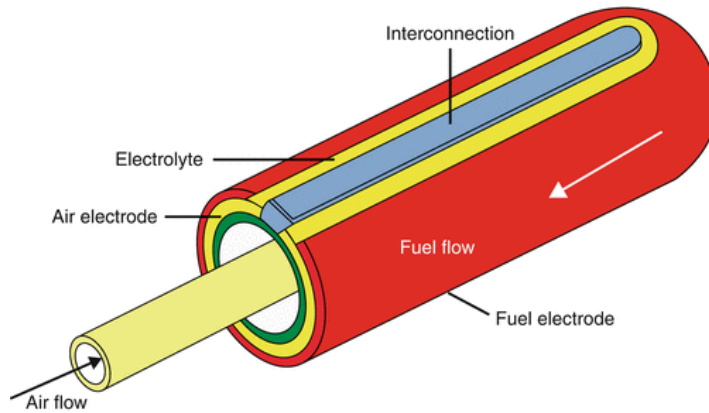


Figure 2.6. Tubular geometry of a SOFC³⁰

The main advantage of tubular SOFCs, compared to their planar analogous, is that they do not require sealants. They also allow faster start-up and shut-down procedures, and possess a better structural robustness for long-term operation. Nevertheless, their power density is considerably lower, due to the high internal resistance caused by the long path that the current must cover to reach the external circuit; moreover, the production costs are higher due to complex deposition techniques required to obtain cylindrical oxide layers.

2.2.7. Planar SOFCs

Planar SOFCs are generally square-shaped with dimensions that range between $10 \times 10 \text{ cm}^2$ and $20 \times 20 \text{ cm}^2$, in order to avoid fractures during manufacturing due to the high temperature and pressure gradients, and with a mean thickness of around one mm (or even less).

Depending on the supporting layer, upon which the other layers are deposited, there are four typologies of planar SOFCs: Electrolyte Supported (ES-SOFCs), Anode Supported (AS-SOFCs), Cathode Supported (CS-SOFCs) cells and Metal Supported (MS-SOFCs)^{9, 10, 11}.

Concerning the first three types of cells, the anode supported type is the most widespread, allowing to reduce the thickness of the electrolyte layer below $10 \text{ }\mu\text{m}$, and thus dramatically reducing the overall internal resistance of the cell; moreover the anode support results more mechanically stable and has better manufacturing proprieties than the cathode materials.

Recently, to overcome the issues of anode supported SOFCs related to the low reliability of sealant materials, and to failures of the cells related to thermal transients and mechanical stresses, metal supported SOFCs have been developed ³¹.

The principal difference with respect to AS-SOFCs is that the anode support is substituted by a porous metallic support, and the anode is deposited as a thin film over its surface. The overall structure has generally the same thickness.

Metal supported cells offer several advantages like lower production costs, better tolerance to contaminants and general improved robustness to mechanical stresses. Nevertheless, they still require more investigations to finally enter the market of SOFC.

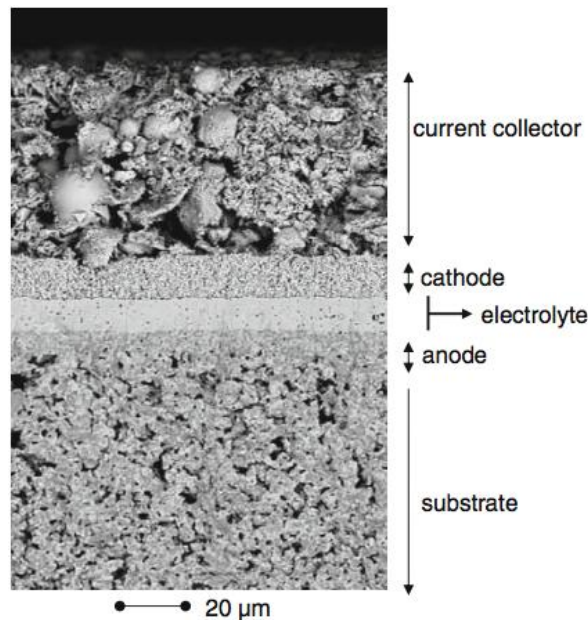


Figure 2.7. SEM images of the cross section of a typical anode supported SOFC. At the anode side, the anode support and the anode functional layers can be distinguished.

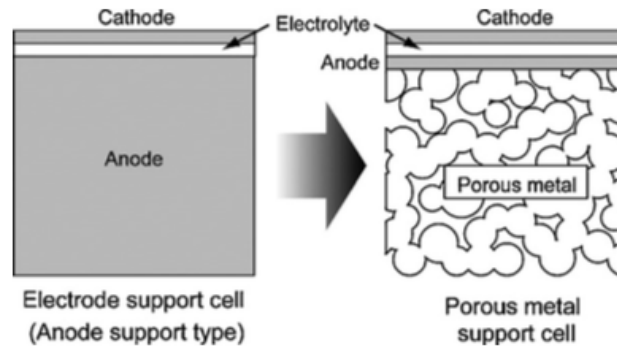


Figure 2.8. Schematic representation of the comparison between the anode supported and metallic supported SOFCs structures.

2.3. Fuel flexibility

Hydrogen is the preferred fuel for SOFCs systems, as it guarantees high power and thermal output, safe operation for cell components and water as the only exhaust gas; it is also planned in the future to be generated from renewable sources, thereby becoming an attractive energy vector for the spread of green technologies. Nevertheless, to the present day, hydrogen is produced almost totally from hydrocarbons, and there is a very low penetration of H₂ distribution infrastructures or storage facilities; this clearly hinders to some extent the possibility of hydrogen-fed SOFCs to become competitive systems for heat and power generation on the market.

However, as explained also in the previous Sections, fuel flexibility is one of the most attractive proprieties of SOFCs, thereby being able to produce electricity and heat starting from more conventional carbon-based fuels, due to their high operating temperatures, high catalytic activity and low susceptibility compared to low-temperature fuel cells.

A number of different fuels can be successfully employed with SOFCs: natural gas, syngas produced from gasification of coal and biomasses, biogas coming from anaerobic digestion of organic wastes, and even liquid fuels such as diesel and alcohols^{32, 33, 34, 35, 36}.

Since the aim of this work is to shed light on the different processes occurring when IT-SOFCs are fed with syngas mixtures, in the following Sections a brief discussion about the feeding of SOFC with syngas is reported, highlighting those aspects that will be instrumental for the discussion of the experimental results obtained within this work.

2.3.1 Non-conventional fuel: syngas

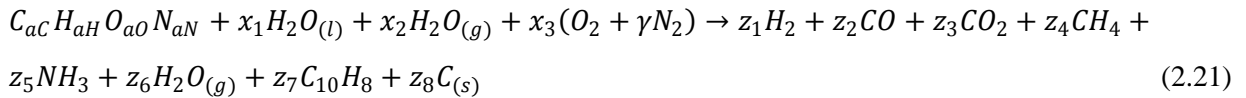
With the term syngas a gas mixture is generally intended in which the principal components are H₂ and CO. There are several ways to produce a syngas; however the most interesting sources of syngas for the application in SOFC systems are the gasification of biomass and the conversion of natural gas by means of the reforming reaction.

From these two sources, the produced syngas is generally a mixture of H₂, H₂O, CO, CO₂, CH₄ and N₂. A typical syngas composition resulting from a biomass gasifier is reported in Table 2.1. below ³⁷:

Syngas					
H ₂ (%)	H ₂ O (%)	CO (%)	CO ₂ (%)	CH ₄ (%)	N ₂ (%)
10-50	0-30	10-45	10-30	1-20	0-50

Table 2.1. Mean composition of a syngas

The gasification process is a thermochemical process that uses air, oxygen or steam as gasification agents that convert the biomass (or coal) in a gas rich in hydrogen and carbon monoxide. A generic reaction for the gasification of biomass can be expressed as follows:



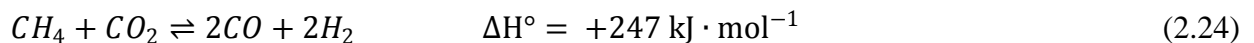
The temperature employed for the gasification process is typically above 800 °C.

Besides the reported products, other impurities, which are contaminants for SOFCs, are generally present, such as H₂S, HCl, NH₃ and Tars. In Section 2.3.3, particular attention will be provided to the description of tars and their effects on SOFCs, since part of the experimental analysis was aimed to investigate the effect of this class of compounds on IT-SOFC cells.

Natural gas can be converted into a syngas by means of the steam reforming reaction. In the case of SOFC systems, this fuel conversion can proceed directly at the SOFC anode, thanks to the catalytic properties of dispersed Ni particles, or in an upstream reformer. The former process is

called Direct Internal Reforming (DIR) while the latter is known as Indirect Internal Reforming (IIR). Depending on the applications, either the DIR or the IIR conversion can be applied; nevertheless, IIR is generally preferred due to the significant thermal and concentration gradients that arise when methane is reformed directly at the anode, which can compromise the longevity of the entire system.

For methane, the main reactions occurring in this conversion to syngas are the steam reforming reaction (Equation 2.22), and the subsequent water gas shift (2.23) and dry steam reforming (2.24), that may occur once the steam reforming products start to appear in the gas mixture.



The endothermic steam reforming reaction is thermodynamically favoured at high temperatures and low pressures and, along with the water gas shift reaction, they are generally carried out at temperatures above 700 °C and with Nickel based catalysts.

2.3.2 Operation of SOFC with syngas

When an SOFC cell is fed with a syngas, a number of different reactions, both of chemical and electrochemical nature, occur.

Figure 2.9. below summarizes all the possible reactions than can develop in a SOFC fed with syngas.

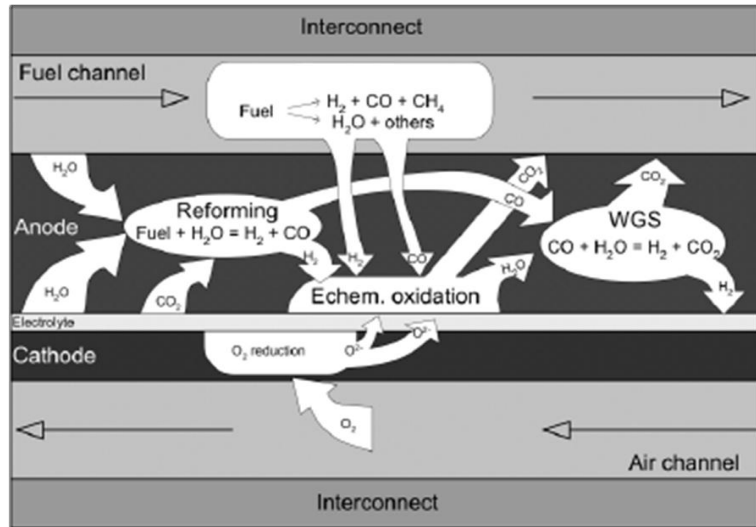


Figure 2.9. Schematic representation of the possible reactions within an SOFC fed with syngas

Along with the electrochemical oxidation of H_2 (Equation 2.1) and the aforementioned steam reforming and water gas shift reactions (Equations 2.22 and 2.23) other mechanisms are theoretically possible, depending on the conditions of temperature, gas compositions, cell materials, and operating point at which the SOFC works.

Carbon monoxide and methane can be electrochemically oxidized (Equations 2.24 and 2.25 respectively) and equilibria like the methane cracking (Equation 2.26) and the Boudouard reaction may be present, forming carbon deposits:



The operation of SOFCs with syngas has been widely studied in literature, but a clear comprehension of the occurrence of all these reactions and their pathway is still missing, especially due to the lack of analysis tools able to provide information directly *in-operando*. As

previously mentioned, the study of these reactions by means of innovative tools of analysis will be the objective of this work.

2.3.3 Fuel impurities: tar

Especially in the case of syngas produced by gasification of biomasses, impurities that may be harmful for the safe operation of SOFC systems are always present and may cause a fast degradation of performances, leading to cell failure.

Moreover, since the general trend in SOFC systems is to reduce the operating temperatures, employing the next generation of IT-SOFCs, lowering the operating temperature leads to a general reduction of the tolerance limits of SOFCs to typical biomass gasification product gas contaminants³⁸.

These contaminants are mainly sulfurous compounds (such as H₂S), NH₃, HCl, alkali, and tars³⁹. As regards the effects of the former impurities (H₂S, NH₃, HCl and alkali compounds) on solid oxide fuel cells, they have been studied and results are reported in literature, together with tolerance limits^{40, 41, 42, 43}, while there is a lack of literature concerning the tolerance limits and the effects of a long term exposure to the latter (tar).

Tar can be defined as an organic compound with a molecular weight larger than benzene. This class of compounds comprises a number of organic condensable hydrocarbons, formed by aromatics and polycyclic aromatic hydrocarbons (PAH). Tars are classified as primary, secondary and tertiary tars; however, Bergman et al.⁴⁴ formulated an alternative classification based on the structure and on the molecular weight of the species; this classification is summarized in Table 2.2.

Class	Type	Examples
1	Gas Chromatography (GC) undetectable tars	Biomass fragments, heaviest tars
2	Heterocyclic compounds	Phenol, cresol, pyridine
3	Light aromatics (1 ring)	Toluene, xylene
4	Light polyaromatics (2-3 ring)	Naphthalene, anthracene, phenanthrene
5	Heavy polyaromatics (>3 rings)	Pyrene, fluoranthene

Table 2.2. Classification of tars.

The amount of tars produced during the gasification of biomass can be as high as several hundred of $\text{g}\cdot\text{Nm}^{-3}$, depending on the gasification technology applied ⁴⁵. Also the composition of the tar mixture in the gas stream largely depends on the nature of the feedstock, on the different gasification technologies, and on the operating conditions of the gasifier. However, it frequently comprises a 50% of benzene and toluene, with the other half covered by the rest of the tar typologies.

Tar species induce a pronounced carbon deposition through a complex series of different chemical reactions, comprising also the steam reforming (or even the dry reforming in presence of CO_2) and the thermal degradation of this class of hydrocarbon. The product species of these reactions can further interact with each other, leading to other possible carbon deposition reactions ⁴⁶.

As a result of carbon formation, deactivation of Ni catalyst, reduction of the Three Phase Boundary length (TPB) and hindering of the transport of reactants to the active sites due to pore occlusion, are the main effects that affect negatively the cell performances ^{47, 48, 49, 50}.

However, the possibility of carbon formation and the rate of deposition are strictly dependent on the operating conditions, such as operating temperature, moisture content and current density, on the anode material and on the type and concentration of tar species.

A study of the effects of a model tar in a simulated syngas fed to an IT-SOFC will be presented in Chapter 5.

3. ANALYSIS TOOLS AND TECHNIQUES

In this Chapter, a description of the basics of the principal and most renowned electrochemical characterization techniques employed in the study of SOFC cells, namely Polarization Curves (or i-V curves) and Electrochemical Impedance Spectroscopy (EIS), is provided.

The main focus of the following Sections will be the description of the fundamental principles of two advanced analysis techniques that both rely on the EIS measurements: the Distribution of Relaxation Times (DRT) method and the Complex Non-linear Least Squares (CNLS) fitting. The combination of these three analysis tools (EIS-DRT-CNLS) will be the basis of the main results obtained in the experimental work of this thesis.

Finally, a brief description will be provided at the end of this Chapter of the principal post-mortem characterizations employed to further confirm the results obtained from the *in-operando* analysis presented in this work.

3.1. Polarization curves

The polarization curve (or i-V curve) is the most employed diagnostic technique used to characterize the overall immediate performance of SOFC cells^{10, 11} (see Figure 3.1).

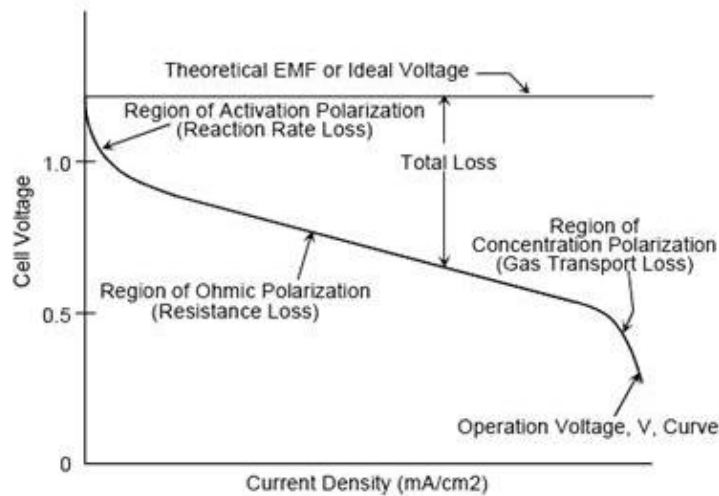


Figure 3.1. Polarization curves and regions at which the different polarization losses are predominant⁵¹.

It consists in the measurement of the cell voltage with the varying of the current generated and extracted from an external load. It provides information about the general electrical response of the cell over the range of currents investigated, and hence it is a valuable instrument to assess the dependency of the cell performances to the operating conditions, but it can also suggest hints about the effect of the different polarization losses by examining the different portions of the plot. First of all, the Open Circuit Voltage (OCV), measured at $i = 0 \text{ A}\cdot\text{cm}^{-2}$, can be compared to the theoretical voltage calculated from the Nernst equation and the difference between them is a good estimation of losses related to gas leakages, since the Nernst voltage is the maximum voltage obtainable in ideal conditions.

The rapid drop of the cell voltage at low current densities is the reflection of the polarization losses related to the overcoming of the activation energies for the electrochemical reactions at the electrodes. Hence it weights the impact of the activation overpotential η_{act} of both the anode and cathode reactions.

The linear trend that covers most of the plot is caused by the ohmic polarization due to the internal resistance of the cell, which is constant with respect to a change in the current density (Equation 2.14). As explained in Chapter 2, for SOFCs the main contribution to the ohmic resistance of the whole cell is ascribable to the resistivity of the electrolyte layer. From the slope of this central region of the i-V curve the physical quantity known as Area Specific Resistance (ASR), measured in $\Omega\cdot\text{cm}^2$, is generally estimated in order to compare the overall performances of different cells.

Finally, when high current densities are required from the cell, an undersupply of reactants in the active regions of the cell occurs, which is caused by the mass transport limitations of gases through the electrolyte layers or by simple fuel starvation. The fast drop of the cell voltage is related to the concentration overpotential η_{conc} , and it represents the maximum current that can be supplied from the cell without incurring into severe material degradation.

3.2 Electrochemical Impedance Spectroscopy (EIS)

3.2.1. Principles of EIS

Electrochemical Impedance Spectroscopy (EIS) is a very sensitive technique that maps an electrochemical cell's response to the application of a periodic small AC signal carried out at

different frequencies. In contrast to polarization curves, EIS measurements can shed light on the diverse physicochemical processes occurring in the active layers of the cell, as each process has associated a unique time-constant (relaxation time) and therefore each one of is exhibited at different frequencies ⁵².

If the studied system satisfies contemporaneously the conditions of causality, linearity and time-invariance, the response to a sinusoidal voltage (or current) excitation signal is a sinusoidal current (or voltage) signal, sharing the same frequency ⁵³. For a generic sinusoidal voltage input signal $e(t) = E \cos(\omega t + \theta)$ the response is a current signal which can be expressed as: $i(t) = I \cos(\omega t + \varphi)$, where $\omega = 2\pi f$, f being the signal's frequency, E and I are the amplitude of the voltage and current signals respectively, whilst θ and φ are their initial phases. Both sinusoidal expressions can be rewritten as complex-form functions, namely ⁵⁴:

$$e^*(t) = E \cdot \exp[j(\omega t + \theta)], \text{ with } e(t) = \text{Re}[e^*(t)] \quad (3.1)$$

$$i^*(t) = I \cdot \exp[j(\omega t + \varphi)], \text{ with } i(t) = \text{Re}[i^*(t)] \quad (3.2)$$

The impedance value measured at different frequencies is given by:

$$Z^*(\omega) = \frac{e^*(t)}{i^*(t)} = \frac{E}{I} \exp[j(\theta - \varphi)] = \frac{E}{I} (\cos(\theta - \varphi) + j \sin(\theta - \varphi)) \quad (3.3)$$

which can be expressed as a complex number having its real and imaginary components expressed as follows:

$$\text{Re}[Z^*(\omega)] = Z'(\omega) = \frac{E}{I} \cos(\theta - \varphi) \quad (3.4)$$

$$\text{Im}[Z^*(\omega)] = Z''(\omega) = \frac{E}{I} \sin(\theta - \varphi) \quad (3.5)$$

3.2.2. EIS measurements on SOFC

As illustrated in Chapter 2, during the operation of an SOFC, a number of physicochemical processes occur contemporaneously. Each of them have a characteristic frequency at which they can be excited by the sinusoidal stimulus provided by a Frequency Response Analyzer (FRA) and the electrical response, measured in terms of amplitude and phase shift of the signal, is the response of that single process having its maximum intensity at that particular frequency.

If the excitation signal has a small amplitude, which in SOFC cells generally corresponds to c.a. 10 mV (or a current stimulus corresponding to an oscillation of the cell's voltage of 10 mV), the response of the cell can be considered linear and time invariant ⁵⁵.

Impedance measurements can be reported in two different plots: the so-called Nyquist plot, which reports the real part of the measured impedance against its imaginary part, and the Bode plots, that depict the dependency on the imposed frequency of the impedance modulus or the phase shift.

The impedance response of a SOFC cell is generally reported in a Nyquist plot, as it provides quantitative information, expressed in terms of resistances, about the polarization losses that affect the i-V characteristics.

Figure 3.2. reports an experimental EIS spectrum, in the form of the Nyquist plot, measured from a sample tested in this work.

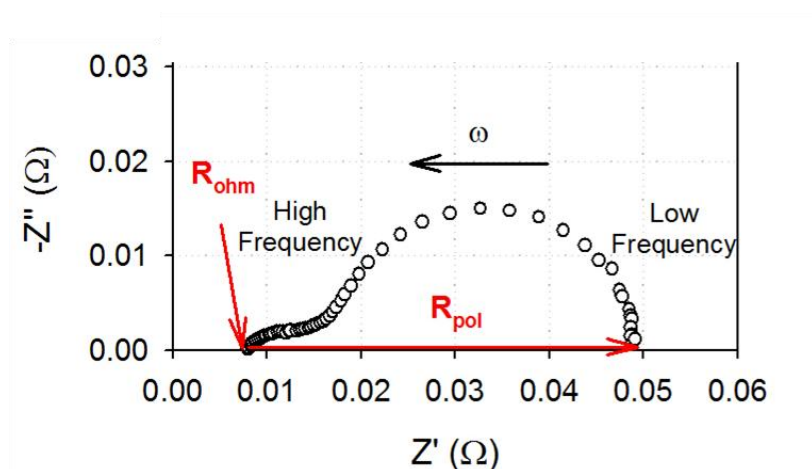


Figure 3.2. Electrochemical impedance spectrum of a single cell sample ($10 \times 10 \text{ cm}^2$) measured at $T = 700 \text{ }^\circ\text{C}$ in humidified hydrogen.

From the intercept of the experimental data with the real axis ($-Z'' = 0 \Omega$), the value of impedance corresponds to the total ohmic resistance of the cell, which generates in the i-V curve the linear trend in the central part of the plot.

The difference between the resistance measured from the last point on the real axis to the first one is the measure of the so-called polarization resistance R_{pol} , that is given by the sum of all the activation and mass transport losses of both the anode and cathode sides, as previously explained in Chapter 2.

Further information can be given accepting the general assumption, which is considered valid for SOFC cells, that the small arc appearing in the high frequency region is related to the fast charge transfer mechanism involved in the electrochemical reactions at the anode and at the cathode; for this reason, if the real part of the total impedance of this arc is extrapolated, it results as the resistance related to the charge transfer mechanisms that cause the activation overpotential losses. By similar considerations, the bigger arc appearing in the low frequency region is often associated to the mass transport losses related to the diffusion of the gasses in the porous matrix of the electrodes; it is thus a measure of the diffusion resistance which causes the voltage to rapidly drop at high current densities^{56, 57}.

Even though the information obtainable from the analysis of Nyquist plots provides quantitative measurement about the polarization losses, nothing can be said about which process, anodic or cathodic, is predominant on a given amount of polarization loss; moreover, since the EIS response appears very broadened, it is difficult to clearly visualize the contributions of single physicochemical processes to the total polarization resistance, hence impeding a profound and complete comprehension of the evolution of these processes and their dependency to the operating conditions of the cell.

In the following Section, a novel and reliable deconvolution methodology (DRT) for the EIS spectra will be extensively explained.

3.3. Distribution of Relaxation Times (DRT) method: deconvolution of signals

SOFCs are complex electrochemical devices, in which many processes occur at the same time, each process being characterized by its typical relaxation time. When two (or more) processes have a similar relaxation time, it is hard to separate and distinguish their contributions to the

overall impedance of the cell, since the EIS spectra can clearly distinguish processes separated at least by two decades in the frequency domain. Furthermore, it is hard to identify small contributions, these being totally covered by processes with large polarization losses.

The Distributed Relaxation Times (DRT) method, is a mathematical tool which allows to overcome this issue, by calculating the distribution of relaxation times function of the processes from the experimental data ⁵⁸.

It is based on the validity of the Kramers-Kronig equations ^{59, 60} for the cell studied:

$$Z'(\omega) = R_0 + R_{pol} \sum_m \frac{1}{1 + (\omega\tau_m)^2} a_m \quad (3.6)$$

$$Z''(\omega) = R_{pol} \sum_m \frac{-\omega\tau_m}{1 + (\omega\tau_m)^2} a_m \quad (3.7)$$

where R_0 is the ohmic resistance of the cell, R_{pol} is the polarization resistance, ω is the angular frequency, τ_m the relaxation time of the process m and a_m is the contribution of the process m to the total polarization loss.

The DRT function can be calculated either from Eq. 3.6 or Eq. 3.7. Considering the Eq. 3.7 expressed in its matrix form, and introducing the constant value of the polarization resistance into the distribution vector $b_m = R_{pol} a_m$, it results:

$$\mathbf{Z}'' = \mathbf{K}\mathbf{b} \quad (3.8)$$

To solve the Eq. 3.8, the Tikhonov regularization algorithm has been employed ^{61, 62}. This algorithm allows to obtain the distribution vector \mathbf{b} as:

$$\mathbf{b} = (\mathbf{K}^{-1} \mathbf{K} + \lambda \mathbf{I})^{-1} \mathbf{K}^T \mathbf{Z}'' \quad (3.9)$$

where \mathbf{I} is the identity matrix, and λ is the self-consistent regularization parameter that must be optimized: too small values result in artificial meaningless peaks, while too large values excessively smooth out the shape of the distribution function.

In Fig. 3.3, the imaginary part of the impedance of a dummy-cell is compared to the distribution function obtained from the DRT calculation over the experimental spectrum, as a function of the

frequency. In Fig. 3.4. the imaginary part of the EIS spectrum of an IT-SOFC button cell (active surface 2 cm^2 , employed in this work) is compared to its distribution function derived from the DRT calculation carried over the imaginary part of its impedance. The dummy-cell consisted of a resistance R_1 in series with a resistance R_2 and a capacitor C_1 connected in parallel, with $R_1 = 10 \text{ } \Omega$, $R_2 = 100 \text{ } \Omega$, and $C_1 = 100 \text{ } \mu\text{F}$. The spectrum shown in Fig. 1b was obtained from a button cell sample at $T = 675^\circ\text{C}$ in a fuel mixture of $\text{H}_2 = 20 \%$, $\text{N}_2 = 76 \%$ and $\text{H}_2\text{O} = 4 \%$, in OCV condition.

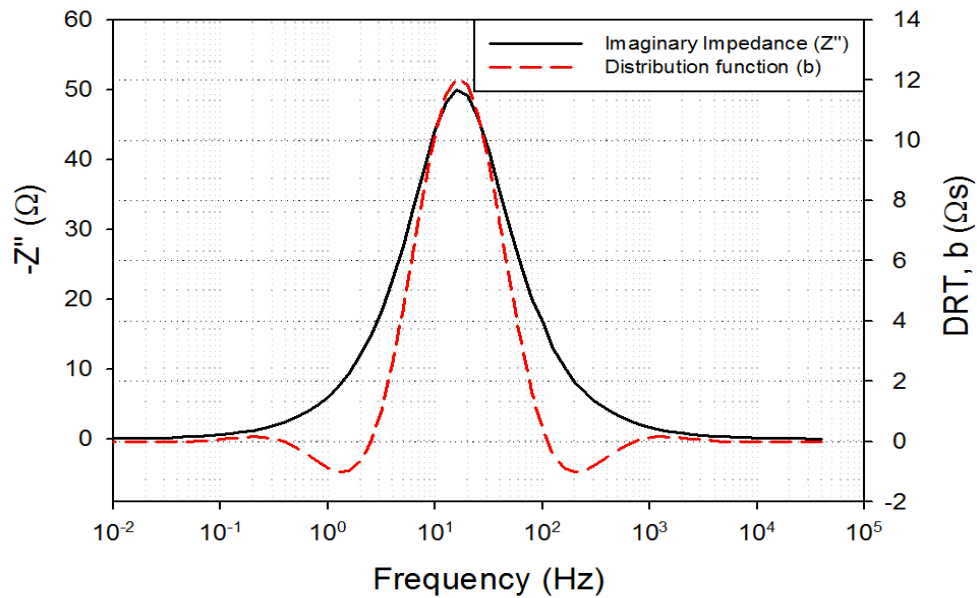


Figure 3.3. DRT distribution function with the imaginary part of the impedance of a dummy-cell.

Observing Figure 3.3, it shows that the DRT calculation does not affect the characteristic frequency at which the process occurs. Depending on the value of λ , fluctuations in proximity of the peak may appear; however, the optimal value of λ , which minimize the fluctuations related to the calculation process, can be estimated from the L-curve of the Tikhonov regularization method⁶³. The optimal value of λ is in proximity of the angle formed from the L-shaped curve (Figure 3.5).

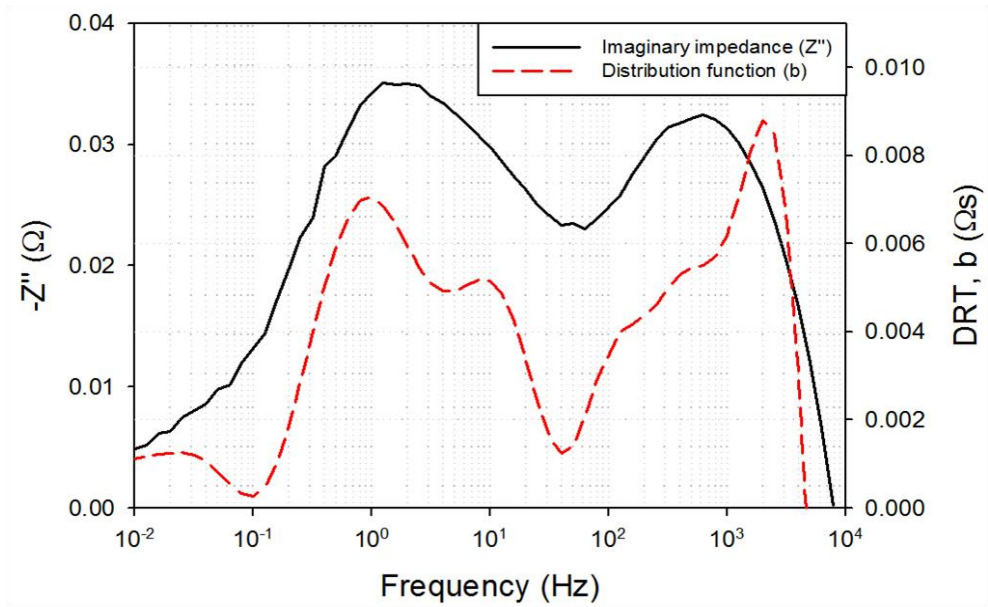


Figure 3.4. DRT distribution function the imaginary part of the impedance of an IT-SOFC button cell operating at $T = 675^{\circ}\text{C}$ in humidified H_2 - N_2 mixture.

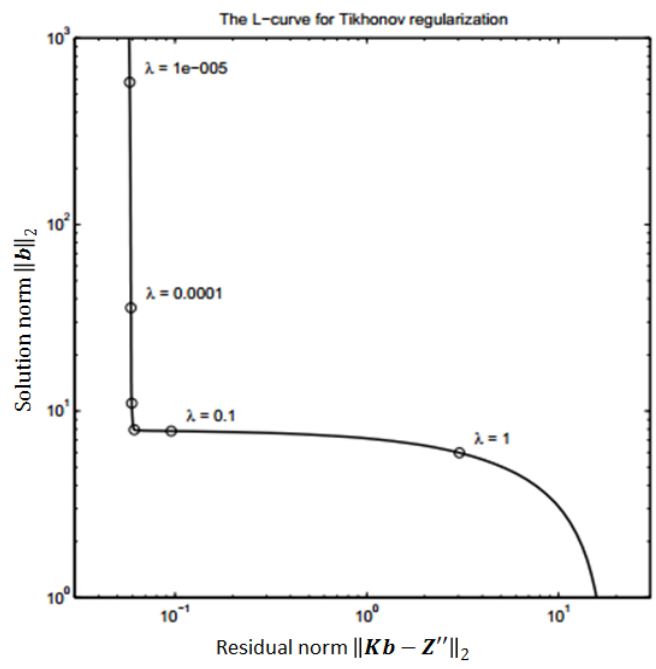


Figure 3.5. L-curve for Tikhonov Regularization.

As shown in Fig. 3.4, from the DRT calculation, 6 different peaks can now be distinguished from the imaginary part of the EIS measurement. The nature of these peaks will be assessed by means of a systematic experimental campaign, presented hereafter, to understand whether a single peak corresponds to an anodic process or a cathodic process, and to further comprehend the nature of the process behind each peak (charge transfer or mass transport phenomena).

The DRT method has been already successfully employed in the study of physicochemical processes occurring in anode-supported SOFCs operating in humidified hydrogen^{64, 65} or in reformat fuel⁶⁶, in tubular SOFCs⁶⁷, and in the study of degradation effects^{68, 69}, providing profound insights about the number, nature and behavior of the diverse processes that determine the overall response of a SOFC, under a broad range of different operating conditions.

It is important to underline that the quality of the experimental data plays a fundamental role in the interpretation of the DRT plots. If the experimental spectra are affected by instrumental interference that cause a loss in the linearity of the EIS response, scattered signals appears in the EIS spectra that will be converted into ghost peaks into the DRT plots, impeding a correct identification and analysis of the processes.

A method to assess the quality of the experimental spectra is the so-called Kramers-Kronig test, which basically assess the validity of the Kramers-Kronig relationships through all the frequency range examined. In this work, the Kramers-Kronig test was performed by means of the Kramers-Kronig test for Windows^{9, 10}, software developed by B.A. Boukamp *et al.*

The residual errors plot of the aforementioned test is depicted in Fig. 3.6. Since the distribution of the points (red dots for the real part and blue dots for the imaginary part of the impedance) is random for all the frequency range, and the maximum error lies below 0.5%, the experimental data can be considered reliable.

It must be noted that in some cases, especially when high water contents are fed to the cell, the low frequency region of the spectra is affected by a more significant error, but still acceptable.

As it will be explained in the discussion of experimental results, attempts to measure the impedance response of the cell under a constant current density were performed; however the quality of the spectra in these cases, evaluated by this KK-test, resulted poor and were judged unusable for the objectives of this work. On the contrary, all the measurements carried out in OCV conditions resulted acceptable.

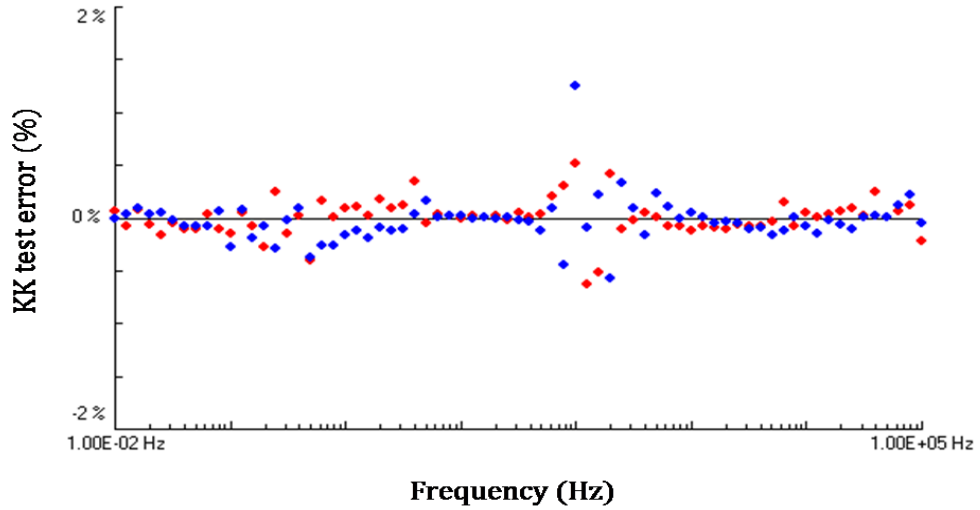


Figure 3.6. Kramers-Kronig test results for the EIS measurement performed on a button cell sample (active area 2 cm^2) at 700°C in humidified hydrogen. Red dots are related to the real part of the impedance, while blue dots are related to the imaginary part.

3.4. Complex Non-linear Least Squares (CNLS) fit

As previously explained, EIS is a powerful tool to measure the sources of potential losses within an SOFC under operating conditions. Nevertheless, a profound interpretation of the single physicochemical processes results in a very complex problem, since it often requires *a-priori* assumptions about the system being investigated ⁷⁰.

One of the most widespread ways to extract quantitative information about the different contributions to the EIS spectra is a fitting procedure of the experimental data with a so-called Equivalent Circuit Model (ECM), which is a sequence of circuit elements, such as resistances and capacitors, connected in series and/or in parallel, which aims to simulate the experimental electrical response of the investigated device ³.

The unknown values of the parameters defining the equivalent circuit elements are generally evaluated by a Complex Non-linear Least Squares (CNLS) fitting algorithm.

This fitting procedure aims to find a set of parameters that minimize the following sum:

$$Q(\vec{p}) = \sum_{k=0}^{N-1} \left[w_{k,r} (\Phi'(\omega_k, \vec{p}) - Z'(\omega_k))^2 + w_{k,l} (\Phi''(\omega_k, \vec{p}) - Z''(\omega_k))^2 \right] \rightarrow \text{Min} \quad (3.10)$$

with:

$$\vec{\Phi}(\omega_k, \vec{p}) = \Phi'(\omega_k, \vec{p}) + j\Phi''(\omega_k, \vec{p}) \quad (3.11)$$

and:

$$\vec{Z}(\omega_k) = Z'(\omega_k) + jZ''(\omega_k) \quad (3.12)$$

where $\vec{\Phi}(\omega_k, \vec{p})$ is the model fit function and $\vec{p}(R_0, R_1, R_2, \dots, C_1, C_2, \dots, R_N, C_N)$ is the fit parameter vector. $Z'(\omega_k)$ and $Z''(\omega_k)$ represent the real and imaginary part of the measured impedance, respectively, and $\vec{Z}(\omega_k)$ is the measured curve. $w_{k,r}$ and $w_{k,l}$ are the weight factors of the k^{th} experimental point.

3.4.1. Equivalent circuit elements

A brief summary of the typical circuit elements employed for the build-up of an ECM which simulates the EIS response of an SOFC will be provided in this Section. In this work, the ECM based CNLS fitting procedure was carried out by means of the Zview software⁷¹.

It is generally assumed that the processes occurring at the interface of an SOFC can be modeled with a simple parallel of a resistance and a capacitor (RC parallel)⁷².

The impedance of a resistance is not a function of the frequency, so:

$$Z_R = R \quad (3.13)$$

and its response in a Nyquist plot will be a point on the real axis having a resistance value equal to its modulus. In the Bode plot, its modulus will be constant with respect to the frequency, so it will appear as a *plateau*.

The impedance of a capacitor is only composed of an imaginary part:

$$Z_C(\omega) = -\frac{1}{j\omega C} \quad (3.14)$$

where C is the modulus of the capacitance. In a Nyquist plot, the response of a capacitance is a set of points displaced on a vertical line, parallel to the imaginary axis. In a Bode plot, with a log-log plot, it will result as a linear trend.

Thus said, an RC parallel element will have an impedance value that can be written as:

$$Z_{R||C}(\omega) = -\frac{R}{1+j\omega RC} \quad (3.15)$$

The product RC represent the characteristic time constant of the circuit. Thus, the characteristic frequency of the process that is modeled by an RC parallel assumes the value of:

$$\omega_{RC} = 2\pi\nu_{RC} = \frac{1}{\tau_{RC}} = \frac{1}{RC} \quad (3.16)$$

where ν_{RC} , ω_{RC} and τ_{RC} are the characteristic frequency, angular velocity, and characteristic time of the RC parallel. Nevertheless, when the process takes place in non-ideal conditions, for example with a distributed surface reactivity, with surface inhomogeneity, roughness or fractal geometry, a constant phase element (CPE) is generally preferred over the capacitor for fitting purposes as it can represent the deviation from a pure capacitance of the EIS response by means of an exponential factor, n , with $0 \leq n \leq 1$ ⁷³.

The impedance of a CPE element is defined as follows:

$$Z_{CPE} = \frac{1}{(j\omega)^n Y_{CPE}} \quad (3.17)$$

Where Y_{CPE} is the admittance of the CPE element. If $n = 1$, the expression of the impedance of the capacitance with $Y_{CPE} = C$ is obtained.

If an RC parallel element is replaced by an R-CPE parallel, the impedance of this element assumes the expression:

$$Z_{R||CPE}(\omega) = \frac{R}{1+R(CPE)^{-1}} \quad (3.18)$$

The characteristic time constant and the following characteristic frequency of the process assume the form of:

$$\tau_{R||CPE}(\omega) = \sqrt[n]{(RY_{CPE})} \quad (3.19)$$

$$v_{R||CPE} = \frac{1}{2\pi\tau_{R||CPE}} = \frac{1}{2\pi\sqrt[n]{(RY_{CPE})}} \quad (3.20)$$

An example of the Nyquist plots for an R-CPE element with various n values is given in Figure 3.7. below. When n = 1, the Nyquist plot of a simple RC element is obtained.

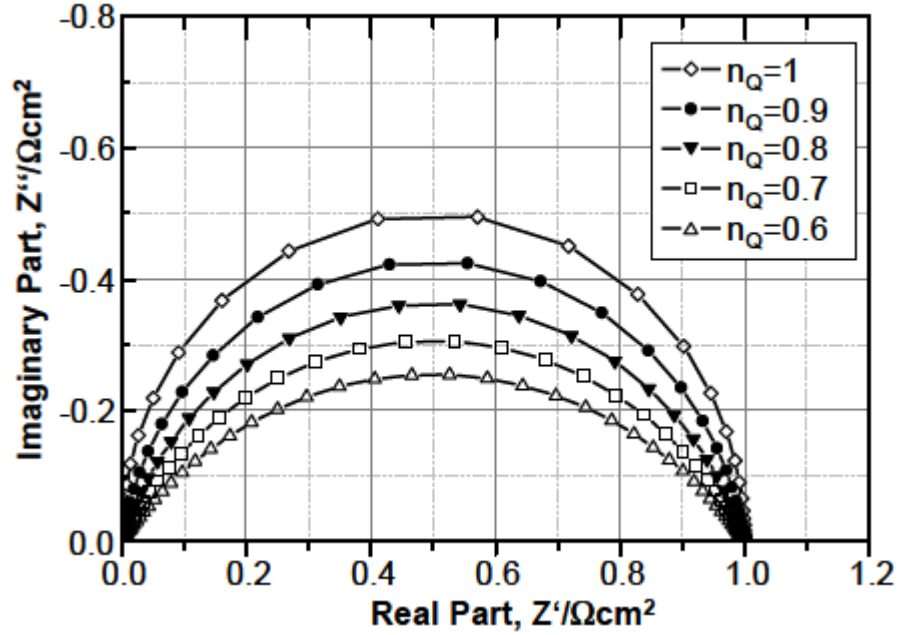


Figure 3.7. Nyquist plots of an R-CPE element for different values of n⁷⁴.

The RC parallel element is also assumed to be valid as the most simple way to model the impedance response of mass transport processes. Nevertheless, for the diffusion of gases in a solid porous matrix, a particular element, the so-called Finite-length Warburg Element (FLW) has been developed, and it is frequently applied in the SOFC field to model the diffusion of the anode and cathode gases through the electrode porosity⁷⁵.

The expression of the impedance of a Warburg element is given by:

$$Z_{FLW}(\omega) = R_W \frac{\tan h[(j\omega T_W)^n]}{(j\omega T_W)^n} \quad (3.21)$$

A perfect one-dimensional diffusion is modelled with $n = 0.5$. $T_W = l_d^2/D_i^{eff}$ where l_d is the effective diffusion thickness and D_i^{eff} is the effective diffusion coefficient of the species i . R_W is the diffusion resistance for $\omega \rightarrow 0$.

An example of the impedance response of a Warburg element is given by the Nyquist plot reported in Figure 3.8 below:

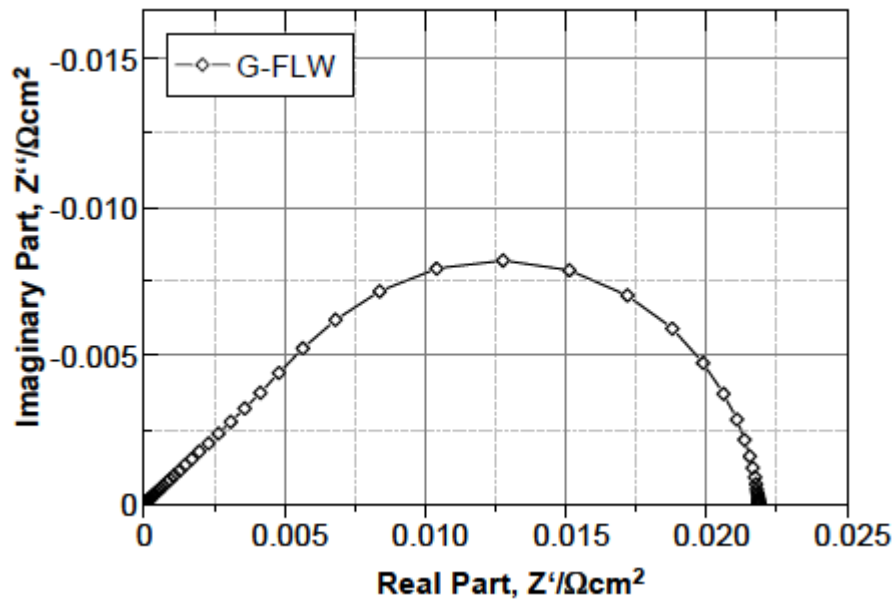


Figure 3.8. Nyquist plot of a Finite-length Warburg element ⁷⁶.

3.4.2. Fitting strategy based on DRT

The major issues in the determination of the ECM and in the CNLS fitting procedure based upon it are related to the choice and the number of circuit elements that constitute the ECM, and to the choice of the initial values for the parameters of the model fitting function ^{20, 22}.

Concerning the former issue, if one considers a typical EIS spectrum as the one reported in Figure 3.2, from what has been stated so far, a plausible ECM model would be a series

connection of a resistance, in order to model the contribution of the ohmic resistance, and 2 simple RC parallels to model the charge transfer mechanisms and the mass transport mechanisms at anode and cathode sides^{77, 78}. In other works, it is reported how ECM models with three or up to five different RC (or R-CPE) parallels can approximate very well the experimental curve; other authors employ other circuit elements, such as the Warburg or the Gerischer element instead of the R-CPE elements, to achieve better fitting results for the modelling of the mass transport phenomena^{26, 79}. It is evident that some sort of ambiguity in the definition of the ECM model is present, which will affect the reliability of the obtained results^{3, 24}.

Considering the choice of the initial parameters for the model fit function, an accurate analysis of both the Nyquist and Bode plots can suggest values of resistances and capacitance to be used as initial fitting values. Nevertheless, in complex electrochemical systems such as SOFCs, numerous physicochemical processes occur contemporaneously; even though EIS is a very sensitive technique, it can hardly distinguish two processes that differ in their characteristic frequency by less than two decades, thus resulting deeply convoluted in the EIS spectrum.

An instrumental tool to overcome both these issues, and thus provide a superior reliability for the ECM-CNLS fitting procedure, may be the analysis of the DRT functions.

Consider the DRT plot calculated from an experimental EIS test performed in this work, and reported in Figure 3.9.

It can be seen that at least five different processes are visible in this spectrum, with five different characteristic frequencies, indicated by the red stars in the plot. This suggests that the ECM model that will be employed for the fitting of the experimental data should possess a maximum of 5 different circuit elements (note that the R_0 element and other elements such as the inductive element to model the inductance of the instrument cable do not have to be considered, since the DRT plot is calculated on the imaginary and negative part of the EIS spectra).

Moreover, observing a single DRT peak of the plot, while the red star indicates the maximum frequency of the process, hence its characteristic frequency, the red cross indicates the end of the it, as also easily appreciable from the DRT response of the dummy-cell model reported in Figure 3.3.

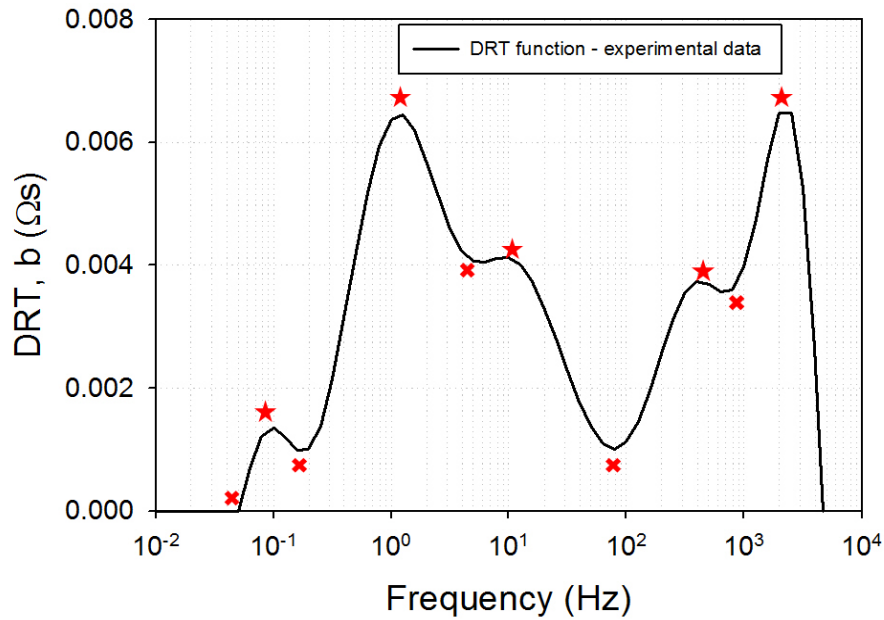


Figure 3.9. DRT function obtained from the experimental EIS recorded from an SOFC sample operating at $T = 700$ °C in humidified hydrogen (H_2 20%, N_2 76%, H_2O 4%).

This means that both the maximum frequency and the frequency at which the process possesses only the real component of the impedance, hence the maximum value of its resistance R_i , can be evaluated. This information allow to extract, from the Bode plot, the values of the modulus of the impedance $|Z_i|$ at the peak frequency and at the minimum frequency, which allow in turn to calculate the initial values of capacitance and resistance, respectively, by means of the equations reported in 3.2.1, for each peak.

In Chapter 4 and 5 an experimental campaign consisting of a set of different experiments in which a SOFC sample is exposed to different operating conditions (such as gas compositions and temperature), in which only a single operating parameter is varied each time, will be addressed in order to identify the nature of the processes underlying each different DRT feature, by studying the different behaviour of each peak in response to a variation of a single operating parameter. The resulting ECM model will be part of the results obtained in this work and will be presented in Chapter 5.

Nevertheless, an example of the goodness of the fitting obtained with this procedure is depicted in Figure 3.9.

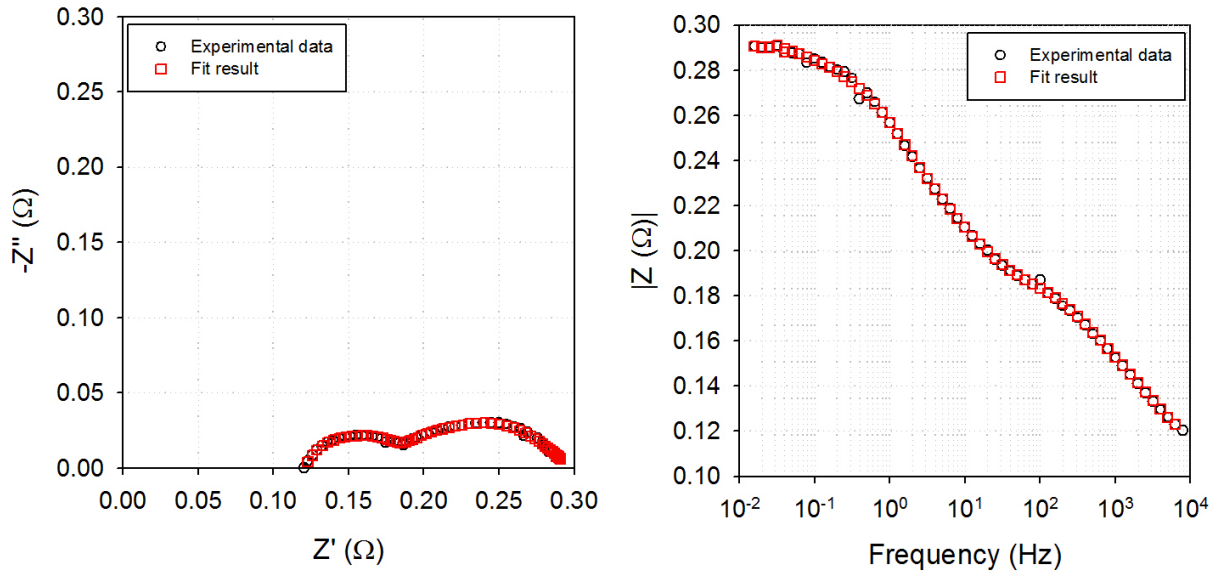


Figure 3.9. Nyquist (left) and Bode (right) plots depicting experimental (black circles) and fit (red squares) points.

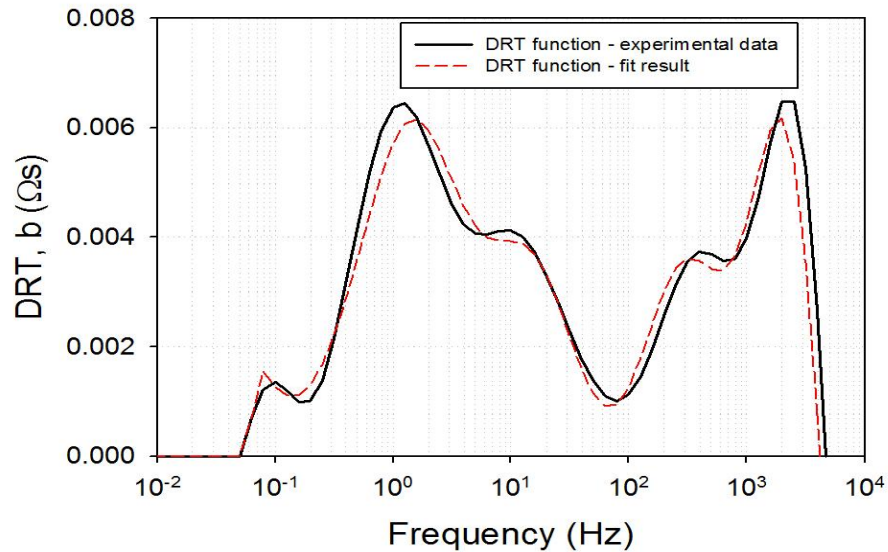


Figure 3.10. DRT functions of the experimental spectrum (black line) and fit (red dashed line) function.

Also from the DRT function calculated from the imaginary part of the model fit function the goodness of the fit can be better appreciated. The comparison between the DRT function calculated from the experimental data and the fit function is reported in Figure 3.10.

3.5. Other characterization techniques

In the following Sections, a brief description of the other characterization techniques employed in the experimental part of this work is addressed. Apart from Gas Chromatography (GC), the other techniques were employed to perform *post-mortem* analysis of the tested samples. Being not a fundamental part of this work, for more details about these techniques, the reader is referred to more specific readings.

Gas Chromatography (GC)

Gas Chromatography is an analytical technique of great importance for the analysis of the compositions of gas mixtures.

It is based on the different times of retention that different gas species possess when they pass through a stationary phase (solid phase), carried by a mobile phase (gas carrier). Depending on the molecular weight and physical properties, the single gas species will pass through the stationary phase and reach a specific detector placed at the end of the column at different times, called elution (or retention) times.

The result of this analysis is a gas chromatograph which reports the intensity of the different peaks related to the gas species detected as a function of the elution time.

From a gas chromatograph qualitative information can be obtained based on literature data about the elution time of single species (most often employed in databases within the analysis software provided with the instrument). Quantitative analysis can be further performed comparing the areas of the peaks, on a percentage basis: the ratio between the areas of two peaks will be equal to the ratio of their concentration in the gas mixture.

X-Ray Diffraction (XRD)

X-Ray Diffraction (XRD) spectroscopy is a technique for the analysis of the crystalline structure of solid samples. The resulting spectrum is produced by the diffraction of X rays that hit the sample and are scattered by the atoms comprised in the crystalline reticulate. Each phase has a characteristic diffraction pattern, which is univocally related to the geometrical distribution of

elements within the crystalline reticulate, thus resulting specific of each crystalline phase. It provides information about the solid phases present in the bulk of the sample, and it is useful in SOFC investigations to assess if new phases are formed after a prolonged operation of the cell, or due to detrimental effects related to the presence of contaminants in the fuel stream.

Raman Spectroscopy

Raman Spectroscopy is a very sensitive technique that provides information about the chemical composition, the nature of the bonds, the chemical environment and the crystalline phases of the tested samples. It was first invented by the physician C. V. Raman, who discovered that a small fraction of the radiation diffused by a sample had a different energy content with respect to the incident one, and that this difference was related to the chemical structure of the sample (*Raman effect*). A monochromatic radiation is sent to a sample, most often in the visible spectrum; considering the interaction between the radiation and the matter in terms of collision between particles, the photons merging by these interaction (back-scattered) may be affected by an elastic or inelastic interaction. The former event is the most probable, but it does not contain information about the nature of the sample; the latter, having lost or acquired energy, carries with it the information of the excitation of the atomic or molecular bonds within the sample.

Similar to the XRD analysis, the Raman spectrum is characteristic for each species, so the identification of the phases is possible by means of literature data.

In contrast with the XRD analysis, the information provided by the Raman spectroscopy comes from the very first layers upon the surface of the as received sample.

Scanning Electron Microscopy (SEM) and Energy - Dispersive X-ray spectroscopy (EDX)

Electron microscopes are based on the same principles as light microscopes, but focus beams of energetic electrons rather than photons to generate a high resolution image of the surface of the sample. The capability of investigating the microscopic features of certain samples enables a comprehensive evaluation of the morphological evolution due to the operating conditions and degradation phenomena. Moreover, energetic electrons that hit the atoms of the sample cause an excitation of the atomic energetic state which, due to the following relaxation, releases a radiation in the X-ray spectrum. Based on this phenomenon, the energy dispersive x-ray spectroscopy

provides information about the chemical composition of the sample, in terms of concentrations of the different elements. SEM allows an in-depth analysis of the sample down to the micron and submicron scale, which can be further used to estimate geometric parameters such as the pore radii, the particle radii and the thickness of the layers.

4. EXPERIMENTAL MATERIALS, METHODS AND PROCEDURES

In this chapter, the technical details for the realization of the experiments presented in this work are addressed.

In the first part of this section, along with the characteristics of the tested samples and the description of the equipment of the test stations, the design and realization of an innovative, in-house built, multisampling cell housing for the local measurement of temperatures and gas compositions *in operando* is presented in Section 4.3.

In the second part of this chapter, the testing procedures and conditions adopted for the realization of all the experiments described in this work are summarized.

4.1. Tested samples

All the cells studied in this work are planar, anode supported, Intermediate Temperature Solid Oxide Fuel Cells (IT-SOFC), manufactured by Elcogen AS (Tallinn, Estonia). The cells employ a porous Ni-8YSZ anode (c.a. 400 μm), divided in a thick anode substrate and a thin anode functional layer (AFL), a thin (c.a. 5 μm) dense 8YSZ electrolyte, a GDC diffusion barrier layer and an LSC cathode layer (c.a. 15 μm).

The anode substrate was produced by tape casting of NiO-YSZ suspensions; upon this substrate, the electrolyte layer was deposited by tape casting a dense 8YSZ suspension and sintered to form a dense film. The GDC diffusion barrier and the LSC cathode layer were applied by subsequent screen printing and sintering processes.

Table 4.1 summarizes the materials and thicknesses of all the layers.

	Materials	Thickness (μm)	Operating Temperature ($^{\circ}\text{C}$)
Anode	Ni-YSZ	405 ± 20 (anode + electrolyte)	600-700 $^{\circ}\text{C}$
Electrolyte	YSZ		
Diffusion barrier layer	GDC	15 ± 5 (cathode + barrier)	
Cathode	LSC		

Table 4.1. Materials and thicknesses of tested cells.

Three different sizes of cell were tested: button cell size (active area: 2 cm²) and single cell size (active area: 81 cm² or 121 cm²), as depicted in Figure 4.1 below.

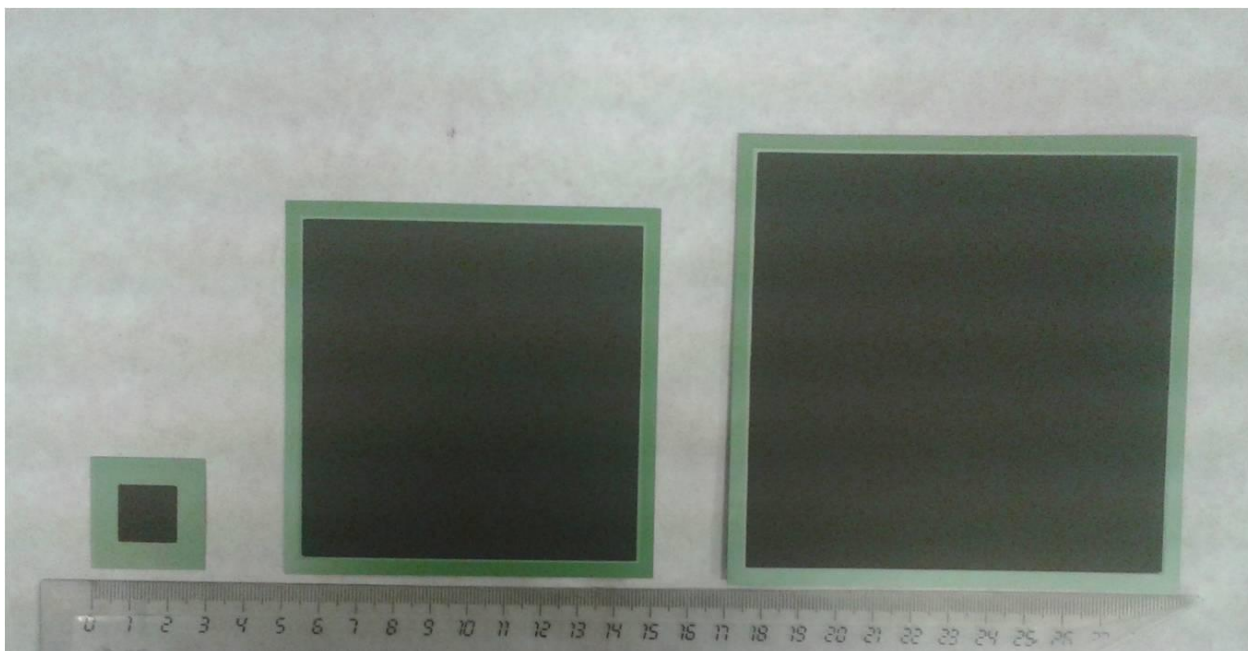


Figure 4.1. Different cell samples tested in this work.

Button cell samples were employed for the electrochemical characterization and evaluation of single physicochemical processes, for the study of their evolution during long operation and for the evaluation of the effects of a tar contaminant.

Single cell samples were used in order to study the distribution of temperatures and gas compositions along the anode surface, and the evolution of chemical and electrochemical reactions *in operando* by means of the multisampling set-up developed in this work, and extensively described in Section 4.3 below.

4.2 Button cell test station

The button cell test rig consists of a temperature programmed oven, in which a SOFC button cell sample is inserted by means of an alumina cylindrical support; on the top of it, the button cell sample is fixed by a high-temperature refractory paste, which, after being baked under the manufacturer specifications, ensures also the gas tightness. The cell is held vertically and two current collectors, one consisting of a nickel mesh for the anode side, and another one consisting of a gold mesh for the cathode side, are placed in contact with the two electrodes of the sample.

A thermocouple for the measurement of the temperature of the cell is placed very close to the sample.

The test rig employs a set of mass flow controllers (MFCs) to allow the cell to be fed with hydrogen or simulated syngas at the anode side, and with air, enriched or depleted in its O₂ content, at the cathode. A bubbling humidifier placed in a Haake D8 Fisons thermostat circulator is used for the humidification of the anode stream.

A refillable permeation tube is employed to evaporate liquid toluene, as a single component representation of tars, and mix in the fuel stream by means of a sweep gas (N₂); the concentration of toluene in the resulting tar-contaminated syngas is set adjusting the temperature of the permeation tube environment with a Julabo UC-5B temperature controlled water circulator, and by varying the flow rate of the sweep gas.

The gas pipelines going from the bubbler to the anode inlet, and that containing the sweep gas for the tar evaporating system are heated by heating strips, to avoid condensation of both water and toluene.

The test bench is equipped with an Agilent E3634A DC power supply which can act as a DC electronic load too, an Agilent 34970A data logger, and a LABVIEW-based control software, in order to perform the polarization curves, and with a Solartron 1260 Impedance Gain/Phase Analyzer module coupled with a Solartron 1287 Electrochemical Interface for the electrochemical impedance spectroscopy measurements.

Fig. 4.2 depicts the test-rig, together with a magnification of the button cell housing.

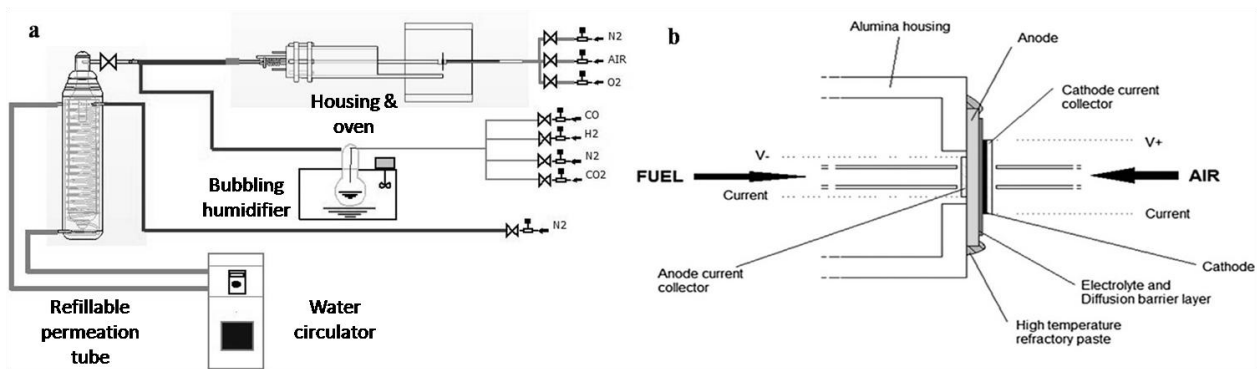


Figure 4.2. Schematic representation of the button cell test-rig (a) and of the button cell housing (b).

4.3 Multisampling cell housing

In this work, and within the framework of the European project NELLHI (New all European high performance stack: design for mass production, grant agreement no. 621227) an innovative experimental setup for in-depth characterizations of Solid Oxide Fuel Cells has been developed.

In this section, the design, the realization, and the assembly of a novel, in-house designed, multisampling housing will be described.

4.3.1 Design and Realization

The idea behind this project is to realize a setup enabling the sampling of temperature and gas compositions localized on the anode surface, in order to collect data on the evolution of anodic reactions along the surface. Thus, chemical and temperature gradients will be available, and can be recorded during selected modes of operation of the cell, thereby increasing and deepening the level of characterization of the cells. This is particularly important for the direct fuelling of IT-SOFC cells with syngas, where the dynamic processes of internal reforming and water gas shift reactions can create severe local gradients of temperature and gas compositions, inducing stresses and possible carbon deposition. Moreover, the novel housing has to allow electrochemical characterization, such as polarization curves and electrochemical impedance spectroscopy (EIS), not affecting (or at least with minor contributions) the cell response during the characterization.

The design was realized in the ENEA Casaccia HOTLAB, and is depicted in Figure 4.3. It consists of a number of levels separated by frame-shaped layers of gaskets, made of Thermiculite

866LS or CL87 manufactured by Flexitallic, a partner of the project. This multi-layer configuration is meant to provide both gas tightness and electrical insulation of the SOFC cell from the housing.

This setup has been realized in two different dimensions, in order to allocate the 10x10 cm² (active area 81 cm²) and the 12x12 cm² (active area 121 cm²) single cells manufactured by Elcogen AS.

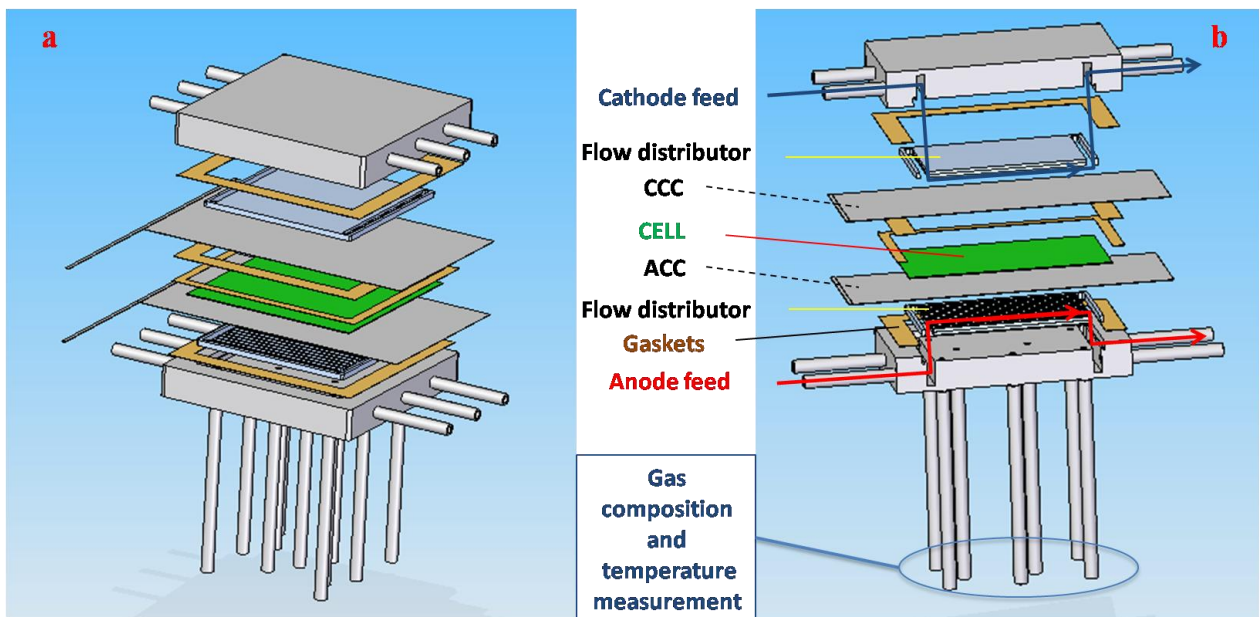


Figure 4.3. Exploded view (a) and cross section (b) drawings of the multisampling housing.

4.3.2 Materials and Manufacturing

Steel housing

Anodic and cathodic cases are made of AISI 310 stainless steel.

Gas inlet and outlet tubes are made of Inconel, which is a material supposed to form a thick and stable passivating oxide layer on its surface, avoiding the chromium evaporation and, thus, the cell contamination. Three short tubes are welded on the two opposite side of the case, providing a

better gas supply, and, on the other extremity, they are joined together to a longer and larger tube, which comes out from the furnace.

The anodic case has been drilled on the surface for gas sampling, which is performed by means of capillary tubes, made of AISI 310 stainless steel, welded in correspondence to the holes.

On the surface of both anodic and cathodic cases, a square shaped seat has been designed for the accommodation of the gas distribution plate.

All the cases and tubes, together with the welding of the latter, were manufactured by RMP s.r.l. (Italy), based on the supplied designs.

Gas distribution plates

Gas distribution plates are made of AISI 310 stainless steel.

Both anodic and cathodic plates have a set of parallel gas distribution channels, that connects the gas inlet and outlet, placed on the two opposite sides.

The anodic plate possesses also a set of holes in correspondence of those placed on the anodic case.

To avoid electrical contact with current collectors and chromium evaporation, a layer of insulating Al_2O_3 has been deposited on the surface of the whole plate.

Current collectors

Anodic current collectors consist of a Crofer 22H stainless steel calendered mesh on which a series of Pt wires are welded on one side, very close to each other, and rolled together to form a bundle for the collection of the current. A single Pt wire is welded on the opposite side of the mesh, for the measurement of the cell potential.

Cathodic current collectors consist of a gold (or Crofer 22H) calendered mesh, on which Pt wires are welded similarly to those on the anode mesh.

Current collectors were manufactured by Fiaxell (Switzerland).

Gaskets

Gaskets consists of Thermiculite 866LS or Thermiculite CL87, provided by Flexitallic Ltd. (UK), hand-cut into frames according to the case dimensions.

4.3.3 Placement and role of components

Steel housing

The bottom of the entire setup is the anodic case. Its first function is to provide fuel gas and remove the exhaust by means of the lateral inlet and outlet tubes, respectively, that communicate to the cell by means of long cavity machined in both sides of the case.

The second function is to allow gas sampling from the SOFC anode surface, through a set of 11 capillary tubes distributed along the entire corresponding SOFC surface. Moreover, localized temperature measurement may be achieved by means of thin thermocouples inserted inside the capillary tubes, ending in the immediate proximity of the corresponding holes.

The cathodic case represents the top of the whole setup. Its only scope is to provide oxidant gas to the SOFC cathode and remove the exhaust, similarly to its anodic counterpart. Localized gas sampling and temperature measurement cannot be performed, since the top of the cathodic case must be planar to apply the mechanical load.

Gas distribution plates

Gas distribution plates are positioned inside the cases, into a slot specifically manufactured on them. They merge slightly from the surface, to provide contact with SOFCs electrodes. They are also equipped with a series of parallel gas channels, in order to realize a homogeneous gas distribution along the cell surfaces, that connects two side-pipes, perpendicular to the gas channels, for the inlet and the outlet of gases.

Moreover, the anodic gas distribution plate is equipped with a set of 11 holes for localized gas sampling, with a peculiar distribution. This distribution has been designed to cover the most important regions of the surface, with the least number of holes.

As can be seen in Fig. 4.4, two groups of three holes are distributed along the y and y' axes, in proximity of gas inlets and outlets. In this way, it is possible to analyse the initial and the final compositions coming from the anode surface, both from the corners and in the middle.

Moreover, the gas distribution on the centre of the anode surface is measurable from 5 different spots, distributed in an asymmetrical array.

Along the gas flow direction, the gas composition can be monitored in 5 progressive axial locations, resulting in an efficient mapping of surface composition.

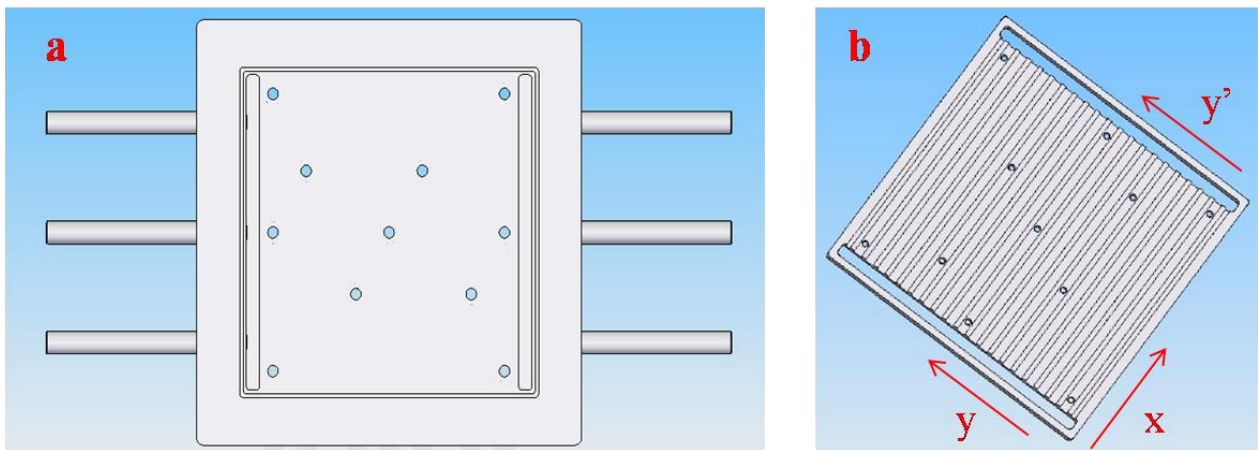


Figure 4.4. Top view of the anodic case (a) and of the anodic gas distribution plate (b) with 11 sampling ports shown.

Finally, a temperature mapping of the surface can be generated positioning a thermocouple in proximity of each spot.

If the surface of both anodic and cathodic gas distribution plates is made perfectly insulating, the result is the measurement of electrical properties of the sole cell, avoiding contributions from the rest of the setup.

Current collectors

Current collectors are placed between the gas distribution plates and the SOFC cell, in contact with its electrodes. They are manufactured to be perfectly flat, ensuring a good contact with cells electrodes. They are equipped with a bundle of Pt wires for the collection of the current on one side, and a single Pt wire, placed on the opposite side, for the recording of the voltage. In order to

avoid gas leakages caused by the roughness coming from the welding spots of the wires, current collectors have a length which exceed the housing dimensions, emerging from it on the two sides.

Gaskets

To ensure gas tightness and electrical insulation of each component, a set of 4 Thermiculite gaskets, shaped as square frames, are required.

Three of them have the dimensions of the frame on the case surface (see Figure 4.3.a); the other one is cut in the centre in order to perfectly contain the SOFC.

Two gaskets are placed between the current collectors and the respective steel case, avoiding, at the same time, gas leakages from the housing, and electrical contact between current collectors and the housing; with this disposition the cell results effectively insulated from the housing.

The other two gaskets are placed at the cell level. One of them contains the cell, while the other one covers the exposed surface of the electrolyte on the cathode side, in order to avoid short circuiting between the electrodes. Moreover, these gaskets provide gas tightness at cell level, and avoid the contact between the two current collectors.

4.3.4 SOFC Cell Assembly

In this part, the assembly of a SOFC single cell (81 cm² active area) into the novel housing is reported.

- *Step 1:* the anodic steel case is positioned into the furnace, with the gas sampling capillary tubes merging from the bottom, outside the furnace. The ends of these capillaries are closed by means of valves. On the top of the anodic case, one of the Thermiculite gaskets is fixed using a spray glue, and the anodic gas distribution plate is placed into its slot (see Figure 4.5.a).
- *Step 2:* the anodic current collector is placed on the gas distribution plate, followed by the single cell. Two gaskets are placed at this level: one surrounds the cell, and the other one is placed on the top of the former, covering the electrolyte exposed on the cathode side, to avoid short circuiting of the electrodes (see Figure 4.6.b).

- *Step 3:* cathode current collector is positioned in contact with the SOFCs cathode, rotated 90° with respect to the anode current collector, to avoid possible short circuit caused by the bending of the former on the latter. (See Figure 4.7.c). Meanwhile, the last Thermiculite gasket is fixed along the edge of the cathodic case, and the cathodic gas distribution plate is paced into its slot (See Figure 4.8.d).
- *Step 4:* Finally the cathodic case is placed on the top of the current collector, closing the setup (Figure 4.9.e). A mechanical load is placed over the setup, and the furnace is insulated with alumina bricks (Figure 4.10.f).

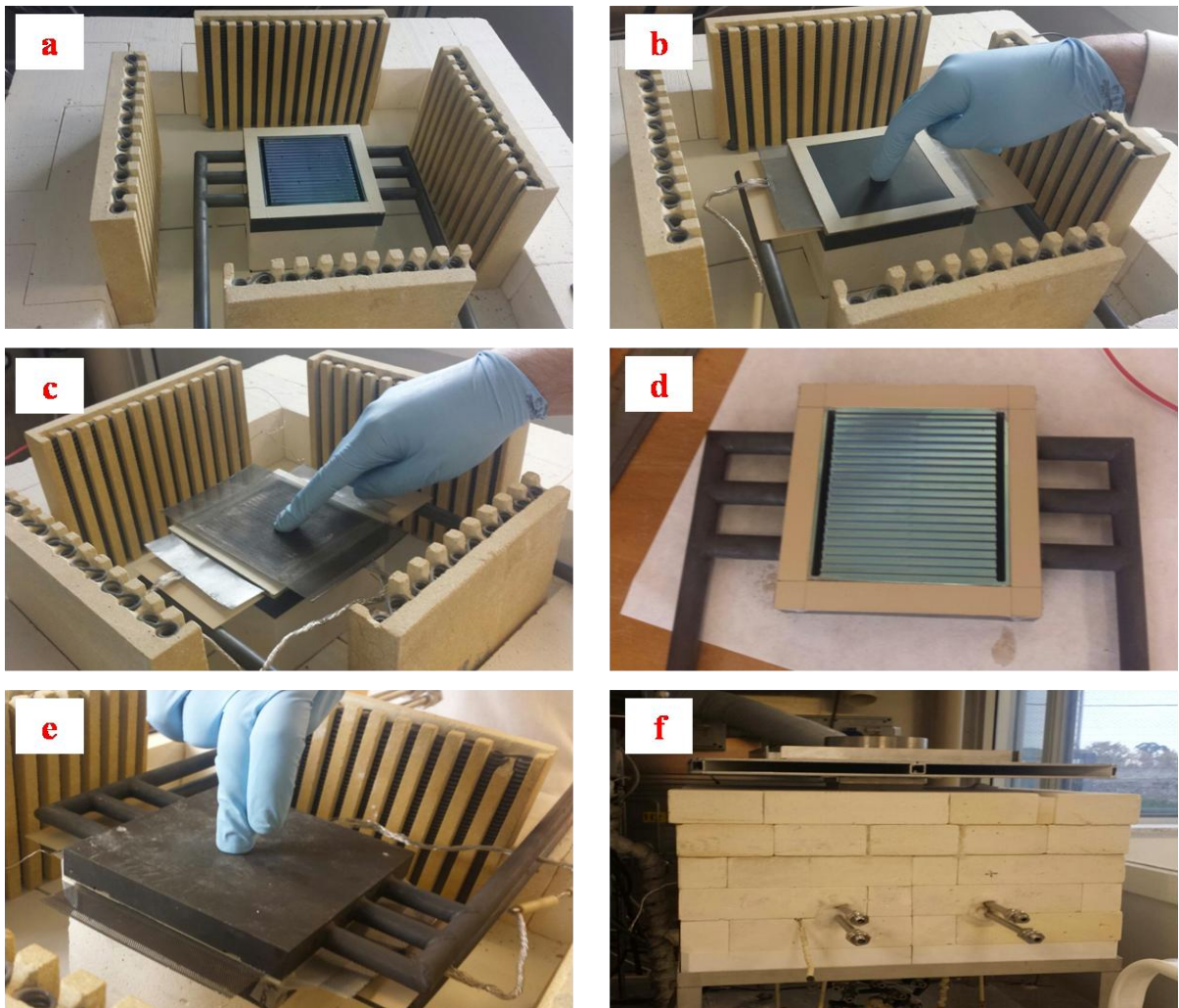


Figure 4.10. Different stages of cell assembly

4.4 Single cell test station

In Figure 4.11 the piping and instrumentation diagram of the single cell test station is reported.

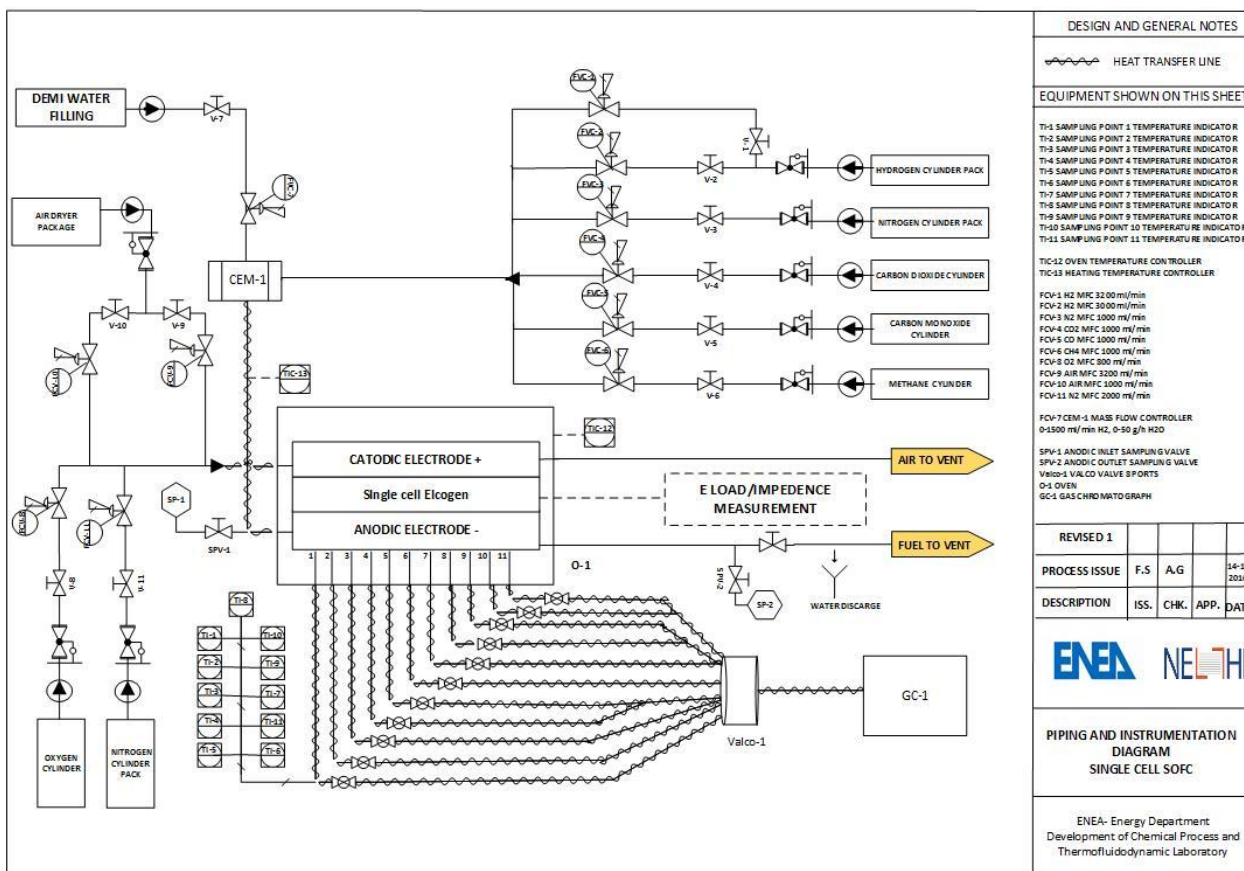


Figure 4.11. Piping and instrumentation diagram of the single cell test bench.

The single cell test bench is equipped with a temperature programmed oven, in which the single cell housing is inserted. The eleven sampling capillary tubes merge from the bottom of the furnace, and converge to a multi-stage Valco valve, which selectively drives the gas coming from a single sampling spot to a Perkin-Elmer Clarus 680 GC gas-chromatograph. In order to reduce the pressure drop on the cell, and to avoid the mixing of the gas of different sampling spots, each capillary is also equipped with a single valve. A thermocouple (Type K) is inserted inside each capillary tube, ending in the immediate proximity of the corresponding holes. A set of mass flow controllers are employed to allow the cell to be fed with H₂, CO, CO₂, CH₄ and N₂; the fuel gas can be humidified by means of a controlled evaporator mixer and a liquid flow meter. On the

cathode side, air is provided by a mass flow controller, and it can be further enriched or depleted in its oxygen content by means of dedicated mass flow controllers for N₂ and O₂. Anode exhaust is driven to an hermetic glass container for the water condensation, and the exhaust gas is then led to the vent. The cathode exhaust is driven to the vent too. The anode and cathode inlets, and the capillary tubes are all trace heated in order to avoid water condensation. The test bench is equipped with a Kikusui PLZ664WA electronic load connected in series with a Delta Elektronika SM-30-100D power supply to record the polarization curves, measuring the cell potential by means of an TTI 1604 digital multimeter, and with a Solartron 1260 Impedance Gain/Phase Analyzer module coupled with a Solartron 1287 Electrochemical Interface for the electrochemical impedance spectroscopy measurements.

4.5 Preliminary testing procedures

The experimental procedure and the testing conditions for the evaluation of the immediate performances of the SOFC samples studied are reported in this section.

4.5.1 Button cells

The button cell samples were heated up to 700° C, with a temperature ramp of 0.5 °C·min⁻¹ under 25 ml·min⁻¹·cm⁻² of N₂ to the anode and 50 ml·min⁻¹·cm⁻² of air to the cathode. They were then reduced at 700 °C, progressively changing the flows to 75 ml·min⁻¹·cm⁻² of H₂ with 4 mol% humidification to the anode and 125 ml·min⁻¹·cm⁻² of air to the cathode. Once the cells were fully reduced the first acceptance trials were carried out: considering the cell voltage as previously expressed in Equation 2.9, at OCV condition the only contribution to the voltage drop is determined by η_{leak} . If voltage loss was below 5% (Equation 4.1), leakages were considered to be negligible and the correspondent cell was valid for further testing.

$$\Delta E_N(\%) = \frac{E_{N,theoretical} - E_{N,measured}}{E_{N,theoretical}} \cdot 100 \quad (4.1)$$

In Equation (4.1) ΔE_N denotes the voltage loss due to leakage, $E_{N,theoretical}$ is the theoretical Nernst voltage calculated by means of Equation 2.8 and $E_{N,measured}$ is the potential experimentally measured.

BC	Theoretical voltage (mV)	Measured voltage (mV)	Voltage loss (%)
01	1115	1080	3.1
02	1115	1090	2.2
03	1115	1090	2.2
04	1115	1080	3.1
05	1115	1087	2.5
06	1115	1077	3.4

Table 4.2. Theoretical and measured Nernst potential at 700 °C along with the voltage loss due to leakage expressed as a percentage for the abovementioned gas compositions.

After the reduction procedure, in the same conditions of gas flows and temperature, a polarization curve was recorded from OCV condition to the maximum current value at which the voltage of the cell was above 600 mV, increasing the current with a step rate of $50 \text{ mA}\cdot\text{min}^{-1}$. Afterwards, an EIS spectrum was recorded in the same conditions, at OCV, from 100 kHz to 10 mHz and with an amplitude of 10 mV.

4.5.2 Single cells

The single cell samples were heated up to 700° C, with a temperature ramp of $0.5 \text{ }^\circ\text{C}\cdot\text{min}^{-1}$ under $6.17 \text{ ml}\cdot\text{min}^{-1}\cdot\text{cm}^{-2}$ of N_2 to the anode and $6.17 \text{ ml}\cdot\text{min}^{-1}\cdot\text{cm}^{-2}$ of air to the cathode. They were then reduced at 700 °C, progressively changing the flows to $13.71 \text{ ml}\cdot\text{min}^{-1}\cdot\text{cm}^{-2}$ of H_2 to the anode and $32.63 \text{ ml}\cdot\text{min}^{-1}\cdot\text{cm}^{-2}$ of air to the cathode. The leakage value has been evaluated as previously mentioned.

SC	Theoretical voltage (mV)	Measured voltage (mV)	Voltage loss (%)
01 (81 cm ²)	1230	1144	6.9
02 (121 cm ²)	1230	1178	4.2

Table 4.3. Theoretical and measured Nernst potential at 700 °C along with the leakage value expressed as a percentage for the abovementioned gas compositions.

In the case of SC_01 (active area 81 cm²) a higher value of leakages was measured. However, for the experimental campaign carried out on this cell, described hereafter, this value was still considered acceptable. After the reduction procedure, in the same conditions of gas flows and temperature, a polarization curve was recorded from OCV condition to the maximum current value at which the voltage of the cell was above 600 mV, increasing the current with a step rate of 0.1 A·s⁻¹. Afterwards, an EIS spectrum was recorded in the same conditions, at OCV, from 100 kHz to 10 mHz and with an amplitude of 10 mV.

4.6 Button cells testing conditions

The experimental procedure and testing conditions for the identification and estimation of the physicochemical processes, for the study of the long-term behaviour of the cells and for the investigation of a tar contamination of the fuel on the SOFCs processes are summarized hereafter.

4.6.1 Process identification

In order to ascribe each peak identified from DRT functions to a single physicochemical process, and to estimate the values of several parameters contained in the fundamental equations that regulate the operation of an SOFC (see Chapter 2), the button cell samples were operated under a number of different conditions, varying only one operating parameter at a time: temperature, fuel type and gas composition. For each condition, an EIS measurement was recorded, and the DRT function was calculated from the experimental data acquired. Tables 4.4, 4.5, 4.6, 4.7. resume all the gas compositions tested, expressed in molar fractions, which were undertaken at three different temperatures: 650 °C, 675 °C and 700 °C.

The fuel types tested were H₂/H₂O, CO/CO₂ and syngas mixtures, in order to first identify the processes in the simpler gas compositions, where the only expected reaction is the

electrochemical conversion of the fuel, and then to study a more complex composition (syngas, which contains all the components of the first two gas mixtures) where other processes can occur. The total flow at the anode was set to $75 \text{ ml}\cdot\text{min}^{-1}\cdot\text{cm}^{-2}$, while the total flow at the cathode side was set to $125 \text{ ml}\cdot\text{min}^{-1}\cdot\text{cm}^{-2}$.

In the case of CO/CO₂ operation, high molar fractions of CO₂ were provided in order to limit the occurrence of the carbon deposition phenomenon.

In the case of syngas operations, gas compositions were chosen in order to be comparable with the results obtained from the variations of gas composition performed in the case of H₂/H₂O and in CO/CO₂ fuels. Due to the chemical equilibrium related to the Water Gas Shift reaction (WGS), a variation of x_{H_2} implies a variation of x_{CO} , while a variation of $x_{\text{H}_2\text{O}}$ implies a variation of x_{CO_2} . Hence, molar fractions of H₂ and CO and molar fractions of H₂O and CO₂ were set with the same value, and gas flows were slightly adjusted according to the equilibrium constant of the water WGS reaction (see Equation 2.23), for each temperature, in order to realize equilibrium fuel gas compositions. Furthermore, the variations of the O₂ content at the cathode side were performed both in H₂/H₂O and in CO/CO₂ fuels. for simplicity, Table 4.6. reports the syngas compositions only for the case at T = 700°C.

T		H ₂ variations					H ₂ O variations			
650 °C, 675 °C, 700 °C		I	II	III	IV	V	I	II	III	IV
Anode gas	H ₂	0.10	0.20	0.30	0.40	0.96	0.80	0.80	0.80	0.80
	H ₂ O	0.04	0.04	0.04	0.04	0.04	0.05	0.10	0.15	0.20
	N ₂	0.86	0.76	0.66	0.56	0.00	0.15	0.10	0.05	0.00
Cathode gas	O ₂	0.21	0.21	0.21	0.21	0.21	0.21	0.21	0.21	0.21
	N ₂	0.79	0.79	0.79	0.79	0.79	0.79	0.79	0.79	0.79

Table 4.4. Test matrix containing the molar fractions of gas species for the DRT analysis under H₂–H₂O operation.

T 650 °C, 675 °C, 700°C		CO variations				CO ₂ variations			
		I	II	III	IV	I	II	III	IV
Anode gas	CO	0.10	0.20	0.30	0.40	0.10	0.10	0.10	0.10
	CO ₂	0.60	0.60	0.60	0.60	0.20	0.30	0.40	0.50
	N ₂	0.30	0.20	0.10	0.00	0.70	0.60	0.50	0.40
Cathode gas	O ₂	0.21	0.21	0.21	0.21	0.21	0.21	0.21	0.21
	N ₂	0.79	0.79	0.79	0.79	0.79	0.79	0.79	0.79

Table 4.5. Test matrix containing the molar fractions of gas species for the DRT analysis under CO– CO₂ operation.

T 700°C		H ₂ - CO variations				H ₂ O - CO ₂ variations			
		I	II	III	IV	I	II	III	IV
Anode gas	H ₂	0.10	0.20	0.30	0.40	0.30	0.30	0.30	0.30
	H ₂ O	0.04	0.04	0.04	0.04	0.05	0.10	0.15	0.20
	CO	0.10	0.20	0.30	0.40	0.19	0.19	0.19	0.19
	CO ₂	0.06	0.06	0.06	0.06	0.05	0.10	0.15	0.20
	N ₂	0.70	0.50	0.30	0.10	0.41	0.31	0.21	0.11
Cathode gas	O ₂	0.21	0.21	0.21	0.21	0.21	0.21	0.21	0.21
	N ₂	0.79	0.79	0.79	0.79	0.79	0.79	0.79	0.79

Table 4.6. Test matrix containing the molar fractions of gas species for the DRT analysis under syngas operation.

		O ₂ variations				O ₂ variations				
		I	II	III	IV	I	II	III	IV	
Anode gas	H ₂	0.96	0.96	0.96	0.96	CO	0.40	0.40	0.40	0.40
	H ₂ O	0.04	0.04	0.04	0.04	CO ₂	0.60	0.60	0.60	0.60
	N ₂	0.00	0.00	0.00	0.00	N ₂	0.00	0.00	0.00	0.00
Cathode gas	O ₂	0.04	0.08	0.21	0.50	O ₂	0.04	0.08	0.21	0.50
	N ₂	0.96	0.92	0.79	0.50	N ₂	0.96	0.92	0.79	0.50

Table 4.7. Test matrix containing the molar fractions of gas species for the DRT analysis for oxygen variations.

4.6.2. Endurance performance in syngas

A button cell sample was operated at $T = 650^{\circ}\text{C}$ under a constant current density of $0.5 \text{ A}\cdot\text{cm}^{-2}$ for 1000 hours, with the aim of evaluating the temporal evolution of the processes determining the overall performances and investigate whether the reduced operating temperature could compromise the feeding of SOFCs with a syngas. The cell was fed with the syngas composition reported in Table 4.8 below, which approximates that obtained from a steam-enriched air gasification of biomass. In this case the total flow at the anode was set to $48.4 \text{ ml}\cdot\text{min}^{-1}\cdot\text{cm}^{-2}$, while the total flow at the cathode side was set to $41.5 \text{ ml}\cdot\text{min}^{-1}\cdot\text{cm}^{-2}$, according to FCTSQA⁸⁰ standard test modules.

During the operation, EIS measurements were performed with the same specifications described previously (Section 4.5), and the DRT functions were calculated from the imaginary part of the experimental spectra.

	Anode gas					Cathode gas	
	H ₂	H ₂ O	CO	CO ₂	N ₂	O ₂	N ₂
x _i	0.25	0.10	0.15	0.14	0.36	0.21	0.79

Table 4.8. Molar fractions of the anode and cathode gasses employed for the long-term test under constant current density.

4.6.3. Tar contamination

As described in Section 2.3.3, tars are considered one of the most harmful classes of compounds for safe operation of SOFCs with syngas produced from gasification of biomass. In order to evaluate the effect of a tar contaminant in the fuel stream of an IT-SOFC, a button cell sample was employed for tests with tar-contaminated syngas at different concentrations. For this test, toluene was chosen as a model tar, being one of the most reactive and concentrated species in tar mixtures coming from biomass gasifiers.

All the compositions tested in this characterization are listed in Table 4.9. All compositions reported were tested in succession, in this order.

	H ₂	H ₂ O	CO	CO ₂	N ₂	Toluene (mg·m⁻³)
Tar A	0.25	0.10	0.15	0.14	0.36	536.5
Tar B	0.25	0.10	0.15	0.14	0.36	424
Tar C	0.25	0.10	0.15	0.14	0.36	318.6
Tar D	0.25	0.10	0.15	0.14	0.36	254.9

Table 4.9. Fuel compositions tested with different toluene concentrations.

Polarization curves and EIS measurements were recorded with the same modality described in Section 4.5.

An endurance test was then performed on the sample exposed to the composition Tar D, and the cell was operated with a constant current density of $i = 0.4 \text{ A}\cdot\text{cm}^{-2}$ for up to approximately 150 hours; during the operation, i-V curves and EIS spectra were collected.

4.7. Single cells testing conditions

In order to investigate the evolution of chemical reactions occurring during the operation of the cell, identified with a spatial resolution covering the whole surface of the anode, single cell samples were operated in the multi-sampling housing described in Section 4.3, with dry H₂ and syngas fuels. Detailed spatial mapping of thermo-chemical response of the cells were experimentally obtained *in-operando*, with local measurement of gas compositions and temperature, allowed by the novel setup presented previously. The details of these experimental campaigns are reported in Sections 4.7.2. and 4.7.3; a preliminary validation of the multi-sampling set-up was carried out according to the modality described in Section 4.7.1.

4.7.1 Validation of the multi-sampling housing

The innovative set up was tested on 10x10 cm² (active area 81 cm²) and 12x12 cm² (active area 121 cm²) intermediate temperature solid oxide fuel cells operating in dry H₂ for the validations of cell performance. In Table 4.9. and Table 4.10. the flows provided to the 10x10 cm² and 12x12 cm² cells during the performance evaluation are reported. Air was provided at the cathode side.

Anode	Flows [ml/min]	Percentage [%]
H ₂	660	100
N ₂	0	0
Cathode		
Air	1470	100

Table 4.9. Gas flows for the performance evaluation of the 10x10 cm² cell.

Anode	Flows [ml/min]	Percentage [%]
H ₂	986	100
N ₂	0	0
Cathode		
Air	2196	100

Table 4.10. Gas flows for the performance evaluation of the 12x12 cm² cell.

The operating temperature was set to 650°C, and a polarization curve was performed as described in Section 4.5.2, and compared to the performances obtained from a project partner (CUTEC) on similar cell samples.

4.7.2. Hydrogen operation

Temperature and gas sampling analysis were performed in a mixture of dry H₂/N₂ as reported in Tables 4.11 and 4.12 below. Air was provided at the cathode side. The thermo-chemical mapping of the tested cells was achieved under two different operating conditions: in OCV condition and with a fuel utilization of 40 %. The operating temperature was set to 650°C.

Anode	Flows [ml/min]	Percentage [%]
H ₂	350	50
N ₂	350	50
Cathode		
Air	1500	100

Table 4.11. Gas flows for the temperature and gas sampling of the 10x10 cm² cell, in an H₂ - N₂ mixture.

Anode	Flows [ml/min]	Percentage [%]
H ₂	520	50
N ₂	520	50
Cathode		
Air	2240	100

Table 4.12. Gas flows for the temperature and gas sampling of the 12x12 cm² cell, in an H₂ - N₂ mixture.

For the 10x10 cm² cell (active area 81 cm²), the 40 % of fuel utilization corresponded to a current of 20 A; for the 12x12 cm² cell (active area 121 cm²), the 40 % of fuel utilization corresponded to a current of 30 A.

The current was always increased in steps of 0.1 A·s⁻¹; each operating condition was kept for 3600 s, measuring at the same time the temperature in each sampling spot, by means of a set of thermocouples (type K) connected to a data logger acquisition system (Fukuyama 3000), acquiring simultaneously the temperature of each thermocouple every 500 msec. After the stabilization of conditions, the gas composition in each point was analysed on-line using a Clarus 680-Perkin Elmer gas chromatographer equipped with specific column for the compounds studied (Haysep Q and molecular sieve5A) and a thermal conductivity detector (TCD).

Polarization curves were performed as described in Section 4.5.2.

4.7.3. Syngas operation

Temperature and gas sampling analysis were performed in a mixture simulating a syngas composition coming from the reforming of natural gas: Tables 4.13 and 4.14. below report the flows for the 10 x 10 cm² and for the 12 x 12 cm² cell respectively. Air was provided at the

cathode side. The thermo-chemical mapping of the 10 x 10 cm² cell was achieved under two different operating conditions: in OCV condition and under a current equivalent to a fuel utilization of 40 % (20 A). In the case of the 12 x 12 cm², three different operating conditions were tested: OCV, fuel utilization of 20 % (15 A) and fuel utilization of 40 % (30 A). The operating temperature was set to 650°C.

Anode	Flows [ml/min]	Percentage [%]
H ₂	105	27
H ₂ O	116.22	29.9
CO	18	4.7
CO ₂	89	23.9
CH ₄	60	15.4
N ₂	0	0
Cathode		
Air	1500	100

Table 4.13. Gas flows for the temperature and gas sampling of the 10x10 cm² cell, in the syngas mixture.

Anode	Flows [ml/min]	Percentage [%]
H ₂	140	24.9
H ₂ O	174.33	31.1
CO	23	4.1
CO ₂	133	23.7
CH ₄	90	16.1
N ₂	0	0
Cathode		
Air	1500	100

Table 4.14. Gas flows for the temperature and gas sampling of the 12x12 cm² cell, in the syngas mixture.

Temperature and gas sampling were realized with the procedure described in Section 4.7.2. Polarization curves were performed as described in Section 4.5.2.

5. RESULTS AND DISCUSSIONS

In this chapter, the results of the experimental campaign described in Chapter 4 are presented.

In the first part, the investigation on button cell samples is aimed to identify the physicochemical processes driving the operation of intermediate temperature SOFCs fed with a syngas. To achieve this result, the distributed relaxation times (DRT) method was performed on the experimental EIS spectra obtained from several button cell samples fed with three different fuel mixtures: H₂-H₂O, CO-CO₂ and simulated syngas. From the variation of a single operating parameter each time, the observed response of DRT peaks was ascribed to different electrochemical processes occurring at the anode or at the cathode side, such as charge transfer and mass transport mechanisms. Once the characteristic frequencies of each process were identified, an estimation of several operating parameters contained in the fundamental relationships described in Chapter 2 was achieved, starting from a CNLS fitting of the experimental EIS measurements by means of an ECM model based on the results obtained from the DRT plots, as explained in Chapter 3. From the trends of the different resistances related to the occurrence of each process with the varying of a single operating condition (molar fractions or operating temperature), physical quantities such as activation energies and reaction orders were estimated for the operation of the cells with the different fuels.

With the same methodology, the endurance performances of a syngas fed IT-SOFC button cell were evaluated, identifying which processes suffered from a pronounced degradation, and assigning their behaviour to a particular degradation mechanism, also by means of a post-mortem characterization.

Moreover, the DRT-ECM approach was employed in order to study the detrimental effects of the presence of a model tar contaminant (toluene) in the fuel stream of a syngas fed IT-SOFC sample on a long run. Again, the results obtained from in-operando EIS measurements were correlated to the information obtained from an in depth post-mortem characterization of the cell, and a degradation mechanism was hypothesized.

What stated in the first part of the experimental campaign carried out on button cell samples has a general validity for what concerns the physicochemical processes occurring in the bulk of the

cells. The reduced dimensions of this kind of samples allows to neglect the impact of concentration and temperature gradients arising on an SOFC sample of realistic size.

Nevertheless, SOFC cells can experience significant performance degradation due to the concentration gradients over the anode where the evolution of chemical and electrochemical processes cause severe variations in the local distribution of chemical species, especially with a complex fuel mixture such as a syngas. This may further result in non-homogeneous distribution of the temperature and electrochemical performance, which penalizes the efficiency and durability of the fuel cell.

In the second part of this chapter, a study of the anode processes occurring in a Solid Oxide Fuel Cell (SOFC) in operative conditions, by means of the innovative, in-house experimental setup presented in Chapter 4, is reported. Simultaneous measurement of temperature and gas compositions by means of gas chromatography using eleven points of sampling allowed to detect the variation of thermal and chemical conditions across the anode surface in steady state and in real time. Thus it was possible to investigate the evolution of chemical reactions occurring during the operation of the cell, identified with a spatial resolution covering the whole surface of the anode, in order to distinguish edge effects from bulk processes. The study was carried out in both H_2-N_2 and reformat fuel mixtures, as described in Chapter 4, highlighting the behaviour of the electrochemical oxidation, of water gas shift (WGS) and steam reforming (SR) reactions along the anode surface.

5.1. Process identification

The experimental procedure employed for the identification of the different operating processes was carried out on 4 distinct IT-SOFC samples; however, the tested samples, described in Chapter 4, came from the same batch, and thus they possess similar characteristics. Nevertheless, a preliminary performance characterization was performed on each cell, in order to confirm the comparability of the tested samples and of the results obtained from the subsequent experiments.

As depicted in Figure 5.1, the polarization curves (Figure 5.1.a) show that the overall performances of the tested cells are nearly identical. Only a slight difference in the polarization resistance can be appreciated from the EIS spectra in Figure 5.1.b; nevertheless, the tested samples can still be considered comparable for the objectives of the experimental campaign in

which they have been employed. The measurements reported in Figure 5.1. were realized in the conditions described in Section 4.5.1.

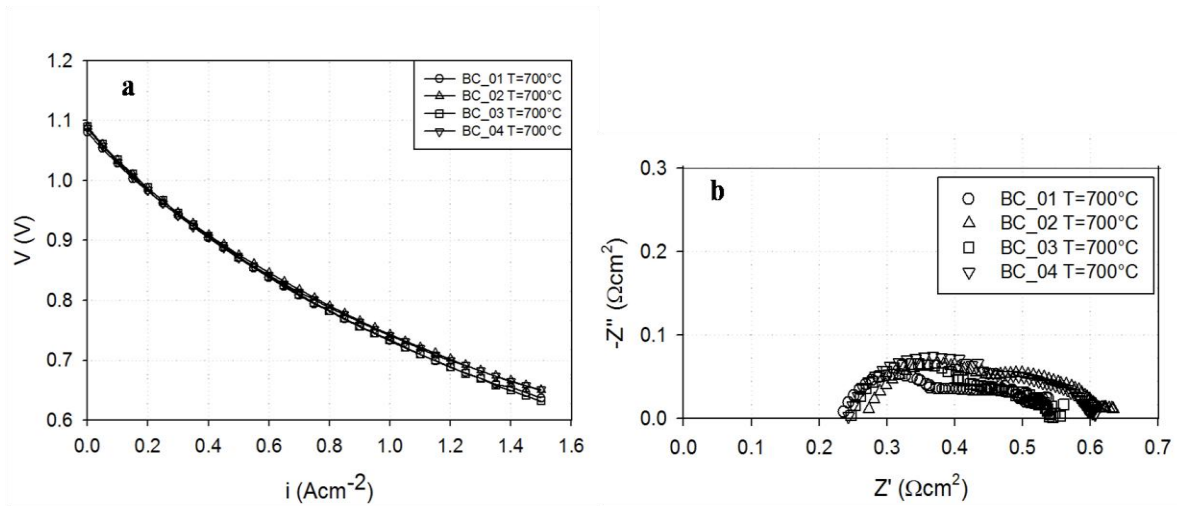


Figure 5.1. Polarization curves (a) and EIS spectra (b) of button cell tested samples employed for the process characterization experiments.

5.1.1. Fuel comparison

Figure 5.2 reports the comparison between the DRT plots obtained for the three different fuel compositions: H₂ – H₂O, CO – CO₂, and syngas, at T = 700 °C and T = 650 °C.

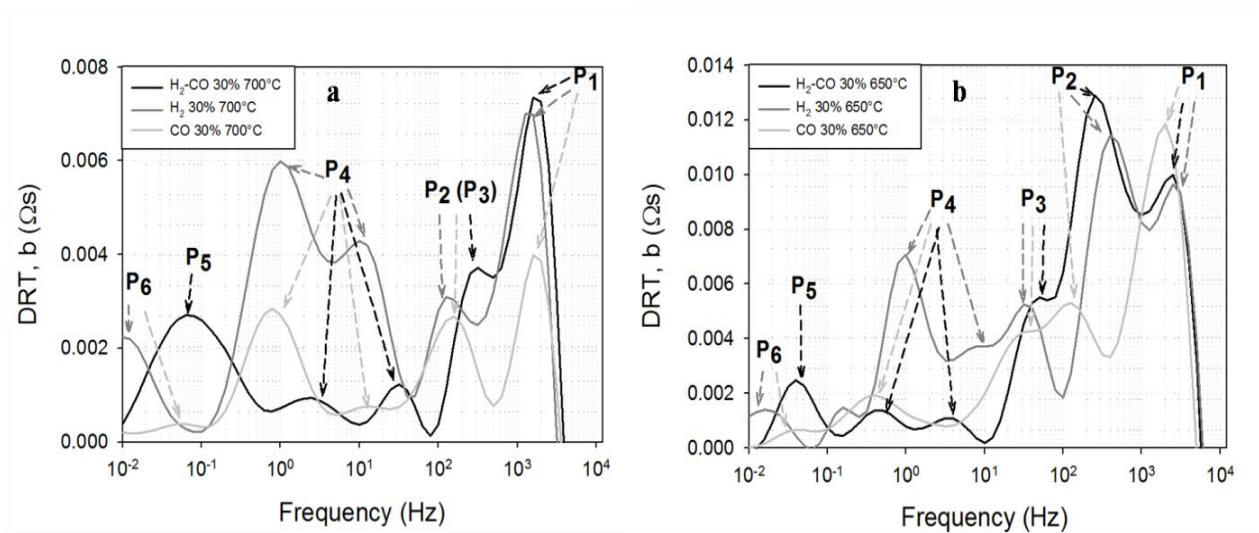


Figure 5.2. DRT plots with different types of fuel at (a) T = 700°C and (b) T = 650°C.

In all cases, up to six different processes can be recognized. Depending on the fuel type and on the operating temperature, the characteristic frequency of each process may result slightly shifted. This phenomenon can be related to the effect of a different surface chemistry experienced by the anodic processes, as demonstrated in the work of Zhu et al.⁸¹: surface adsorbed species introduce a storage capacity that manifests itself as a shift of the characteristic frequency of those processes that are more influenced by surface chemistry (i.e. gas diffusion).

When the characteristic frequency of two adjacent processes differs of less than a decade in frequency, two peaks may overlap: it is the case of process P₃, which is clearly evident in the plots obtained at T = 650°C (Figure 5.2.b), but appears convoluted with the process P₂ in the plots at 700°C (Figure 5.2.a). Furthermore, the process P₄ always appears as a principal peak falling at its characteristic frequency (c.a 1 Hz), followed by a satellite peak at higher frequency (c.a. 10 Hz): the nature of the process represented by this particular feature will be established hereafter, along with the nature of the phenomena behind the other DRT peaks.

5.1.2. H₂/H₂O operation

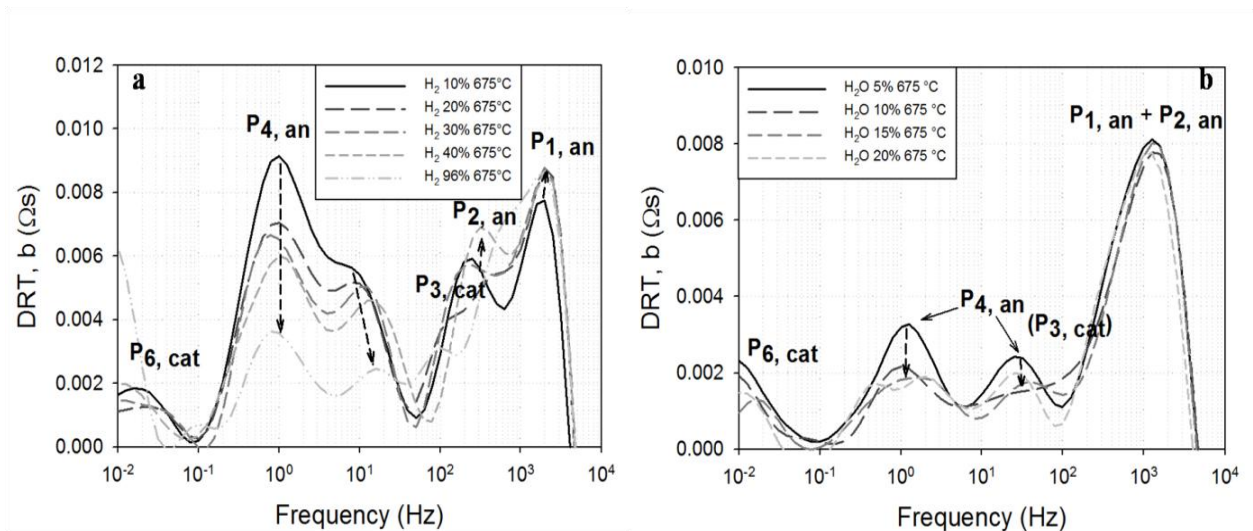


Figure 5.3. DRT plots for (a) hydrogen variation and (b) water variation at T = 675°C.

Considering the two high frequency processes P₁ and P₂ appearing as a single contribution in the case of water variation, it can be appreciated how both these contributions are barely affected by a change in the anodic composition, but are indeed influenced by a temperature variation (Figure

5.4). These behaviors suggest a fast, thermally activated anodic process underlying in these peaks; thus, they can be ascribed to the charge transfer mechanism related to the hydrogen electrochemical oxidation occurring at the anode functional layer (AFL), together with the oxygen ion transport within the YSZ lattice. This attribution perfectly agrees with other works carried out on YSZ based anode supported SOFCs reported in literature from other authors^{64, 65, 82,83}.

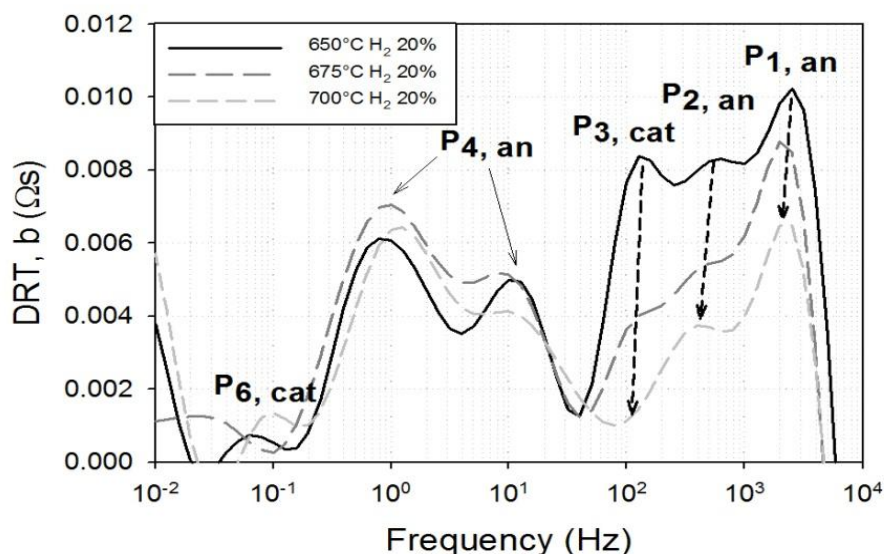


Figure 5.4. DRT plots for the temperature variation at $H_2 = 20\%$.

Peak P_3 appears unaffected from a modification of the anodic molar fractions, but shows an exponential dependency from the operating temperature, that allows associating this feature to the charge transfer mechanism related to the oxygen reduction within the cathode layer^{58, 64, 68}.

In the low frequency region, two distinct features, one falling at c.a. 1 Hz and the other one around 10 Hz have a very similar behaviour when the anodic composition and the operating temperature are altered: they both show a prominent dependency to the anodic molar fraction variations and they are only marginally influenced by the increase of the temperature. In the EIS field, mass transport phenomena are frequently represented by a distributed circuit element, known as the Warburg element⁸⁴. The DRT function calculated for a Warburg impedance response results in a principal peak, falling at the characteristic frequency of the process, followed by a set of satellite peaks, with decreasing intensity, at higher frequency. Therefore, it is

reasonable to ascribe these two peaks to a single mass transport phenomenon (P_4) associated with the diffusion of gas species through the porosity of the anode supporting layer of the cell^{64, 65, 81, 83}. It is worth noting that the characteristic frequencies of the aforementioned anodic processes observed in this work are shifted to lower frequencies of half of a decade compared to what reported by Leonide et al. on another type of cell^{64, 66, 81}. Due to this frequency shift, while in literature it is reported that the charge transfer process at the cathode overlaps with the anodic gas diffusion process, for all the cells tested in this work, the peak related to the charge transfer phenomenon at the cathode side is always comprised between the peak P_2 and the satellite peak of the process P_4 . Nevertheless, the peak P_3 is observed in a frequency range between 20 Hz and 100 Hz, in accordance with what observed by other authors for LSCF cathodes^{64, 68}. Finally, the process P_6 falling at very low frequency is only slightly affected by the temperature, and does not change with a change in the anode composition: it can be hypothesized to be the contribution of the gas diffusion through the porosity of the cathode layer⁵⁸. These attributions, made on the basis of results obtained for $H_2 - H_2O$ operation, will be further confirmed from the analysis of the DRT spectra for the other two types of fuel studied.

5.1.3. CO/CO₂ operation

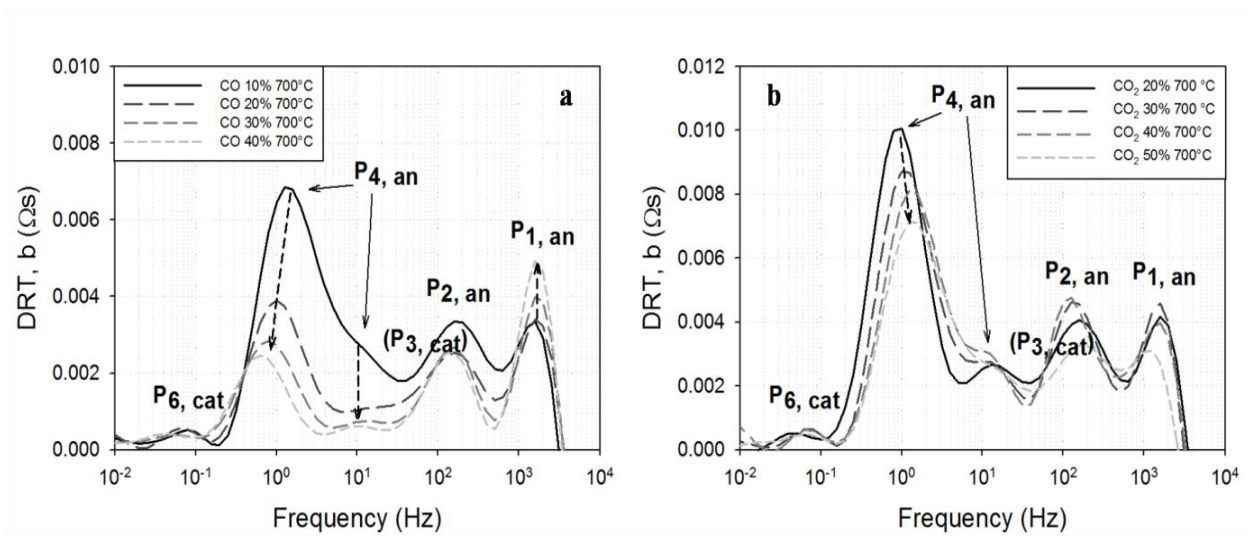


Figure 5.5. DRT plots for (a) carbon monoxide variation and (b) carbon dioxide variation at $T = 700^\circ\text{C}$.

Figure 5.5. reports the DRT plots obtained from the cell fed with CO – CO₂ mixtures.

As for the $H_2 - H_2O$ fuel, the high frequency processes P_1 and P_2 show little modification with the fuel composition, and an important dependency with the operating temperature, leading to the same conclusion that these peaks represent the charge transfer phenomenon at the AFL related to the oxidation of CO to CO_2 coupled with the ionic transport within the YSZ lattice. Interestingly, while the characteristic frequency of the P_1 process results nearly the same of that observed for this process in the $H_2 - H_2O$ mixture, the process P_2 shifts toward lower frequency, covering completely the cathodic process P_3 . This evidence suggests that, compared to the process P_1 , the process P_2 is more influenced by the molecular proprieties of the fuel species; since the ionic transport within the YSZ lattice should be, at least in theory, not influenced by the fuel proprieties, it can be hypothesized that P_1 is related to the ionic transport phenomenon, while the process P_2 is most likely ascribable to the charge transfer process in the oxidation reaction. Sonn et al. reported a DRT analysis carried out on technical Ni-YSZ anodes (half cell). They successfully separated the two contributions in the DRT plots related to the electrochemical oxidation of H_2 , ascribing the highest frequency process to the ionic transport within the YSZ matrix, and the second one at a lower frequency to the charge transfer mechanism involved in the electrochemical oxidation of H_2 ⁸³. Nevertheless, in our case, further and more specific investigations are needed to confirm this hypothesis, since both processes are deeply correlated, and sometimes convoluted with each other.

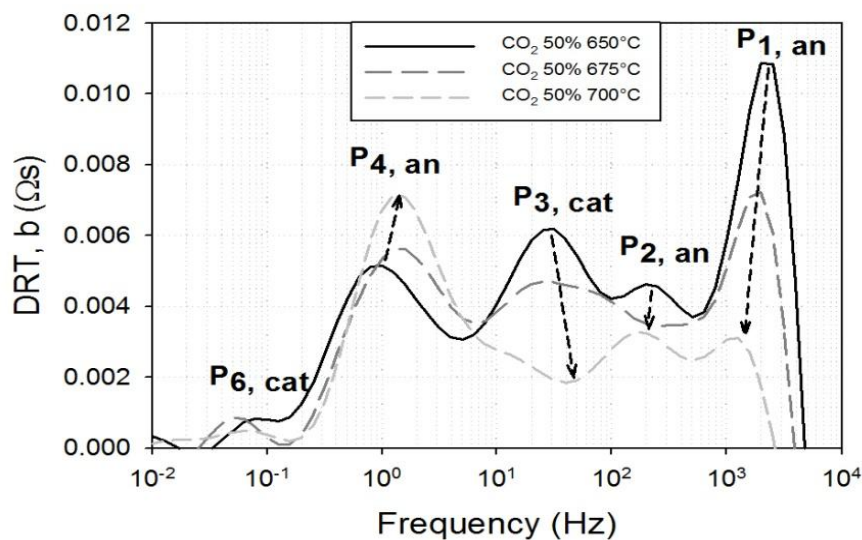


Figure 5.6. DRT plots for the temperature variation at $CO_2 = 50\%$.

Process P_4 confirms its pronounced dependency on the anodic composition, thus validating its attribution to the diffusion of the gas species through the anode porosity. Compared with the $H_2 - H_2O$ case, a more pronounced shift in the characteristic frequency of this process occurs when CO (or CO_2) molar fraction is increased, as a consequence of the influence of surface phenomena, that are, in turn, dependent on the nature of the gas species. An analogous phenomenon has also been reported in the work of Zhu et al., where the effect of the storage capacity arising from surface chemistry equilibriums on the characteristic frequency of the anodic processes were investigated by a synergic approach involving DRT methodology and the computational modeling of the EIS response of a SOFC, applied to different fuel compositions⁸¹. As the process P_6 is unaltered by a fuel modification, and being a low frequency process, the attribution of this feature to the diffusion of gas species within the cathode structure holds.

5.1.4. Syngas operation

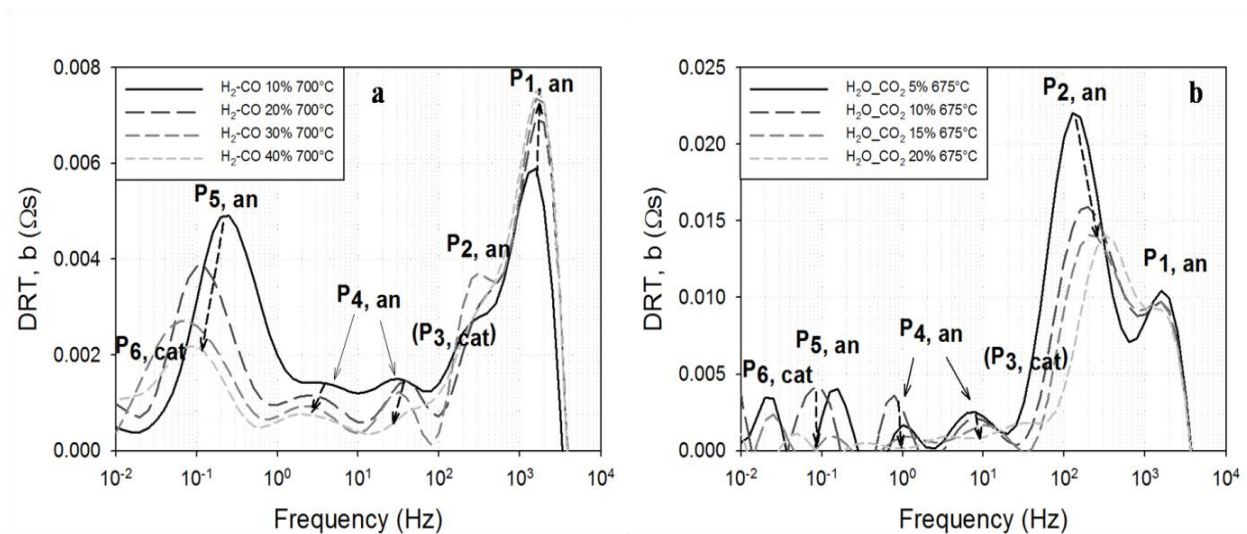


Figure 5.7. DRT plots for (a) H_2 and CO variation at $T = 700^\circ C$ and (b) H_2O and CO_2 variation at $T = 675^\circ C$.

Figures 5.7.a and 5.7.b report the DRT plots obtained varying the syngas composition at the anode side for a fixed temperature, while Figure 5.8 depicts the DRT functions coming from a temperature variation at a fixed gas composition.

The high frequency processes P_1 , P_2 and P_3 (when visible) confirm their previous attribution to the anodic ionic transport and charge transfer mechanisms (P_1 and P_2) and to the charge transfer process at the cathode side (P_3). Furthermore, the characteristic frequency of the process P_2 is again influenced by fuel type and composition, as well depicted in Figure 5.7.b. In the case of an $H_2O - CO_2$ variation, a noteworthy dependency of the peak P_2 intensity can also be observed, which is typical for mass transport processes: it is reported in literature that the two aforementioned anodic processes (P_1 and P_2) may experiment a mass transport limitation arising from an insufficient AFL porosity. However, this contribution is frequently negligible for AFL layers thinner than $8 \mu m$, and becomes unimportant during the first 100 hours of cell operation, due to the development of an open porosity in the AFL^{76 85}.

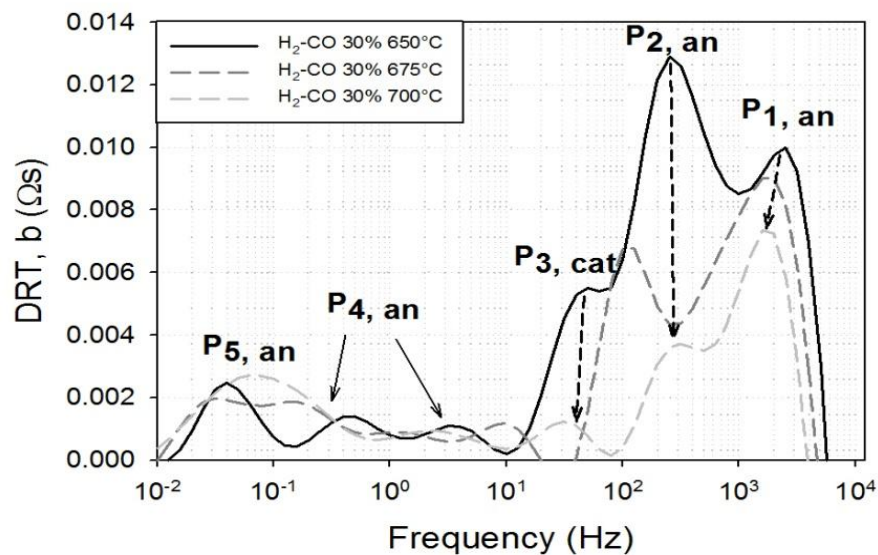


Fig. 5.8. DRT plots the temperature variation at $H_2 - CO = 30\%$.

Along with the low frequency anodic process P_4 , another feature, namely P_5 , appears only for syngas operation, with a characteristic frequency close to 10^{-1} Hz. Its presence is clearly evident when the DRT functions obtained for different fuels are compared (Figure 5.2 Section 5.1.1. Fuel comparison). In Figure 5.2.a (and to a lesser extent in Figure 5.2.b) a prominent dependency with the syngas composition of this process can be appreciated. Moreover, a reduction in the operating temperature does not seem to have a clear effect on the peak intensity. A. Kromp et al.^{66, 86} investigated the DRT response of their standard anode supported SOFC fed with different

syngas compositions. They identified a peak, ranging between 10^{-1} and 10^0 Hz, that had never been observed from previous DRT analyses carried out on the same kind of cell with hydrogen fuel. They observed a power law dependency of this process to the gas composition, but it did not show a thermally activated behavior. Being also a low frequency process, they ascribed this novel DRT feature to the occurrence of the Water Gas Shift (WGS) reaction, coupled with the gas diffusion through the porous anode. As explained by the authors, the external EIS stimulus induces the dynamic oxidation of H_2 , even in OCV conditions, thus affecting the equilibrium of the WGS reaction. In analogy with what is reported in literature, in this work the peak P_5 is then attributed to the WGS equilibrium coupled with a gas phase transport phenomenon. Also in the case of syngas operation, the identification of the processes reported in this work is in good agreement with the results obtained from other researchers^{66, 79, 86}.

5.1.5 Oxygen variation

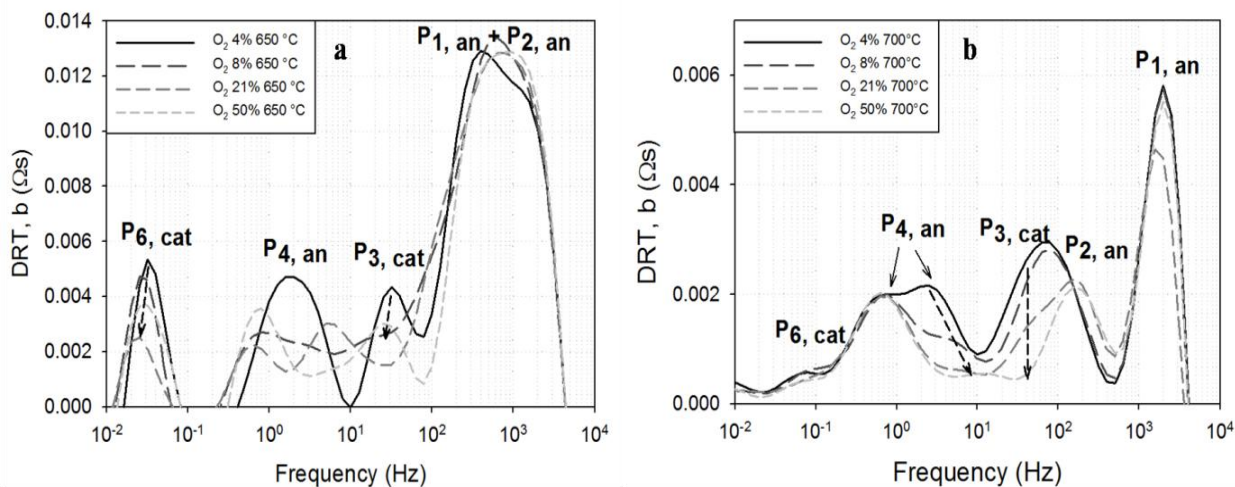


Figure 5.9. DRT plots for the oxygen variation with (a) H_2/H_2O at $T = 650^\circ C$ and (b) with CO/CO_2 variations at $T = 700^\circ C$.

Figure 5.9. reports the effect of an oxygen variation at the cathode side on the DRT response of a button cell sample fed with humidified hydrogen (Figure 5.9.a) or CO/CO_2 mixtures (Figure 5.9.b).

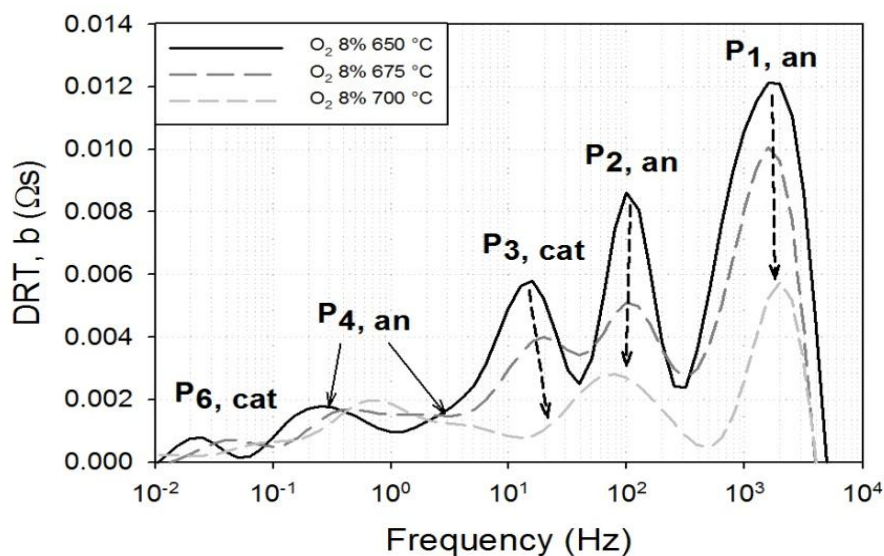


Figure 5.10. DRT plots for the temperature variation with O_2 8%.

Due to the overlapping of the cathodic process P_3 with the anodic process P_2 it is hard to evaluate the effect of the oxygen variation on this process. Nevertheless, a reduction in its intensity is still noticeable, especially from the plot 5.9.b. Moreover, from the Figure 5.9.a, an important reduction of the intensity of the peak P_6 supports the previous attribution of this process to the diffusion process at the cathode side. It is reported in literature^{64,76} that significant and coherent variations of the cathodic processes are achievable only for very low oxygen content in the cathode stream ($< 2\%$); due to the limitations related to the bottom scales of the mass flow meters employed for the cathode stream, such a low oxygen content was not achievable. Nevertheless, the temperature variation reported in Figure 5.10 still confirms that the process P_3 possesses a thermal activation behavior.

5.1.6. Current load variation

When current flows through the cell, it is expected, from the expression of the Butler – Volmer equation, that the peaks related to the charge transfer processes (both at the anode and cathode side) show a significant variation in their intensity; moreover, the generation of current is related to the oxidation of the fuel at the anode side, which causes a reduction in the fuel content and an

increase in the product content at the anode, thus affecting the processes associated to the gas transport phenomena.

From EIS measurements carried out at different current densities, when the operating temperature and the inlet gas compositions are kept constant, it is possible to estimate the values of the forward reaction symmetric factors α_{anode} and $\alpha_{cathode}$, evaluating the dependency of the charge transfer resistances extrapolated from the EIS spectra with respect to a variation of the current density. Unfortunately, in all the measurements carried out under constant current in this work, a very poor resolution of the experimental EIS spectra was obtained, as also previously demonstrated with the KK-test in Chapter 3. When the experimental points result largely affected by noise, the incoherent signals produce scattered points in the EIS spectra, that in turn greatly affect the DRT response, which loses its effectiveness. For most of the frequencies investigated, when current was drawn from the cell, the DRT plots resulted in confused signals, as depicted in Figure 5.11. below. Even though the high frequency peaks related to the anode charge transfer mechanism appear well defined, the rest of the signals appear confused, and this hindered the reliability of the results obtainable with the CNLS-ECM fitting procedure described in Chapter 3. For these reasons, the DRT plots obtained under current are shown only to qualitatively assess the effect of a current variation on the charge transfer process at the anode side, and the reader is referred to the results achieved from other authors in literature^{82, 87} for the calculation of the forward reaction symmetric factors α_{anode} and $\alpha_{cathode}$ starting from the dependency of the charge transfer resistances with the current density.

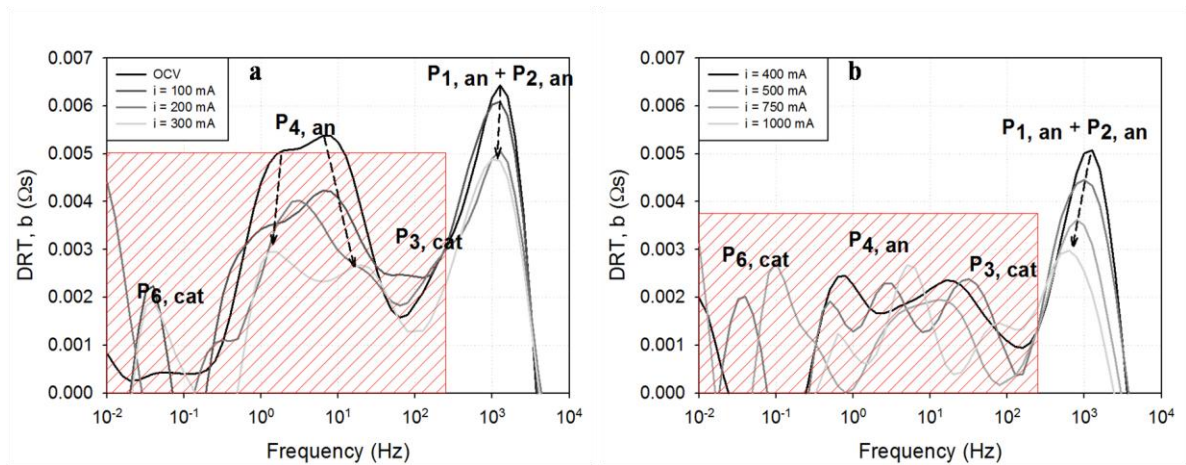


Fig. 5.11. DRT plots for the current variation with H_2 40% at $T = 700$ °C. a) From OCV to 300 mA; b) from 400 mA to 1000 mA.

Observing the two plots reported in Figure 5.11.a and 5.11.b., an increase in the current drawn from the cell correspond to a decrease in the intensity, and a slight shift towards lower frequency of the high frequency process related to charge transfer mechanism at the anode side reflecting the behavior suggested from the Butler – Volmer equation. Except for an initial reduction of the intensity of the process P_4 , the signals appearing below 300 Hz (masked by a red box in the plots) were too incoherent to allow further analysis.

5.1.7. Resume of the identified processes

From the investigation reported in this chapter, up to six different processes were identified from the DRT plots. Depending on the fuel typology and operating temperature, some processes may overlap with each other or, as for the case of the process P_5 , are peculiar for a precise operating condition.

Nevertheless, a brief summary of the results of the process identification campaign is addressed hereafter.

The high frequency processes P_1 and P_2 show a prominent dependency on the operating temperature; furthermore, the process P_2 is also sensitive to a variation of the fuel composition. Together with their high characteristic frequencies, they have been both ascribed to the

electrochemical oxidation of the fuel occurring at the anode side. In particular, the process P_1 , is related to the transport of O^{2-} ions within the YSZ matrix of the anode functional layer. The process P_2 is in turn identified with the charge transfer mechanism of the electrochemical oxidation of the fuel occurring within the anode functional layer, in the three phase boundary (TPB) region.

Even though the process P_3 resulted often convoluted with the anodic process P_2 , its dependency with the operating temperature suggests a thermal activation behavior; being unaffected by anodic fuel type and composition, and slightly influenced by the O_2 content in the oxidant stream, it has been ascribed to the charge transfer mechanism for the reduction of O_2 to O^{2-} at the cathode side.

The particular shape of the DRT feature related to the process P_4 , consisting of a principal peak at the characteristic frequency followed by a smaller feature at higher frequency, is the typical response of a Warburg element in the DRT plots. The evident dependency on the composition of the fuel gas and the relatively low or null sensibility to a temperature variation suggest that this process is associated to a mass transport phenomenon, or rather to the gas diffusion through the open porosity of the anode substrate.

The process P_5 appears only when the sample is fed with a syngas mixture. It is clearly affected by a change in the molar fractions of the fuel, and barely influenced by a temperature variation: it has been thus attributed to the water gas shift reaction (WGS).

Finally, the process P_6 in the lowest frequency region can be associated to the diffusion of the cathodic gas in the MIEC porous structure. Even if the quality of the EIS measurements in this region is lower than in the high frequency region, especially when H_2O is present in the fuel stream, it can still be appreciated how this feature is dependent on the oxygen partial pressure in the cathode whilst the temperature has a minor impact. The small intensity of these contributions can be explained by the slimness of the cathode layer of the tested anode-supported cells (ASC).

5.2. Estimation of operating parameters

As explained in Chapter 3, from the synergic approach of DRT methodology coupled with a CNLS fitting of the experimental EIS spectra with an ECM, it is possible to extrapolate the values of the resistances related to the different processes identified in the DRT plots. The trends of these resistances with respect to the varying of a single operating condition (molar fractions,

cell temperature) are in turn related to the fundamental equations governing the mechanisms of an SOFC, such as the Butler – Volmer equation or Fick’s laws for gas diffusion.

By means of this experimental approach, physical quantities such as activation energies and reaction orders can be extracted directly from EIS measurements coming from the SOFC samples in-operando conditions.

The following Sections report the calculations performed to obtain these parameters, starting from the dependencies of the single process resistances obtained from the CNLS fitting of EIS measurements, for each condition studied in this work.

Recalling all the considerations proposed for the DRT spectra analysis, about the number and the nature of the identified processes, the ECM reported in Figure 5.12. below was employed for the fitting of the experimental spectra.

The electrical resistance of the cell encompasses the electronic and ionic resistances of all the layers composing the SOFC. R_0 is the Ohmic resistance of the cell, which can be regarded as a sum of the different electronic and ionic resistances within the cell connected in series. However, the major contribution to R_0 is given by the conductivity of the electrolyte layer, being several orders of magnitude smaller than that of the electrodes.

As explained in Chapter 3, an RC element is generally employed to model the EIS response of a charge transfer occurring at an interface. Furthermore, when the process takes place in non-ideal conditions (distributed surface reactivity, surface inhomogeneity, roughness or fractal geometry), a constant phase element (CPE) is generally preferred over the capacitor for fitting purposes as it can represent the deviation from a pure capacitance of the EIS response by means of an exponential factor, n , with $0 \leq n \leq 1$ ⁷³. For these reasons, the anodic processes P_1 and P_2 , and the cathodic process P_3 are represented in the ECM with a parallel of a resistance R_i and a constant phase element CPE_i .

The diffusion of gaseous species in a solid porous structure is generally modelled by a Finite-length Warburg (FLW) diffusion impedance⁷⁵. Thus, in the ECM W_{4_anode} and $W_{6_cathode}$ are the Finite Length Warburg elements representing the gas diffusion through the anode and cathode porous matrix, respectively (processes P_4 and P_6). It is worth underlining that in most cases, especially when normal air or O_2 enriched air is fed to the cathode side, the contribution of the process P_6 is generally small or overlapped by other contributions: in these cases, the impedance of the process P_6 has been neglected.

For what concerns the process related to the water gas shift reaction (P_5), occurring only when the cell is operated with a syngas fuel, it is reported in other studies that the gas conversion nature of this process is predominant as compared to the gas diffusion behaviour^{66, 79}: for fitting purposes, better results are then obtained with a generic R-CPE parallel rather than a distributed element, and thus, in the ECM employed in these analyses, such a circuit element has been adopted to model the response of the process P_5 .

Finally, an inductive element L_0 is present to consider the high frequency inductive impedance introduced by instrumental electric artefacts.

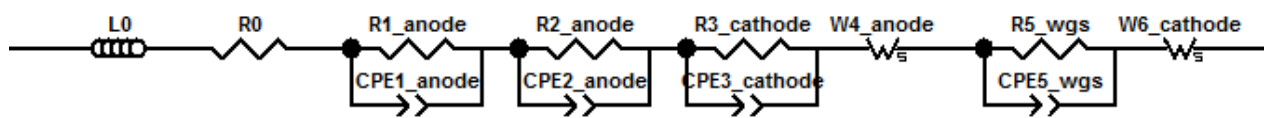


Figure 5.12. Complete ECM employed for the analysis of the EIS spectra. The R-CPE parallel for the water gas shift reaction was employed only for the spectra obtained with a syngas fuel.

The ECM model in Figure 5.12 has the advantage to be generated directly from the information about the number and the nature of the processes obtained from the DRT methodology, that are in turn based on the experimental response of the cell to different operating conditions. This means that this ECM model is supported by experimental evidences, without any *a priori* assumptions.

5.2.1. H_2/H_2O operation

Reaction orders

The following dissertation concerns the anode processes of a button cell sample fed with humidified hydrogen. An analogous methodology can be applied also to the processes occurring at the cathode side: however, a better estimation of the cathodic processes P_3 was obtained in the case of CO/CO_2 fuel, and it will be presented in Section 5.2.2.

The Butler - Volmer equation (described in Chapter 2), can be redefined as an infinite sum of terms (known as Taylor series) describing the relationship between current and overpotential as follows:

$$i = i_0 \left[\frac{n_e F \eta_{act}}{RT} + \frac{(2\alpha-1)}{2} \left(\frac{n_e F \eta_{act}}{RT} \right)^2 + \frac{(3\alpha-3\alpha^2-1)}{6} \left(\frac{n_e F \eta_{act}}{RT} \right)^3 + \dots \right] \quad (5.1)$$

For very small overpotentials a first-order approximation can be made with a negligible error, producing a linear relationship between the activation overpotential and the current density. As the EIS measurements have been carried out under OCV conditions with a small excitation signal ($\Delta V = 10$ mV), the abovementioned condition is valid and Equation 5.1 becomes:

$$i \approx i_0 \frac{n_e F \eta_{act}}{RT} \quad (5.2)$$

Expressing the anode's local exchange transfer current density with respect to the molar fractions of H_2 and H_2O in the bulk of the anode (Equation 2.11), considering that two electrons take part in the electrochemical reaction per mole of H_2 reacted ($n_e = 2$) and differentiating the anode activation overpotential with respect to the current density in Equation 5.2, the resistance to the charge transfer mechanism can be written as follows:

$$R_{ct,anode} = \frac{RT}{2Fi_{0,anode}^{pre} (x_{H_2,bulk})^{\gamma_{H_2}} (x_{H_2O,bulk})^{\gamma_{H_2O}} \exp\left(\frac{E_{act,anode}}{RT}\right)} \quad (5.3)$$

By applying logarithms to both sides, Eq. (x.x) becomes:

$$\log(R_{ct,anode}) = \log\left(\frac{RT}{2Fi_{0,anode}^{pre} (x_{H_2,bulk})^{\gamma_{H_2}} (x_{H_2O,bulk})^{\gamma_{H_2O}} \exp\left(\frac{E_{act,anode}}{RT}\right)}\right) - \gamma_{H_2} \cdot \log(x_{H_2,bulk}) \quad (5.4)$$

Or:

$$\log(R_{ct,anode}) = \log\left(\frac{RT}{2Fi_{0,anode}^{pre} (x_{H_2,bulk})^{\gamma_{H_2}} \exp\left(\frac{E_{act,anode}}{RT}\right)}\right) - \gamma_{H_2O} \cdot \log(x_{H_2O,bulk}) \quad (5.5)$$

From the CNLS fitting of the EIS measurements obtained varying the molar fraction of H₂ (or the molar fraction of H₂O), $R_{ct,anode}$ can be obtained as the sum of $R_{1,anode}$ and $R_{2,anode}$, since the processes P₁ and P₂ are both related to the oxidation reaction of the fuel, as previously explained.

$$R_{ct,anode} = R_{1,anode} + R_{2,anode} \quad (5.6)$$

If $R_{ct,anode}$ is plotted against x_{H_2} in a log-log plot, with x_{H_2O} kept constant (or against x_{H_2O} with x_{H_2} constant), the reaction orders γ_{H_2} or γ_{H_2O} can be obtained from the slope of the regression line correlating the experimental values of $R_{ct,anode}$ with the variation of the respective molar fractions.

Figure 5.13. and 5.14 depict the log-log- plots of $R_{ct,anode}$ vs x_{H_2} and x_{H_2O} respectively

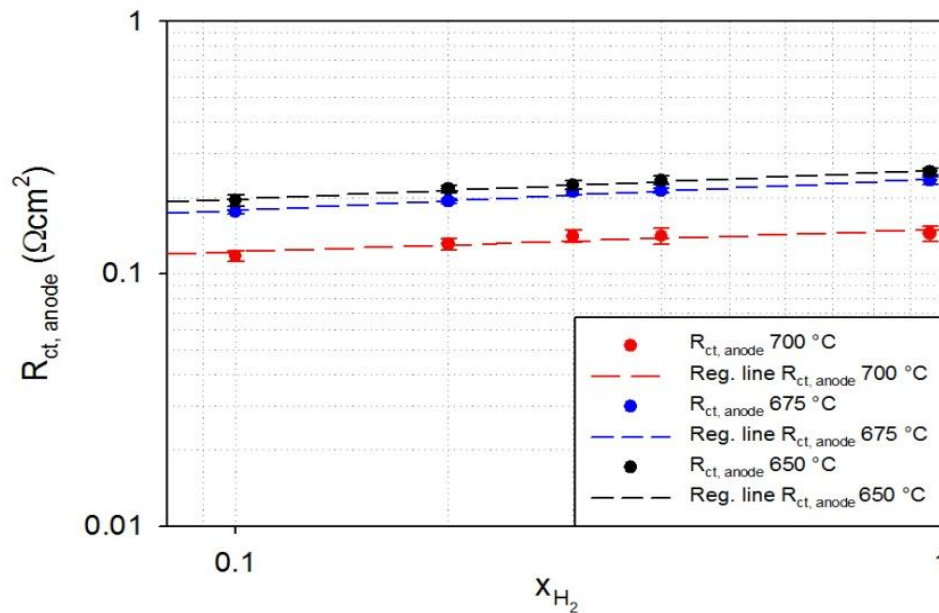


Figure 5.13. Charge transfer resistance in the anode as a function of the hydrogen molar fraction at 700, 675 and 650°C.

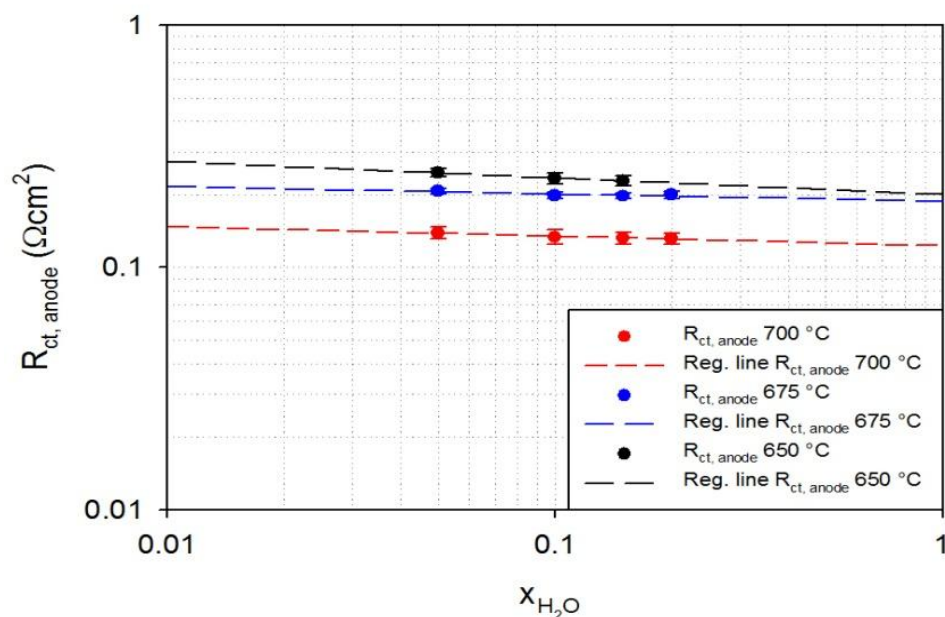


Figure 5.14. Charge transfer resistance in the anode as a function of the water molar fraction at 700, 675 and 650°C.

The mean values obtained for the reaction orders are $\gamma_{H_2} = -0.11$ and $\gamma_{H_2O} = 0.042$. While for the reaction order of H_2 the value obtained in this work agrees with what reported in literature^{64, 65, 66}, a very small value of the reaction order of H_2O was obtained, compared to what was found by other authors ($\gamma_{H_2O} = 0.33$ ^{76, 82}). However, observing the DRT plots for water variation reported in Section 5.1.2 (Figure 5.3.b), the intensity of the high frequency peaks related to the charge transfer mechanism results barely affected from a change in the water content; hence, the small value of γ_{H_2O} obtained from the CNLS/ECM fitting procedure coherently reflects the experimental observations.

Activation energy and pre-exponential factor

The activation energy associated to charge transfer mechanisms in the anode and the pre-exponential factor can be estimated employing Equation 5.3, by normalizing both sides as a function of temperature and applying natural logarithms:

$$\ln\left(\frac{R_{ct,anode}}{T}\right) = \ln\left(\frac{R}{2Fi_{0,anode}^{pre} (x_{H_2,bulk})^{y_{H_2}} (x_{H_2O,bulk})^{y_{H_2O}}}\right) + \frac{E_{act,anode}}{RT} \quad (5.7)$$

The experimental data obtained from the tests carried out under diverse molar fractions of hydrogen and steam at different temperatures can be plotted in the following way: $1000/T$ vs. $\ln\left(\frac{R_{ct,anode}}{T}\right)$. In this case, the regression line can be expressed in the following terms:

$$\ln\left(\frac{R_{ct,anode}}{T}\right)\Big|_{fit} = a_0 + a_1 \frac{1000}{T} \quad (5.8)$$

where a_0 and a_1 are constants (intercept and gradient respectively).

For a temperature variation, the molar fractions are kept constants. It can be easily demonstrated, by simply comparing Equation 5.7 with Equation 5.8, that the activation energy is related to the slope of the linear regression, while the pre-exponential factor can be calculated from its intercept by means of Equations 5.9. and 5.10. below:

$$a_1 = \frac{E_{act,anode}}{1000 \cdot R} \quad (5.9)$$

$$a_0 = \ln\left(\frac{R}{2Fi_{0,anode}^{pre} (x_{H_2,bulk})^{y_{H_2}} (x_{H_2O,bulk})^{y_{H_2O}}}\right) \quad (5.10)$$

Figure 5.15. depicts the trend of the anode charge transfer resistance with respect to the operating temperature, at different fixed hydrogen molar fractions.

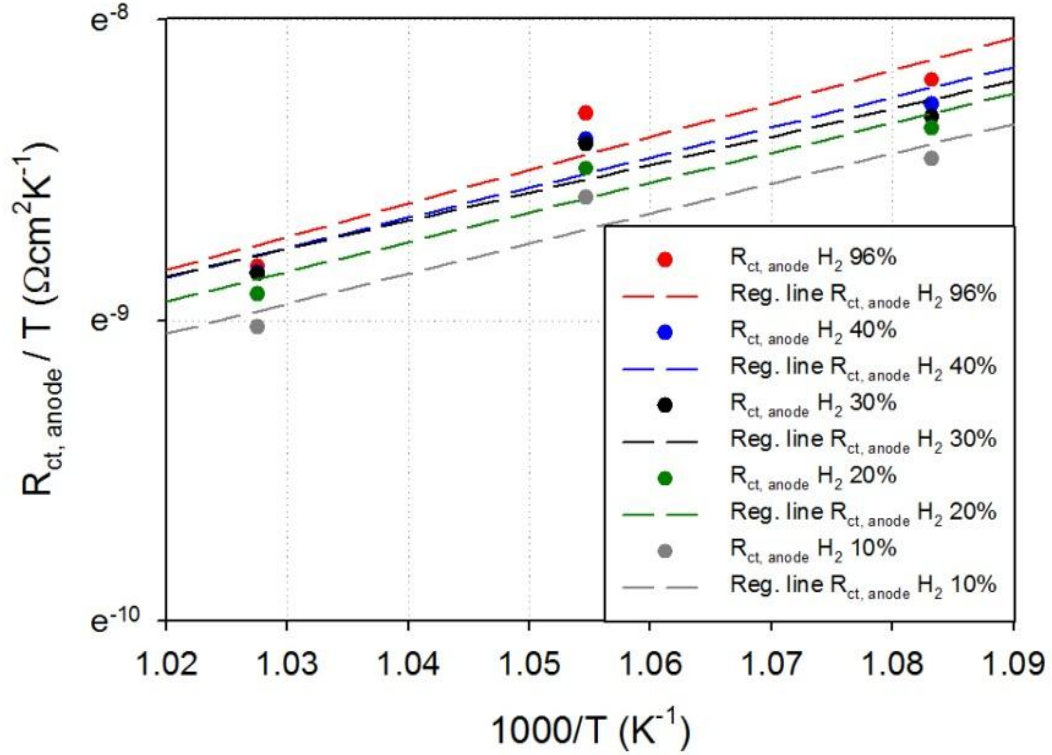


Figure 5.15. Charge transfer resistance in the anode as a function of the temperature for different hydrogen molar fractions.

From calculations performed as explained above, a mean value for the activation energy of the charge transfer mechanism for the hydrogen oxidation reaction of $E_{act,anode} = 83.43 \text{ kJ} \cdot \text{mol}^{-1}$ is obtained. Other authors employing the same DRT-CNLS fitting approach to the response of technical Ni-8YSZ anodes on a standard SOFC cell reports a value of $E_{act,anode} = 105 \text{ kJ} \cdot \text{mol}^{-1}$ ^{76, 82}; the value obtained for the IT-SOFC samples tested in this work results still consistent with literature data.

Considering the pre-exponential factor, a mean value of $i_{0,anode}^{pre} = 4.515 \cdot 10^6 \text{ A} \cdot \text{cm}^{-2}$ is found; literature data shows that the exchange transfer current density pre-exponential factor can vary up to several orders of magnitude, from 10^4 to $10^8 \text{ A} \cdot \text{cm}^{-2}$ ^{88, 89}. Other authors employing a similar DRT-CNLS fitting approach to the experimental data, report a value of $i_{0,anode}^{pre} = 1.8 \cdot 10^5 \text{ A} \cdot \text{cm}^{-2}$, calculated at $T = 700 \text{ }^\circ\text{C}$ ⁸².

Diffusion coefficients

Starting from the expression of the diffusion polarization losses presented in Chapter 2, and analyzing the dependency of the resistance related to the gas diffusion within the porous structure of the anode (and cathode) with respect to a variation of the molar fractions, from the DRT-CNLS fitting approach it is possible to estimate the values of the effective diffusion coefficients D_i^{eff} , that reflect the impact of structural parameters like the porosity and the tortuosity of the electrodes, as well as the effects of the Knudsen diffusion.

Recalling the concentration overpotential expression, based on the Nernst equation:

$$\eta_{conc,anode} = \frac{RT}{2F} \ln \left(\frac{p_{H_2O}^{TPB,anode} \cdot p_{H_2,anode}}{p_{H_2O,anode} \cdot p_{H_2,anode}^{TPB}} \right) \quad (5.11)$$

$$\eta_{conc,cathode} = \frac{RT}{4F} \ln \left(\frac{p_{O_2,cathode}}{p_{O_2,cathode}^{TPB}} \right) \quad (5.12)$$

The partial pressures of the gas species at the three phase boundary can be expressed as a function of the current density. The way in which they are expressed strongly depends on the model chosen to describe the mass transport phenomena. In the SOFC fields, the most renowned are the Fick, the Stephan-Maxwell and the dusty gas models⁹⁰.

The Fick model is the simplest one, and it is a good model for the description of mass transport phenomena of binary and ternary gas mixtures in a porous matrix. Since the tested sample was fed with a ternary mixture of H₂/H₂O balanced with N₂, Fick's model will be employed in this discussion.

For a binary gas mixture, by applying Fick's first law and considering that the amount of current generated in the TPB is governed by the rate of gas species diffusing into the porous anode, the following equation can be written:

$$\left. \frac{dx_i}{dz} \right|_{z=l_a} = - \frac{RT}{2FD_{i,B}^{eff} P} \cdot j \quad (5.13)$$

Where x_i is the molar fraction of the fuel specie, P is the operating pressure, j is the current density, l_a is the anode thickness and $D_{i,B}^{eff}$ is the effective diffusion coefficient of the species i in a binary gas system.

The effective diffusion coefficient generally depends on both the effective molecular diffusion and the effective Knudsen diffusion coefficients as follows:

$$D_i^{eff} = \left(\frac{1}{D_{i,j}^{eff}} + \frac{1}{D_{i,Knudsen}^{eff}} \right)^{-1} \quad (5.14)$$

while $D_{i,j}^{eff}$ and $D_{i,Knudsen}^{eff}$ depend in turn on the microstructure of the porous anode (porosity, tortuosity, particle size) and on the operating conditions (temperature and pressure).

Applying the Neuman boundary condition ($z = l_a$) and the Dirichlet boundary condition ($x_i|_{z=0} = x_{i,bulk}$) Equation 5.13. becomes:

$$x_i = x_{i,bulk} - \frac{RTl_a}{2FD_{i,B}^{eff}P} \cdot j \quad (5.15)$$

In the case of a ternary gas system, such as the $H_2/H_2O/N_2$ mixtures studied in this work, the previous equation becomes:

$$x_i = x_{i,bulk} - \frac{RTl_a}{2FD_{i,T}^{eff}P} \cdot j \quad (5.16)$$

Where $D_{i,T}^{eff}$ is the ternary effective diffusion coefficient, and it assumes the following form:

$$D_{i,T}^{eff} = \frac{1}{\left(\frac{1}{D_{i,Knudsen}^{eff}}\right) + \left(\frac{1}{D_{i,N_2}^{eff}}\right) + \left(\left(\frac{1}{D_{i,j}^{eff}}\right) - \left(\frac{1}{D_{i,N_2}^{eff}}\right)\right)(1-x_{N_2})} \quad (5.17)$$

Substituting the expressions of x_i into the expression of the anode concentration overpotential, it becomes, for binary systems:

$$\eta_{conc,B} = -\frac{RT}{2F} \ln \left\{ \frac{\left[x_{i,bulk} - \left(\frac{RT l_a}{2FD_{i,B}^{eff} P} \right) \cdot j \right] (1 - x_{i,bulk})}{x_{i,bulk} \left[1 + \left(\frac{RT l_a}{2FD_{i,B}^{eff} P} \right) \cdot j - x_{i,bulk} \right]} \right\} \quad (5.18)$$

And for ternary systems:

$$\eta_{conc,T} = -\frac{RT}{2F} \ln \left\{ \frac{\left[x_{i,bulk} - \left(\frac{RT l_a}{2FD_{i,T}^{eff} P} \right) \cdot j \right] (1 - x_{i,bulk} - x_{N_2,bulk})}{x_{i,bulk} \left[1 + \left(\frac{RT l_a}{2FD_{i,T}^{eff} P} \right) \cdot j - x_{i,bulk} - x_{N_2,bulk} \right]} \right\} \quad (5.19)$$

If the expressions of the concentration overpotential are differentiated with respect to the current density, and calculated in OCV conditions ($j = 0$) the following two expressions of the resistances related to the diffusion of gas species in the porous matrix of the anode arise:

$$R_{diff,anode,B,i} = \left(\frac{RT}{2F} \right)^2 \frac{l_{anode}}{P} \frac{1}{D_{i,B}^{eff}} \left(\frac{1}{1 - x_{i,bulk}} \right) \quad (5.20)$$

$$R_{diff,anode,T,i} = \left(\frac{RT}{2F} \right)^2 \frac{l_{anode}}{P} \frac{1}{D_{i,T}^{eff}} \left(\frac{1}{1 - x_{i,bulk} - x_{N_2,bulk}} \right) \quad (5.21)$$

Analogously, an expression for the resistances related to the diffusion of gas species in the porous matrix of the cathode can be written, considering that only binary mixtures are generally fed to the cathode (air):

$$R_{diff,cathode,B,i} = \left(\frac{RT}{4F} \right)^2 \frac{l_{anode}}{P} \frac{1}{D_{i,B}^{eff}} \left(\frac{1}{x_{i,bulk}} \right) \quad (5.22)$$

The values of $R_{diff,anode}$ and $R_{diff,cathode}$ correspond to the real part of the impedance related to the Warburg elements employed in the CNLS fitting of the experimental EIS spectra.

In Figure 5.16 and 5.17 below, the values of $R_{diff,anode}$ extracted from the CNLS fitting of the EIS spectra are reported as a function of the molar fraction of hydrogen and steam, respectively.

The dashed lines represent the results of the fitting of the experimental values with a model curve. For the variation of the hydrogen molar fractions, a modest value of r^2 was obtained from the fitting procedure ($r^2 = 0.7$), while in the case of water variation, a very high value of r^2 was achieved for each fitting attempt ($r^2 = 0.96$).

Considering the results coming from all the experimental data, a mean value for the ternary effective diffusion coefficients of $D_{H_2,T}^{eff} = 4.58 \cdot 10^{-5} m^2 s^{-1}$ and $D_{H_2O,T}^{eff} = 1.63 \cdot 10^{-4} m^2 s^{-1}$ were obtained, that are consistent with what was reported by other authors employing the same methodology^{64, 76}.

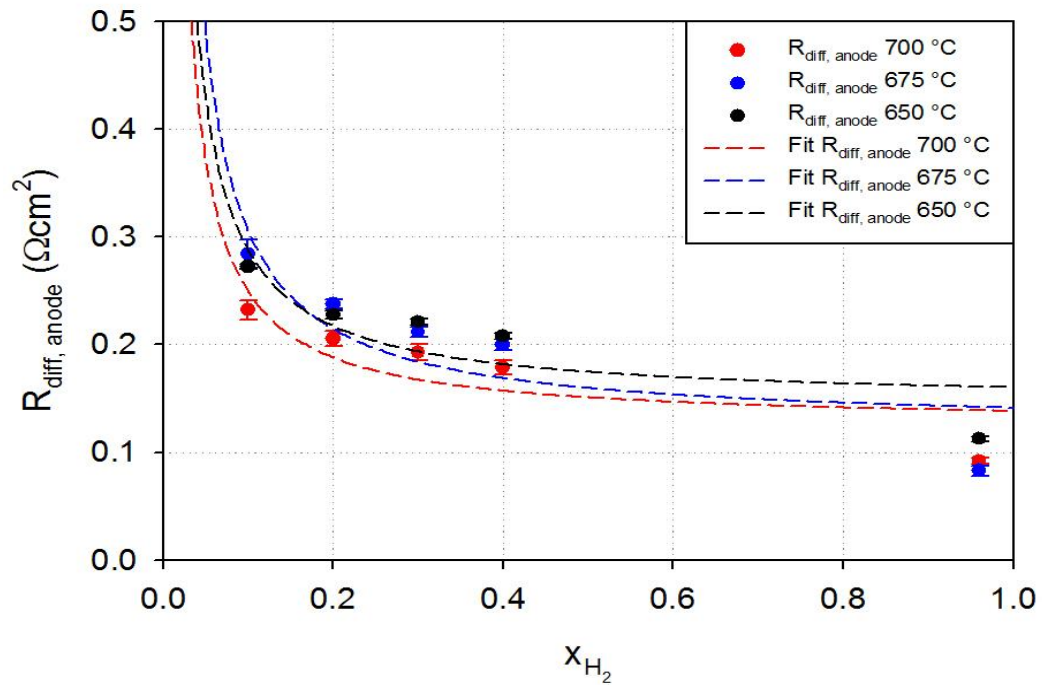


Figure 5.16. Gas diffusion resistance in the anode as a function of the hydrogen molar fraction, at 700 °C, 675 °C and 650 °C.

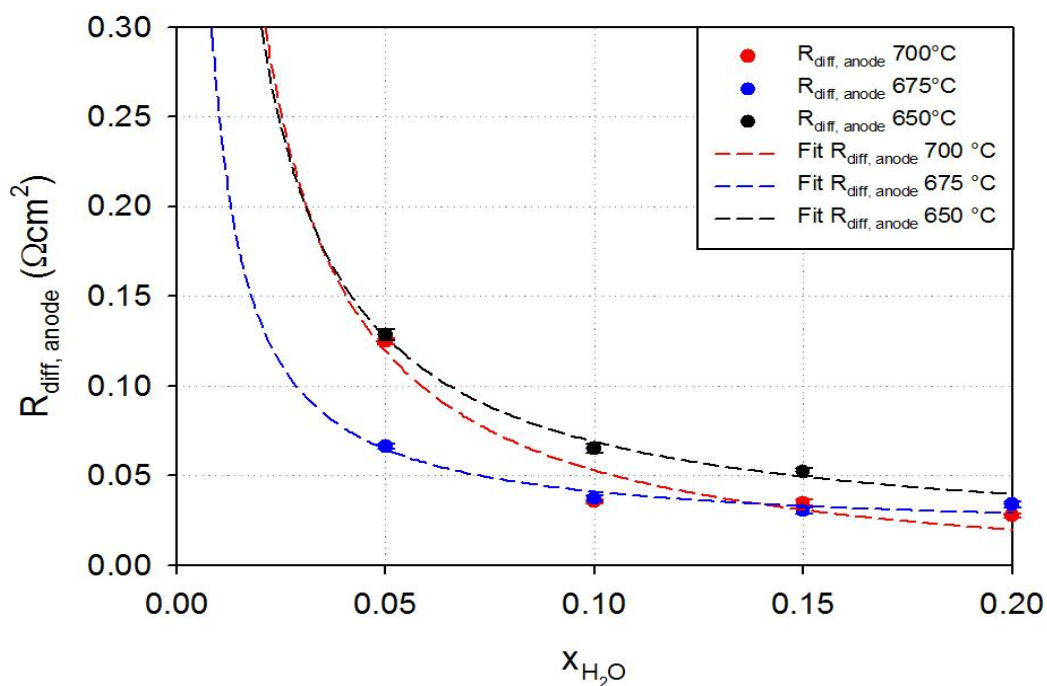


Figure 5.17. Gas diffusion resistance in the anode as a function of the water molar fraction, at 700 °C, 675 °C and 650 °C.

Regarding the effective diffusion coefficient at the cathode side, it was previously explained that the contribution of the diffusion of the gas species through the cathode porosity results extremely hard to be estimated, if the oxygen partial pressure is not reduced to very low values; unfortunately, as explained in Section 5.1.5. due to the limitations related to the bottom scales of the mass flow meters employed for the cathode stream, low oxygen content was not achievable.

Nevertheless an attempt to estimate a value for $D_{O_2, B}^{eff}$ was still performed; Figure 5.18. below reports the values of $R_{diff, cathode}$ resulting from the CNLS fitting for the oxygen variation at the cathode side.

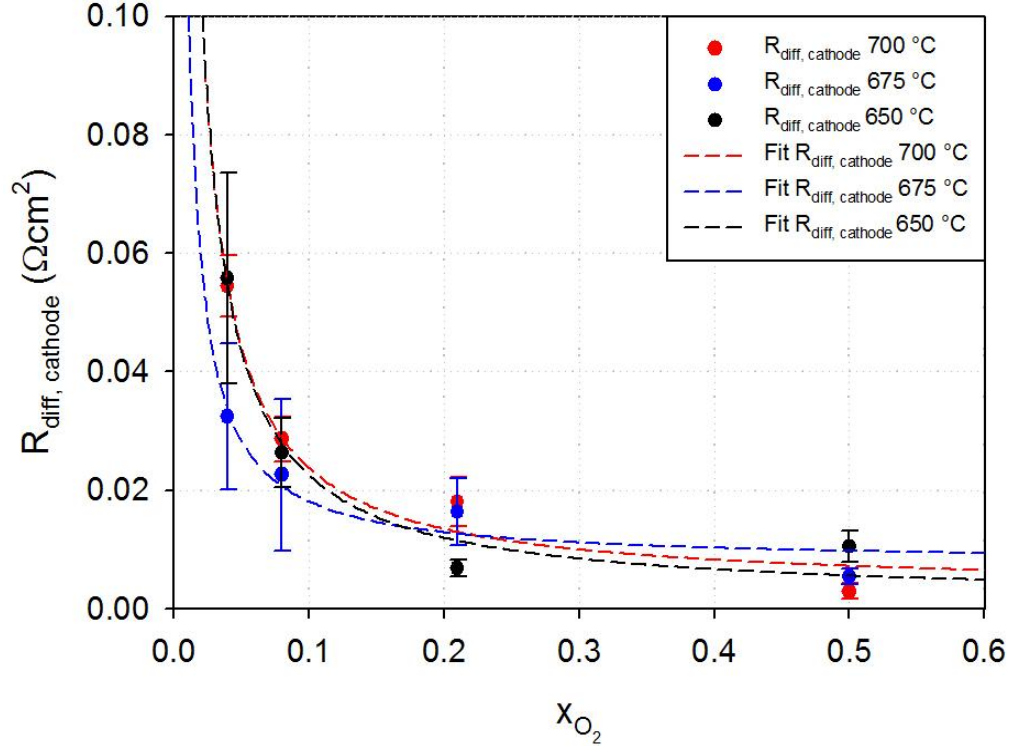


Figure 5.18. Gas diffusion resistance in the cathode as a function of the oxygen molar fraction at 700 °C, 675 °C and 650 °C.

Even though the errors associated with the estimation of the diffusion resistance obtained from the CNLS fitting with the ECM model results in some cases high, the fitting of the trend of the values with the model curve gave good results, with a mean value of $r^2 = 0.95$.

From the fitting, a mean value of $D_{O_2,B}^{eff} = 4.07 \cdot 10^{-6} m^2 s^{-1}$ was calculated, again in good agreement with what is stated in literature^{64,76}.

5.2.2. CO/CO₂ operation

In this Section, the estimation of the same parameters obtained for the H₂/H₂O case is addressed in the case of the CO/CO₂ fuel. Similar considerations and equations were employed also in this case; for the sake of simplicity, the mathematical derivations behind the extrapolation of these physical quantities will be omitted, being analogous to that presented in Section 5.2.1.

Nevertheless, as previously mentioned in Section 5.2.1, the process P₃, related to charge transfer processes at the cathode side, resulted more clearly estimable in this case, thus making it possible to calculate both the reaction order and the activation energy for the charge transfer mechanism associated with the electrochemical reduction of the oxygen at the cathode. For this reason, the equations related to the calculation of these two parameters will be reported.

Since the process at the cathode side should not be affected by the fuel typology fed at the anode, the results obtained from the oxygen variation carried out on the sample fed with the CO/CO₂ mixture are valid also for the H₂/H₂O and syngas mixtures.

Reaction orders

The dependency of the charge transfer resistance at the anode side to the molar fractions of CO and CO₂ are expressed by Equation 5.23 and Equation 5.24.

$$\log(R_{ct,anode}) = \log\left(\frac{RT}{2F i_{0,anode}^{pre} (x_{CO_2,bulk})^{\gamma_{CO_2}} \exp\left(\frac{E_{act,anode}}{RT}\right)}\right) - \gamma_{CO} \cdot \log(x_{CO,bulk}) \quad (5.23)$$

$$\log(R_{ct,anode}) = \log\left(\frac{RT}{2F i_{0,anode}^{pre} (x_{CO,bulk})^{\gamma_{CO}} \exp\left(\frac{E_{act,anode}}{RT}\right)}\right) - \gamma_{CO_2} \cdot \log(x_{CO_2,bulk}) \quad (5.24)$$

In Figure 5.19 and 5.20 below, there are reported the experimental values of $R_{ct,anode}$ as a function of CO and CO₂ molar fractions, respectively, in log-log plots.

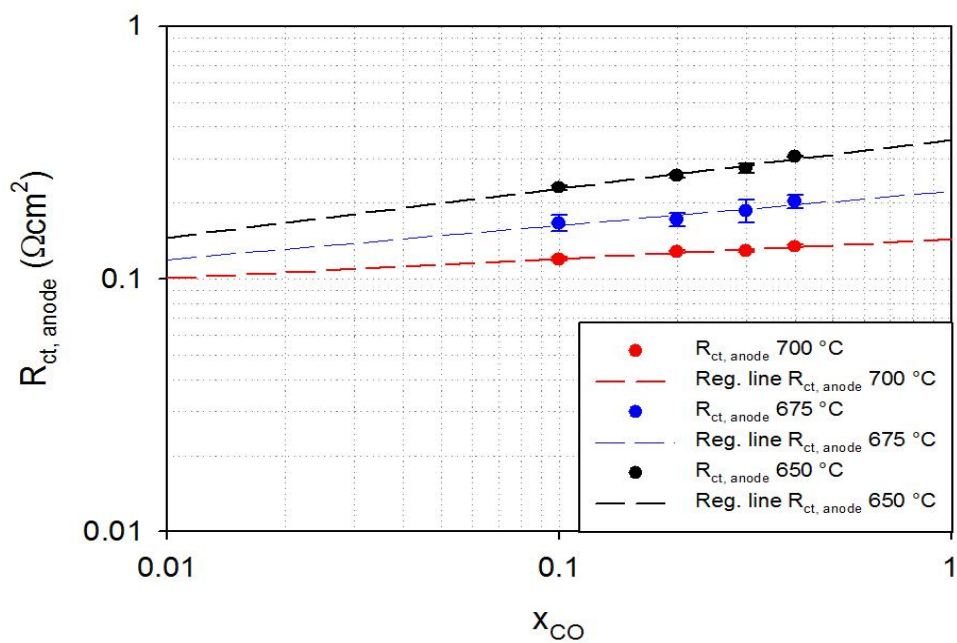


Figure 5.19. Charge transfer resistance in the anode as a function of the carbon monoxide molar fraction at 700 °C, 675 °C and 650 °C.

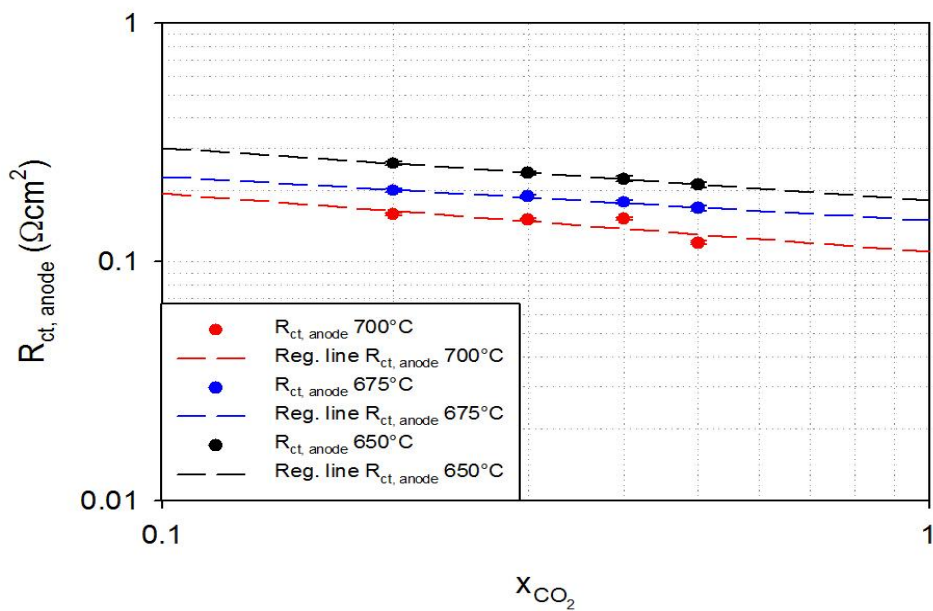


Figure 5.20. Charge transfer resistance in the anode as a function of the carbon dioxide molar fraction at 700 °C, 675 °C and 650 °C.

In analogy with the calculations reported for the case of H₂/H₂O fuel, from the slope of the regression lines of the plots $R_{ct,anode}$ vs x_{CO} and $R_{ct,anode}$ vs x_{CO_2} , values of $\gamma_{CO} = -0.13$ and $\gamma_{CO_2} = -0.22$ were obtained. Leonide et al. report, for a standard SOFC comprised of a technical Ni-YSZ anode and LSCF cathode and fed with CO/CO₂, $\gamma_{CO} = -0.059$ and $\gamma_{CO_2} = -0.25$ ⁸⁷.

For what concerns the reaction order for the cathode semi-reaction, the resistance associated to the charge transfer in the SOFC cathode is expressed analogously to that of the anode, differentiating the cathode activation overpotential with respect to the current density.

$$R_{ct,cathode} = \frac{RT}{2F i_{0,cathode}^{pre} (x_{O_2,bulk})^{\gamma_{O_2}} \exp\left(-\frac{E_{act,cathode}}{RT}\right)} \quad (5.25)$$

The reaction order of the oxygen (γ_{O_2}) can be estimated from the experimental results by applying logarithms to both sides of the preceding equation and expressing the new equation in terms of a first-order polynomial where γ_{O_2} represent the slope of the line.

$$\log(R_{ct,cathode}) = \log\left(\frac{RT}{2F i_{0,cathode}^{pre} \exp\left(-\frac{E_{act,cathode}}{RT}\right)}\right) - \gamma_{O_2} \log(x_{O_2,bulk}) \quad (5.26)$$

Figure 5.21 reports the log-log plot $R_{ct,cathode}$ as a function of x_{O_2} .

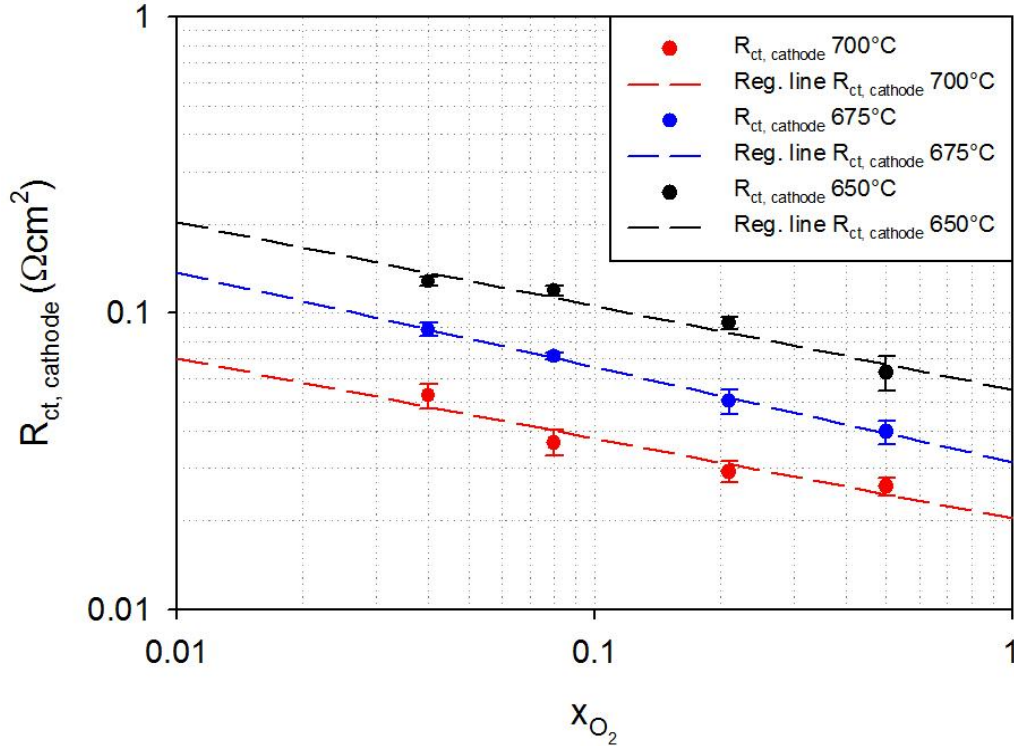


Figure 5.21. Charge transfer resistance in the cathode as a function of the oxygen molar fraction at 700 °C, 675 °C and 650 °C.

From the slope of the linear regressions, a mean value of $\gamma_{O_2} = 0.29$ was calculated. Other authors report a value of 0.22 for an LSCF cathode⁸².

Activation energy and pre-exponential factor

The activation energy and the pre-exponential factor for the oxidation of CO at the anode side can be estimated from the dependency of the resistance to the charge transfer mechanism at the anode with respect to the operating temperature, identically to what was performed for the case with H₂. Figure 5.22. depicts the trend of the charge transfer resistance at the anode side with the varying of the operating temperature, for the 4 different CO molar fractions tested.

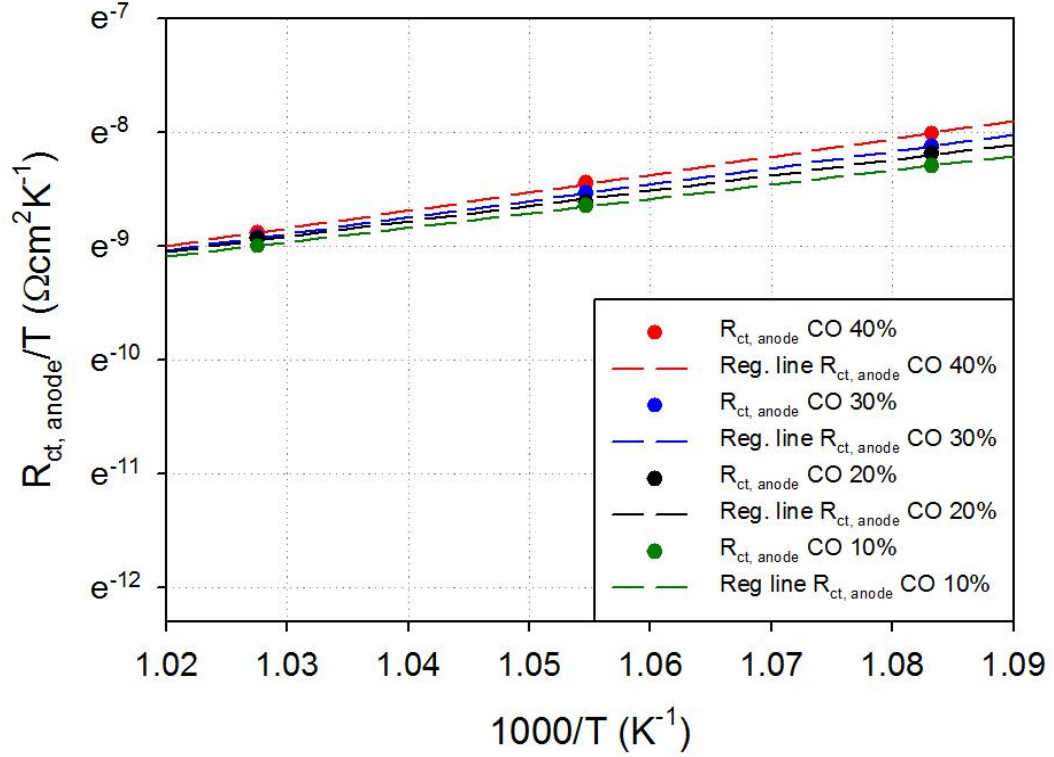


Figure 5.22. Charge transfer resistance in the anode as a function of the temperature for different carbon monoxide molar fractions.

Employing Equation 5.7, written in the case of CO/CO₂ mixtures:

$$\ln\left(\frac{R_{ct,anode}}{T}\right) = \ln\left(\frac{R}{2Fi_{0,anode}^{pre} (x_{CO,bulk})^{y_{CO}} (x_{CO_2,bulk})^{y_{CO_2}}}\right) + \frac{E_{act,anode}}{RT} \quad (5.27)$$

The activation energy and the pre-exponential factor for the electrochemical oxidation reaction of CO to CO₂ can be calculated from the slope and the intercept of the regression lines obtained for the experimental values of $\ln\left(\frac{R_{ct,anode}}{T}\right)$ vs $\frac{1}{T}$. A mean activation energy was calculated of $E_{act,anode} = 117.1 \text{ kJ} \cdot \text{mol}^{-1}$, and a pre-exponential factor of $i_{0,anode}^{pre} = 7.5 \cdot 10^6 \text{ A} \cdot \text{cm}^{-2}$. Both values are again in good agreement with what is reported by Leonide et al. from their DRT/ECM analysis of a CO/CO₂ fed SOFC standard cell: they calculated values of $E_{act,anode} =$

$118.64 \text{ kJ} \cdot \text{mol}^{-1}$ and $i_{0,anode}^{pre} = 4.43 \cdot 10^5 \text{ A} \cdot \text{cm}^{-2}$ for the activation energy and the pre-exponential factor, respectively ⁸⁷.

Considering the electrochemical reaction at the cathode side, Equation 5.28. arises analogously to the anode reaction:

$$\ln\left(\frac{R_{ct,cathode}}{T}\right) = \ln\left(\frac{R}{2Fi_{0,cathode}^{pre}(x_{O_2,bulk})^{\gamma_{O_2}}}\right) + \frac{E_{act,cathode}}{RT} \quad (5.28)$$

Figure 5.23 reports the trend of the charge transfer resistance at the cathode side with varying operating temperature, for the 4 different O₂ molar fractions tested.

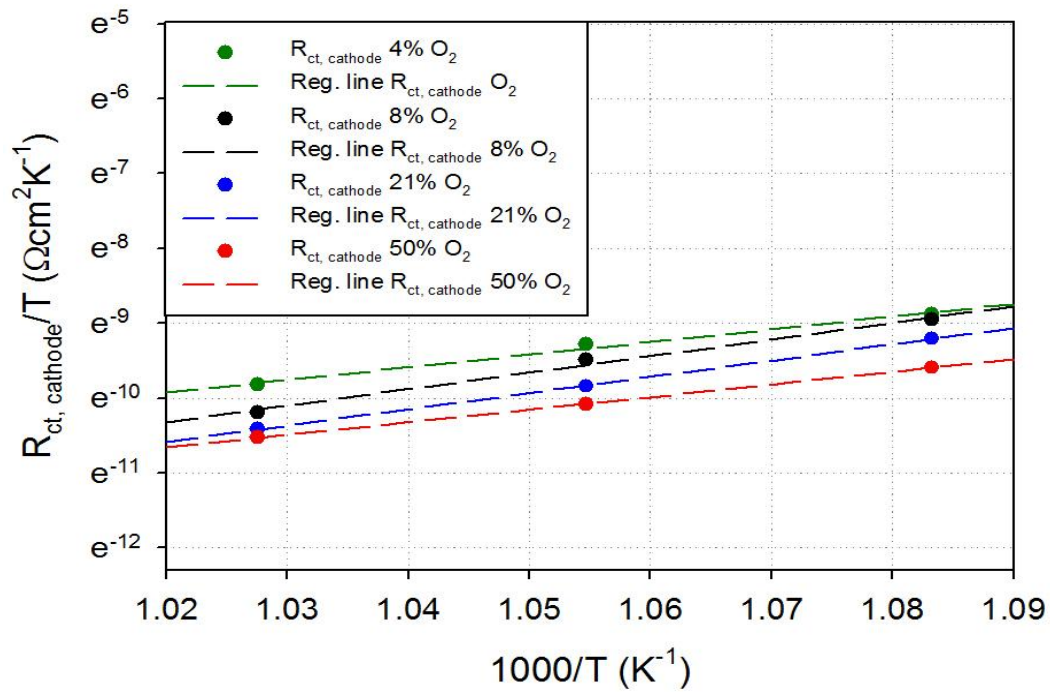


Figure 5.23 Charge transfer resistance in the cathode as a function of the temperature for different oxygen molar fractions.

The activation energy and the pre-exponential factor for the electrochemical reduction reaction of O₂ is again calculated from the slope and the intercept of the regression lines depicted in the

figure above. A mean activation energy was calculated of $E_{act, cathode} = 159.63 \text{ kJ} \cdot \text{mol}^{-1}$, and a pre-exponential factor of $i_{0,cathode}^{pre} = 1.01 \cdot 10^8 \text{ A} \cdot \text{cm}^{-2}$. Again, values reported in literature agrees with this findings; in fact, from analogous investigations on standard SOFCs values were obtained of $E_{act, cathode} = 139.86 \text{ kJ} \cdot \text{mol}^{-1}$ and $i_{0,cathode}^{pre} = 1.47 \cdot 10^7 \text{ A} \cdot \text{cm}^{-2}$ ^{76, 82}.

Diffusion coefficients

Considering the CO/CO₂/N₂ mixtures tested, the expression of the resistance to the gas diffusion within the anode porous matrix can be expressed by Equation 5.21., presented for the case of H₂/H₂O/N₂ mixtures.

In Figures 5.24 and 5.25 below, the values of $R_{diff, anode}$ extracted from the CNLS fitting of the EIS spectra are reported as a function of the molar fraction of carbon monoxide and carbon dioxide, respectively.

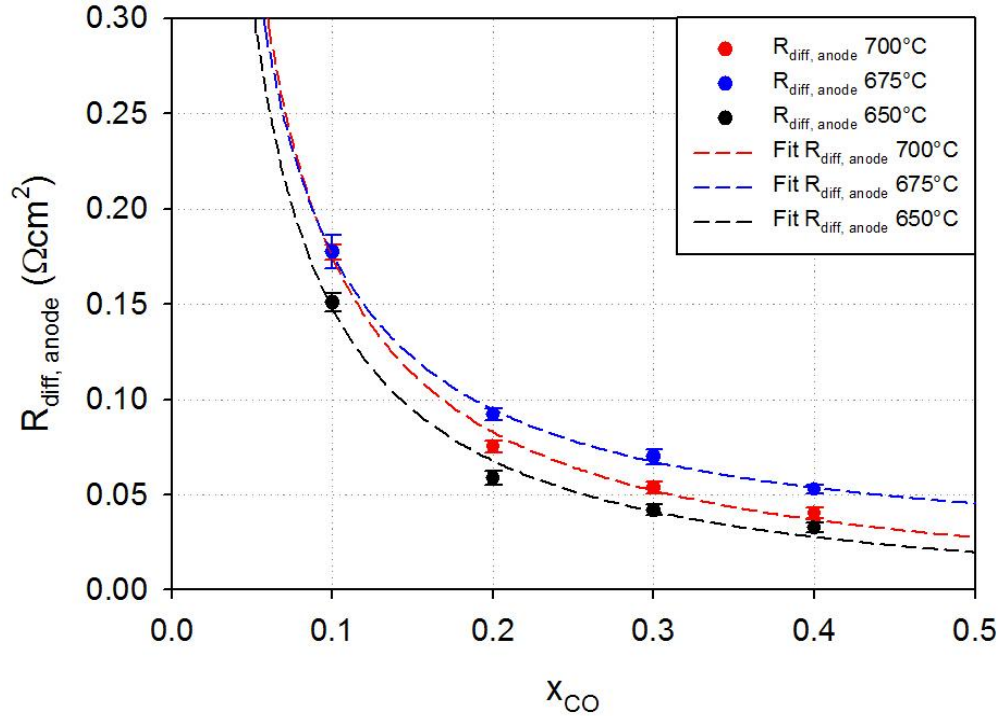


Figure 5.24. Gas diffusion resistance in the anode as a function of the carbon monoxide molar fraction, at 700 °C, 675 °C and 650 °C.

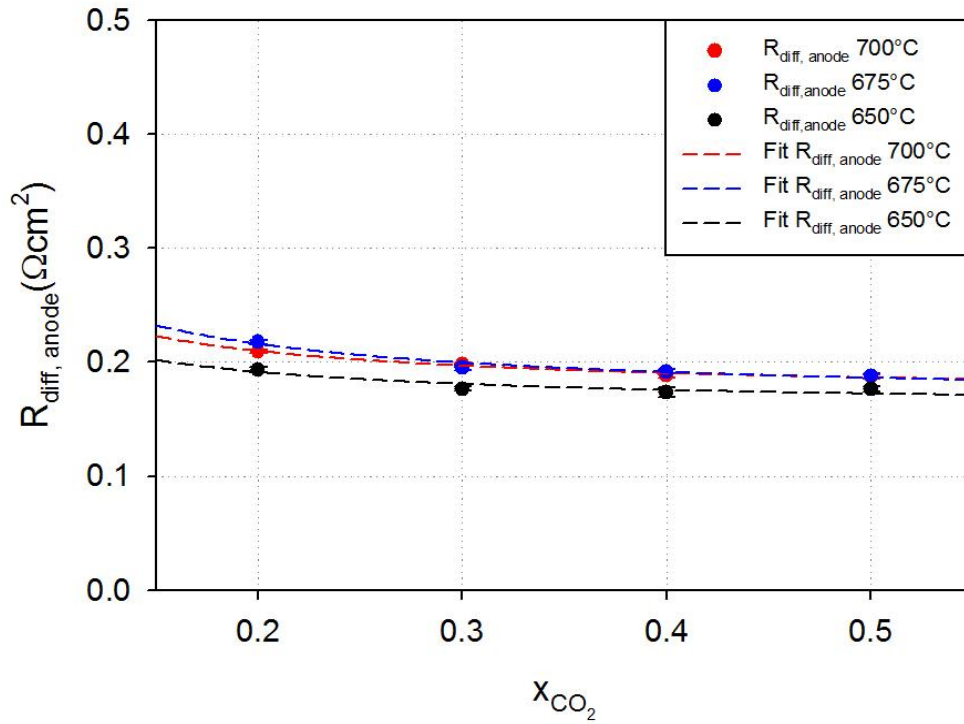


Figure 5.25. Gas diffusion resistance in the anode as a function of the carbon dioxide molar fraction, at 700 °C, 675 °C and 650 °C.

The dashed lines represents the results of the fitting of the experimental values with a model curve; a very high value of r^2 was obtained for each fitting attempt for the case of CO variations ($r^2 = 0.99$), while a mean value of $r^2 = 0.93$ was achieved in the case of CO₂ variations.

With similar calculations as for the case of H₂/H₂O/N₂, mean values for the ternary diffusion coefficients of $D_{CO,T}^{eff} = 3.94 \cdot 10^{-5} m^2 s^{-1}$ and $D_{CO_2,T}^{eff} = 8.6 \cdot 10^{-5} m^2 s^{-1}$ were obtained.

5.2.3. Syngas operation

In this Section, the extracted values of resistances related to the cell processes will be analyzed with respect to the variations of the syngas fuel composition and to the change in operating temperature.

The syngas mixtures tested in this work are all composed of five components, as reported in Chapter 4: H₂, H₂O, CO, CO₂ and balanced in N₂. Thus, the equations illustrated in Section 5.2.1 and 5.2.2 should not be employed as they are, being valid only in the case of binary or ternary gas systems. Nevertheless, in order to compare the results obtained from the cell fed with syngas compositions with those previously obtained from H₂/H₂O and CO/CO₂ mixtures, the following approximation of the system will be assumed: since H₂ and CO are considered fuel for an SOFC, and H₂O and CO₂ are their product, H₂ and CO will be treated as “fuel”, while H₂O and CO₂ will be treated as “product”. In this way, the system can be approximated to a ternary generic system of the type: fuel/product/N₂. This approximation is also experimentally coherent since in all the variation of fuel species H₂ and CO were varied together and by the same quantity, as well as H₂O and CO₂. This simplification will become instrumental for the estimation of all the parameters extrapolated in the H₂/H₂O and CO/CO₂ cases and will allow an interesting discussion of the experimental results.

Reaction orders

Following the same considerations described in the previous cases, Figure 5.26 and 5.27 report the values of the charge transfer resistance at the anode with a variation of H₂-CO and H₂O-CO₂ in the syngas mixture, respectively.

It is worth mentioning that during the measurement at T = 650 °C with $x_{H_2} = x_{CO} = 0.4$, the tested sample showed an incoherent response, resulting in a higher impedance (both in the high frequency and low frequency part of the spectra) than what was expected, probably indicating a degradation of the cell performances occurring during the test. Even though the resulting values are reported in the plot, being outliers with respect to the overall trend, the results were not considered in the calculations of the parameters.

This evidence will result more pronounced in the plots $R_{diff,anode}$ vs $x_{H_2,CO}$, where the value of the resistance at that composition and temperature resulted c.a. 200% higher than expected; for these reasons, these results are excluded from the analysis.

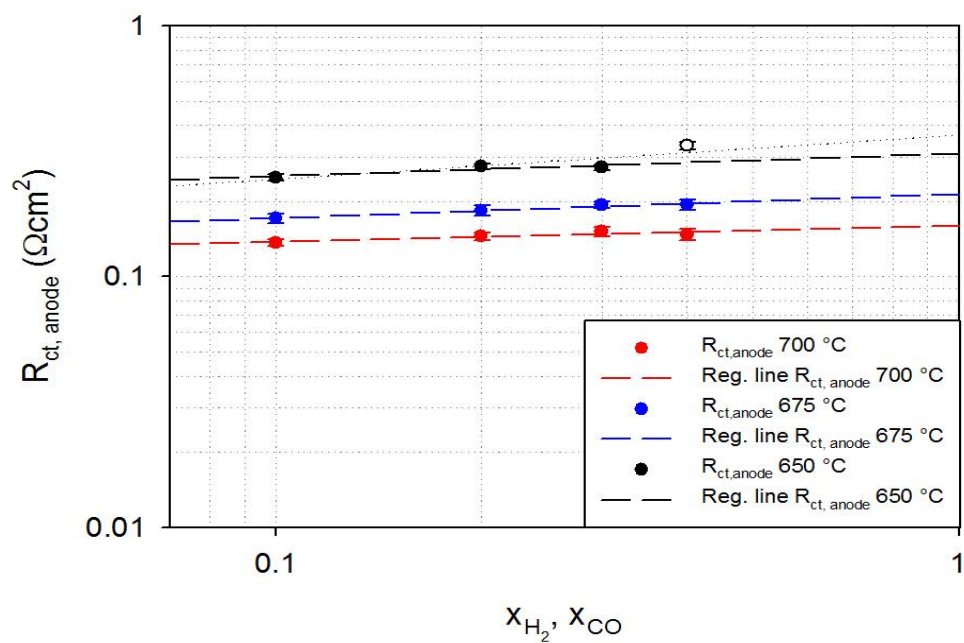


Figure 5.26. Charge transfer resistance in the anode as a function of the H_2 -CO molar fractions at 700 °C, 675 °C and 650 °C.

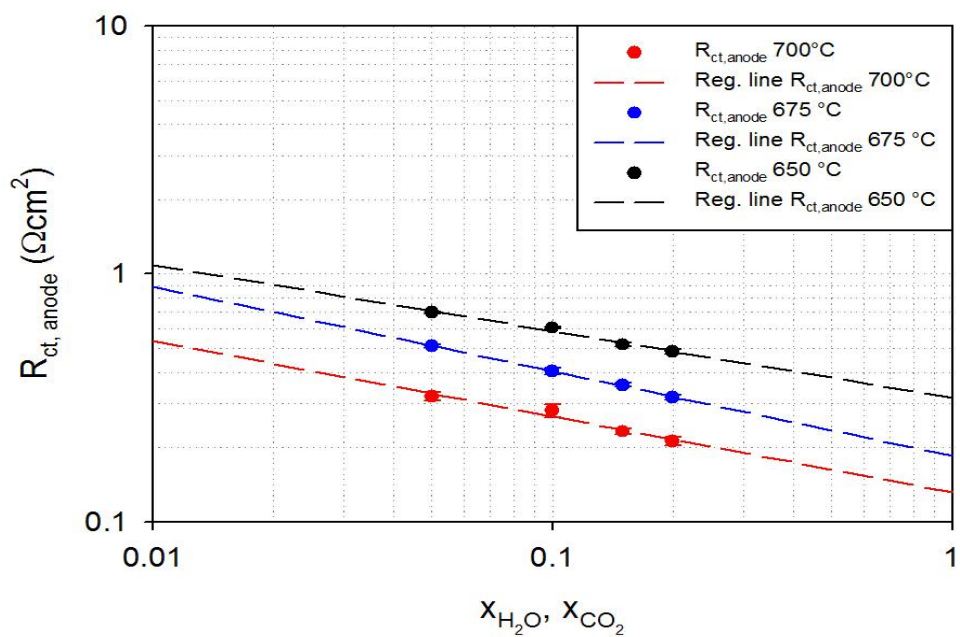


Figure 5.27. Charge transfer resistance in the anode as a function of the H_2O - CO_2 molar fractions at 700 °C, 675 °C and 650 °C.

From the slope of the regression lines reported in the figures above, values of $\gamma_{H_2,CO} = -0.083$ and $\gamma_{H_2O,CO_2} = 0.31$ were obtained for the reaction orders with syngas fuel. A. Kromp et al.^{66, 86} report values of $\gamma_{H_2,CO} = -0.04$ and $\gamma_{H_2O,CO_2} = 0.32$ employing the same methodology. Comparing the reaction orders obtained for the syngas fuel with those obtained for H₂/H₂O and CO/CO₂, it results that the value of $\gamma_{H_2,CO}$ is closer to that of γ_{H_2} rather than that of γ_{CO} , and also close to that obtained from Leonide et al.^{76, 82} with H₂ ($\gamma_{H_2} = 0.10$). Moreover, the value of $\gamma_{H_2O,CO_2} = 0.31$ is very close to that obtained from A. Kromp et al., and also to that obtained from the same group in the case of H₂/H₂O fuel ($\gamma_{H_2O} = 0.33$).

Even though the value obtained in this work for γ_{H_2O} is very low, with the reasons mentioned in Section 5.2.1, these findings may suggest that the mechanism for the electrochemical oxidation of the fuel with syngas is similar to that occurring when the cell is fed with H₂.

Further confirmation of this hypothesis will be provided from the results obtained for the activation energy for the fuel oxidation process reported hereafter.

Activation energy and pre-exponential factor

The activation energy and the pre-exponential factor for the oxidation of fuel species in the syngas at the anode side can be again estimated from the dependency of the resistance to the charge transfer mechanism at the anode with respect to the operating temperature, identically to what was performed for the case with H₂. Figure 5.28. reports the values of the charge transfer resistance at the anode side with the varying of the operating temperature, for the 4 different syngas compositions employed.

Also in this plot, the value obtained from the measurement undertaken at measurement at T = 650 °C with $x_{H_2} = x_{CO} = 0.4$, even if depicted in the plot, was not taken into consideration for the calculation of the activation energy and the pre-exponential factor, for what previously stated.

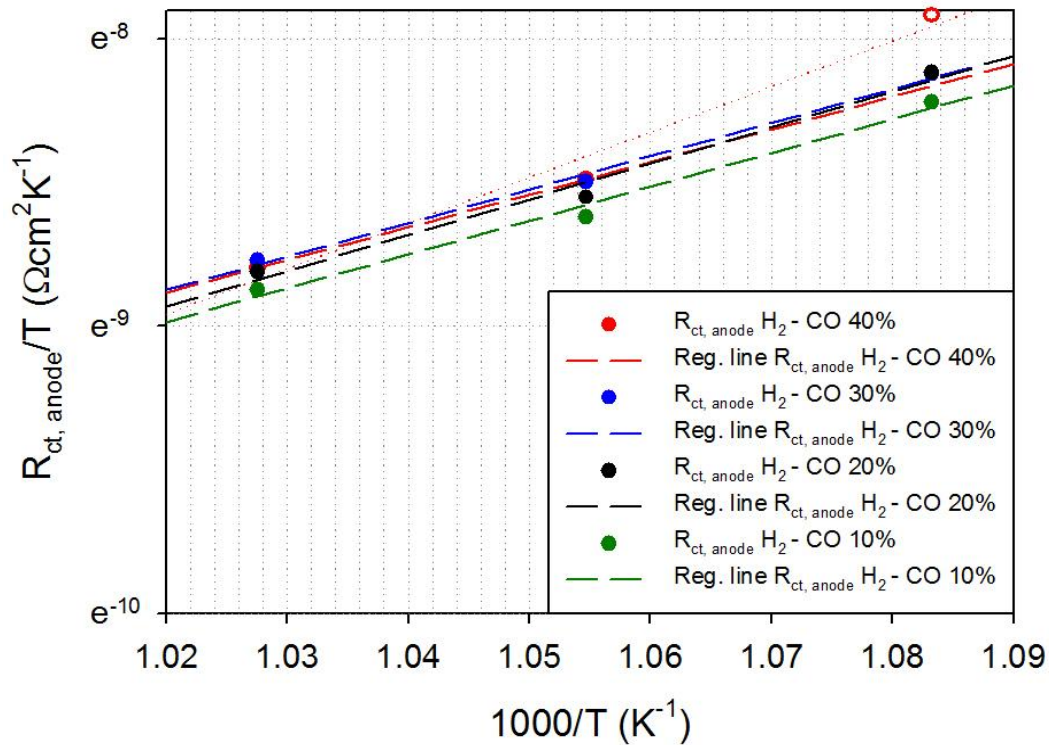


Figure 5.28. Charge transfer resistance in the anode as a function of the temperature for different syngas compositions.

From the slope of the interpolating lines, a mean value of $E_{act,anode} = 95.57 \text{ kJ} \cdot \text{mol}^{-1}$ was calculated for the activation energy of the oxidation reaction of the fuel. This value is closer to that obtained for the oxidation of H_2 rather than that for the oxidation of CO , further suggesting that the oxidation mechanism of the fuel at the anode side of a SOFC fed with a syngas is similar to that occurring when the same cell is fed with humidified hydrogen.

Thus, it can be assumed that H_2 is preferentially electrochemically oxidized at the anode, while the CO is rather converted to H_2 by means of the water gas shift reaction (WGS), the presence of which being evidenced by the presence of the process P_5 in the DRT plots.

A Kromp et al. found a value for the activation energy of the oxidation of the fuel in a syngas of $E_{act,anode} = 106.1 \text{ kJ} \cdot \text{mol}^{-1}$ ^{76, 79, 86} which resulted extremely close to that obtained for the same cell fed with humidified hydrogen ($E_{act,anode} = 109.03 \text{ kJ} \cdot \text{mol}^{-1}$); being almost identical, they also stated that H_2 is the only fuel species to be electrochemically oxidized.

Nevertheless, in the case examined in this work, the higher value obtained for the oxidation of the fuel in the syngas may suggest that the oxidation kinetic is slowed down. An hypothesis can be the occupation of Ni catalytic sites for the concomitant occurrence of the water gas shift reaction: however, this particular hypothesis needs to be experimentally demonstrated.

Finally, from the intercept of the interpolating lines with the y axis of the plot in Figure 5.28 above, a value of $i_{0,anode}^{pre} = 4.25 \cdot 10^6 A \cdot cm^{-2}$ was found, again very similar to that obtained in H_2/H_2O fuel.

Diffusion coefficients

Figure 5.29 and 5.30 below, depict the trends of $R_{diff, anode}$ as a function of $x_{H_2} (= x_{CO})$ and $x_{H_2O} (= x_{CO_2})$. In Figure 5.29 it is particularly evident how the measurement carried out at $T = 650 \text{ }^\circ\text{C}$ with $x_{H_2} = x_{CO} = 0.4$ was affected by some sort of degradation effect on the cell. Again, this measurement was not taken into account for the calculation of the diffusion coefficients.

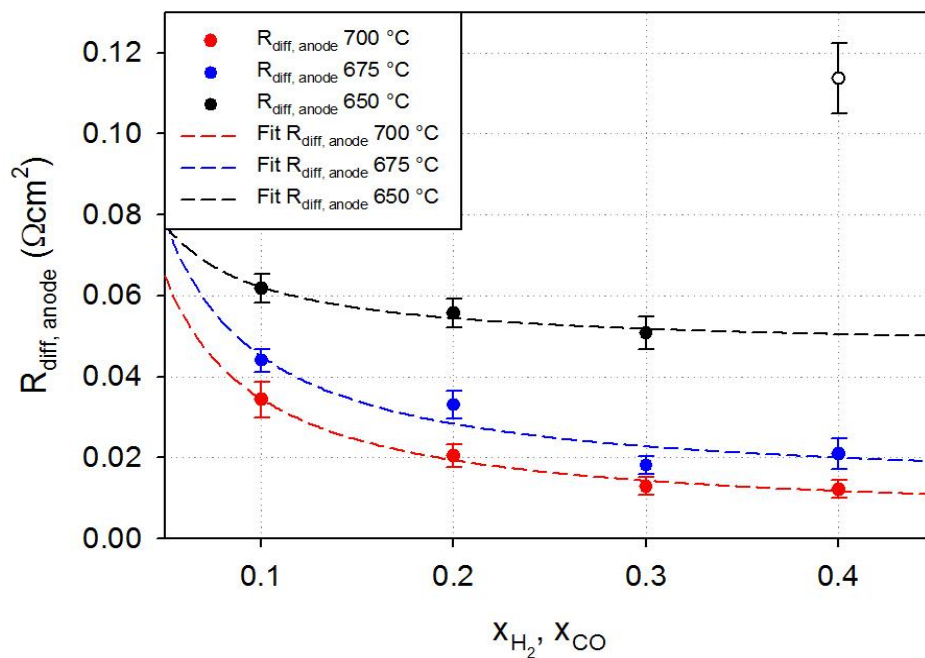


Figure 5.29. Gas diffusion resistance in the anode as a function of the H_2 - CO molar fractions at 700 °C, 675 °C and 650 °C.

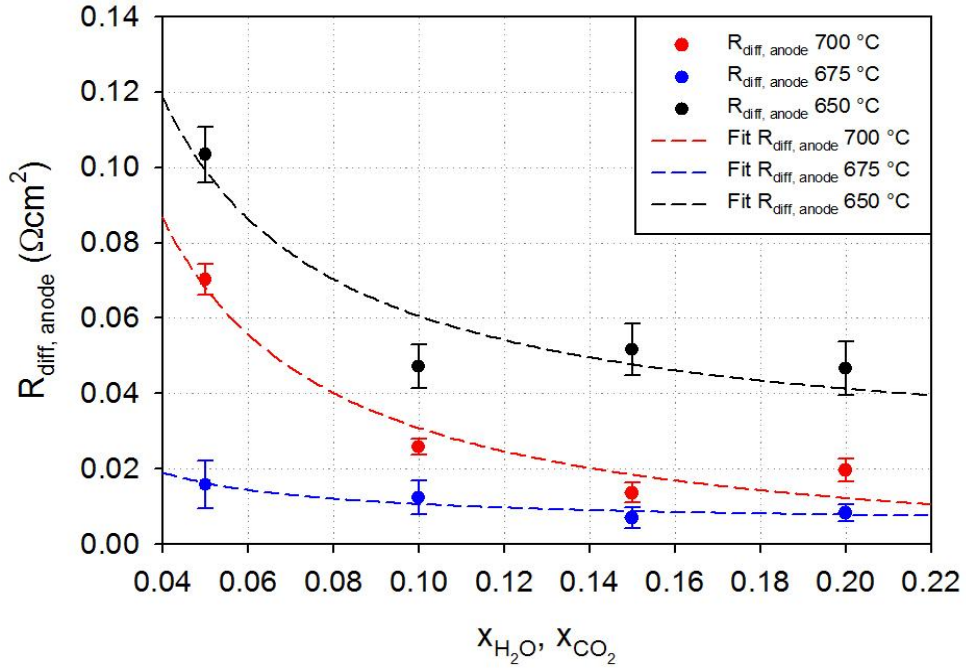


Figure 5.30. Gas diffusion resistance in the anode as a function of the H_2O-CO_2 molar fractions at 700 °C, 675 °C and 650 °C.

Applying the expressions presented in Section 5.2.1, and assuming valid the approximation described at the beginning of this Section, the effective ternary diffusion coefficients can be calculated. It is worth noting that even in this case the interpolations had a high coefficient of determination, both for the H_2-CO ($r^2 = 0.95$) and for the H_2O-CO_2 ($r^2 = 0.9$) variations.

The calculations provided the values of $D_{H_2-CO,T}^{eff} = 2.75 \cdot 10^{-4} m^2 s^{-1}$ and $D_{H_2O-CO_2,T}^{eff} = 4.8 \cdot 10^{-4} m^2 s^{-1}$.

5.2.4. Resume of the estimated parameters

By the application of the synergic approach of *in-operando* impedance spectroscopy measurements under a wide number of different and pre-defined operating conditions, distribution of relaxation times method, and CNLS fitting of the experimental EIS measurement with an equivalent circuit model defined from the identification of the processes presented in Section 5.1, it has been possible to estimate a broad number of physical quantities for each fuel

typology, that characterize the principal equations at the basis of the operation of a SOFC. Activation energies, reaction orders, and pre-exponential factors provided a complete picture of the kinetics of the electrochemical reactions occurring at the anode and at the cathode side, for the three fuels tested: H₂/H₂O, CO/CO₂ and syngas.

Comparing the obtained results in this work in the three cases between them, and with what has been reported by other authors in literature, it has been possible to hypothesize that in the case of a syngas fuel, the oxidation mechanism of the fuel is similar to that occurring in the case of humidified hydrogen, suggesting that H₂ is preferentially oxidized at the anode side. The carbon monoxide is rather involved in the Water Gas Shift reaction, in order to produce more H₂ to be further oxidized; this evidence resulted strongly supported in literature. Nevertheless, in contrast with the findings of other research groups employing a similar approach for the calculation of these physical quantities, a lower activation energy was obtained for the oxidation reaction in H₂/H₂O rather than in syngas: this evidence suggests that, even if H₂ is the gas species to be electrochemically converted, in the case of syngas fuels a slowdown in the reaction kinetics may occur due to the concomitant presence of the Water Gas Shift reaction, which may interfere with the catalytic sites at the anode TPB.

The most important result obtained in this Section, was to prove that this methodology is able to quantitatively and fully characterize all the processes (mass transport, charge transfer, ohmic conduction) starting from measurements obtained from realistic and *in-operando* conditions. In this way, the estimated parameters will generate new and more reliable computational models based on the experimental measurements of these physical quantities, or may be helpful in the investigation of novel materials or structural morphology and architecture with the aim of further improving SOFC efficiencies and stability.

It is also important to note that the DRT/CNLS/ECM methodology employed in this work provided results that are always comparable and in good agreement with the findings of other authors employing the same methodology, with the slight differences mostly related to the fuel cell type (standard SOFC respect to IT-SOFC), materials (LSCF respect to LSC cathodes), dimensions, morphology and manufacturer. This evidence suggest that the DRT-based analysis results in a reliable, reproducible and very informative analysis tool for the investigation of SOFC systems.

5.3. Endurance performance in syngas

In this Section, the results obtained from an endurance test carried out on a IT-SOFC button cell sample fed with a simulated clean syngas (composition in Chapter 4) under a constant current density of 0.5 Acm^{-2} for up to 1000 hours of operation are presented.

In the first part, the evolution of the performances were investigated by means of the same DRT/CNLS fitting approach presented in the previous Sections, and the results obtained were analyzed in order to pinpoint the critical processes which degraded most during the test.

In the second part, by means of a post-mortem analysis, the information provided by the DRT/CNLS study were related to possible degradation effects highlighted by XRD and SEM/EDX analysis.

5.3.1. Degradation of cell performances

In Figure 5.31 there are reported the polarization curves recorded at different times during the endurance test. It can be noted that for the first 530 hours of operation, only a slight reduction in the overall performances of the cell can be appreciated, while a significant decrease is observable after 800 hours and after 1000 hours of operation. Even though the *i*-*V* curves indicates a loss in the cell efficiency over time, they do not say anything about the mechanism of degradation and which processes are affected the most.

Analyzing the EIS measurements, collected together with the *i*-*V* curves, and calculating the DRT functions for each spectrum, more in-depth information about the time evolution of the processes was achieved.

Observing the DRT plots depicted in Figures 5.32 and 5.33, it is evident that for the first 530 hours, only a minor degradation effect is evident, involving the charge transfer process at the cathode side P_3 ; nevertheless, at the same time, a sort of activation phenomenon involving the anode charge transfer processes seems to balance the negative effect of the initial worsening of the process P_3 , and thus resulting only in a minor overall performance losses.

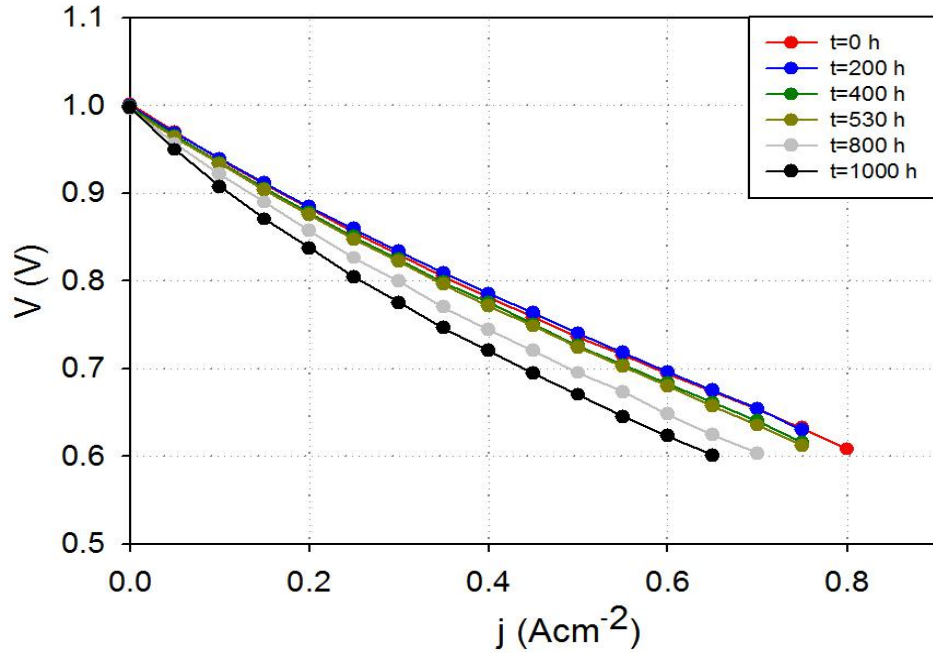


Figure 5.31. Polarization curves recorded at different operating times, at $T = 650\text{ }^{\circ}\text{C}$, with syngas fuel.

A more pronounced modification of the anodic processes can be appreciated between 530 h and 1000 h: while process P_1 remains unaltered, the intensity of process P_2 increases dramatically, becoming the most intense one. In conjunction with the increase of P_2 , a slight increment in the magnitude of anodic processes P_4 and P_5 , related respectively to the gas diffusion and the WGS reaction in the anode substrate, can be observed.

Furthermore, the cathodic process P_3 continues to increment its intensity during the rest of the test.

By applying the CNLS fitting of the experimental data with the ECM model depicted in Figure 5.12, the temporal evolution of the single resistances associated to each physicochemical process was obtained and reported in Figure 5.34.a; moreover, in Figure 5.34.b there are reported the values of the overall resistance to the anodic charge transfer process along with the values of the separated processes P_1 and P_2 which contribute to the overall mechanism.

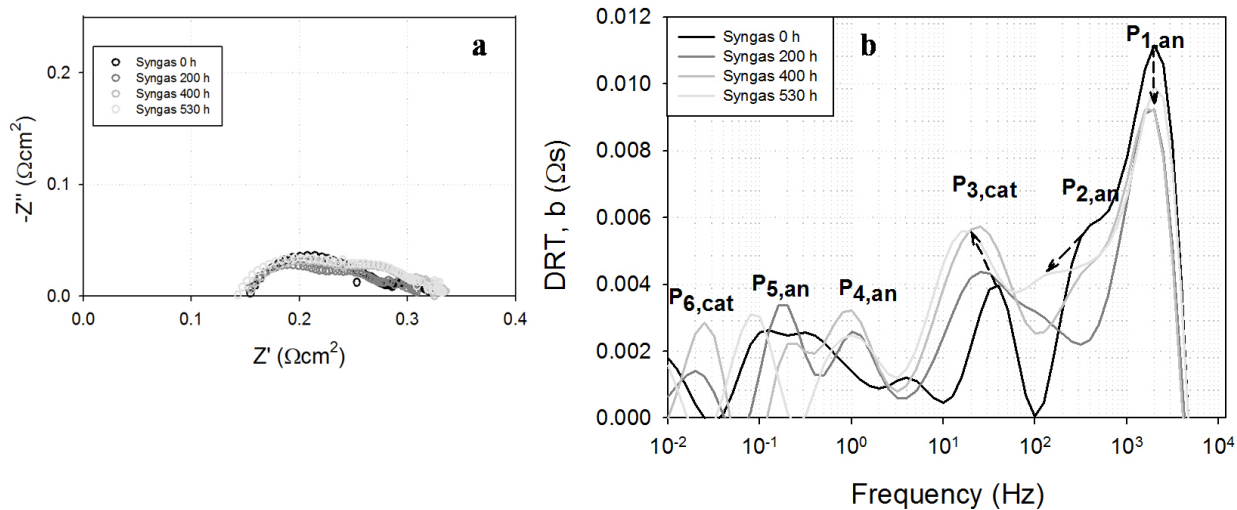


Figure 5.32. EIS measurements (a) and corresponding DRT functions (b) obtained at different operating times between 0 hours and 530 hours.

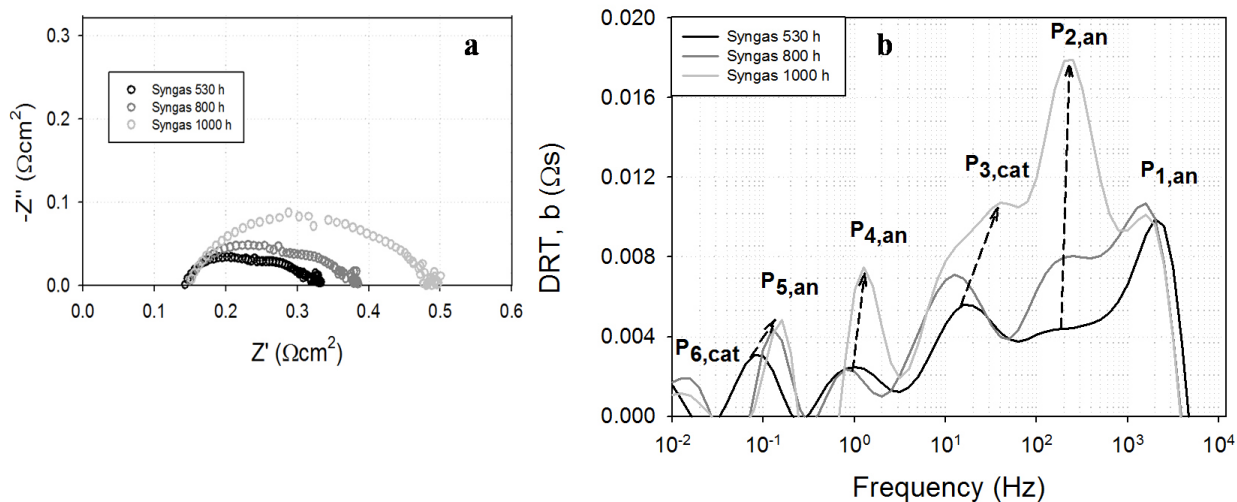


Figure 5.33. EIS measurements (a) and corresponding DRT functions (b) obtained at different operating times between 530 hours and 1000 hours.

Considering the values of the resistances extracted from the CNLS fitting procedure, it appears evident that the limiting process for the cell performance is always, in terms of absolute values, the anodic charge transfer process ($P_1 + P_2$). This process, taken as a sum, increases its impedance up to 100% in 1000 hours of operation, and observing the Figure 5.34.b it is evident

that the contribution to its increment is all ascribable to the process P_2 , which was previously ascribed to the charge transfer mechanism at the three phase boundary within the anode functional layer, while the process P_1 , previously assigned to the ionic transport of O^{2-} within the YSZ lattice, results almost unaffected from the long term operation.

The other anodic processes, the gas diffusion process in the anode porous matrix and the one related to the Water Gas Shift reaction (processes P_4 and P_5) increase only in the last 200 hours of operation and, apparently, as a consequence of the dramatic increase of the process P_2 .

The resistance associated to the charge transfer mechanism at the cathode side (process P_3) is the one that increases its impedance the most, increasing up to 3 times its initial value in 1000 hours.

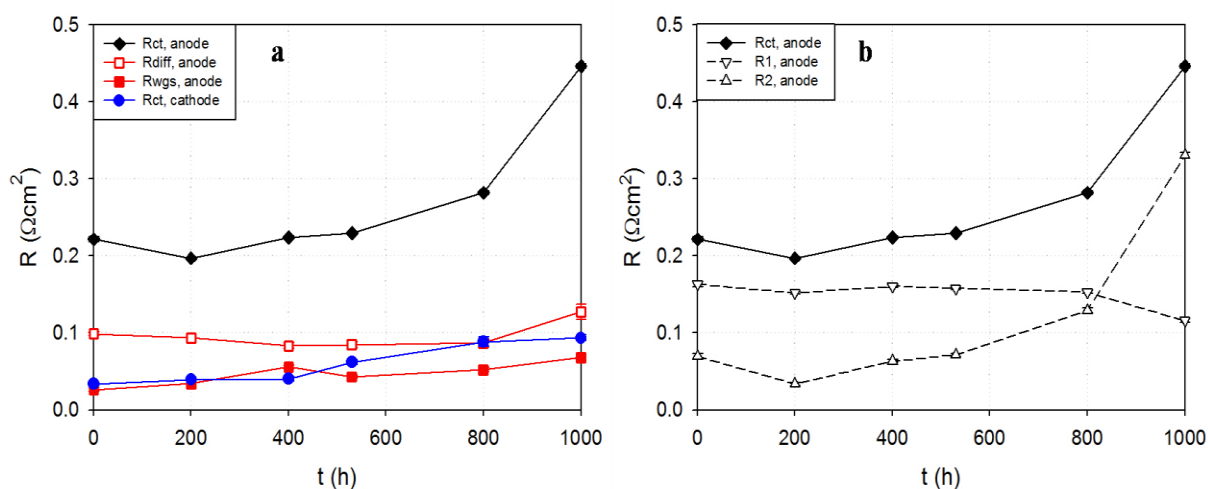


Figure 5.34. Polarization resistances of the button cell sample during the long-term test at 650°C. (a) Extrapolated resistances values for the operating processes within the cell; (b) charge transfer resistance at the anode resistances associated to its constituent processes P_1 and P_2 .

The following Section will provide the results of some post mortem characterization, and the observations collected from both in operando and post mortem analysis will be gathered to explain the degradation phenomena that affected the tested sample.

5.3.2. Post-mortem analysis

In Figure 5.35 below there are reported the XRD spectra measured at $t = 0$ hours and after 1000 hours of operation, of both the anode and cathode layers.

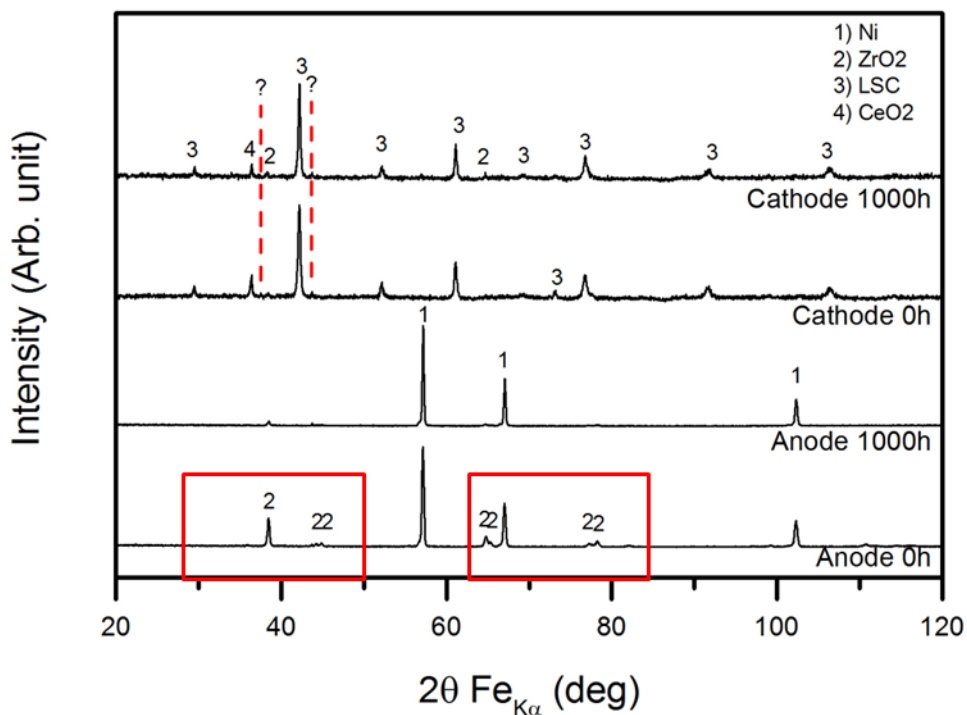


Figure 5.35. XRD spectra obtained for the anode at $t = 0$ h and $t = 1000$ h, and for the cathode at $t = 0$ h and $t = 1000$ h of operation.

For what concerns the anode layer, it is very interesting to note that after 1000 hours, the features related to the ZrO_2 phase completely disappear (marked with the red box), while only the Ni features remain.

Analyzing the XRD patterns for the cathode layer, the features related to LSC and CeO_2 (diffusion barrier) are still present after 1000 hours; however two unrecognized features appear, indicating some sort of modification into the phase composition within the cathode.

Figure 5.36 reports the results obtained from the analysis of the cross section of the cell with SEM images coupled with EDX spectroscopy.

The SEM images of the cross section show that a notable morphology change appears after 1000 hours, in the form of a densification of the structure on the anode surface (bottom part of the image), which is coherent with what was suggested by XRD results.

The EDX mapping of the cathode/diffusion barrier/electrolyte/anode functional layers interface, depicted on the right of Figure 5.36, show a prominent migration of Sr (and to a lesser extent Gd) from the cathode layer through the cell.

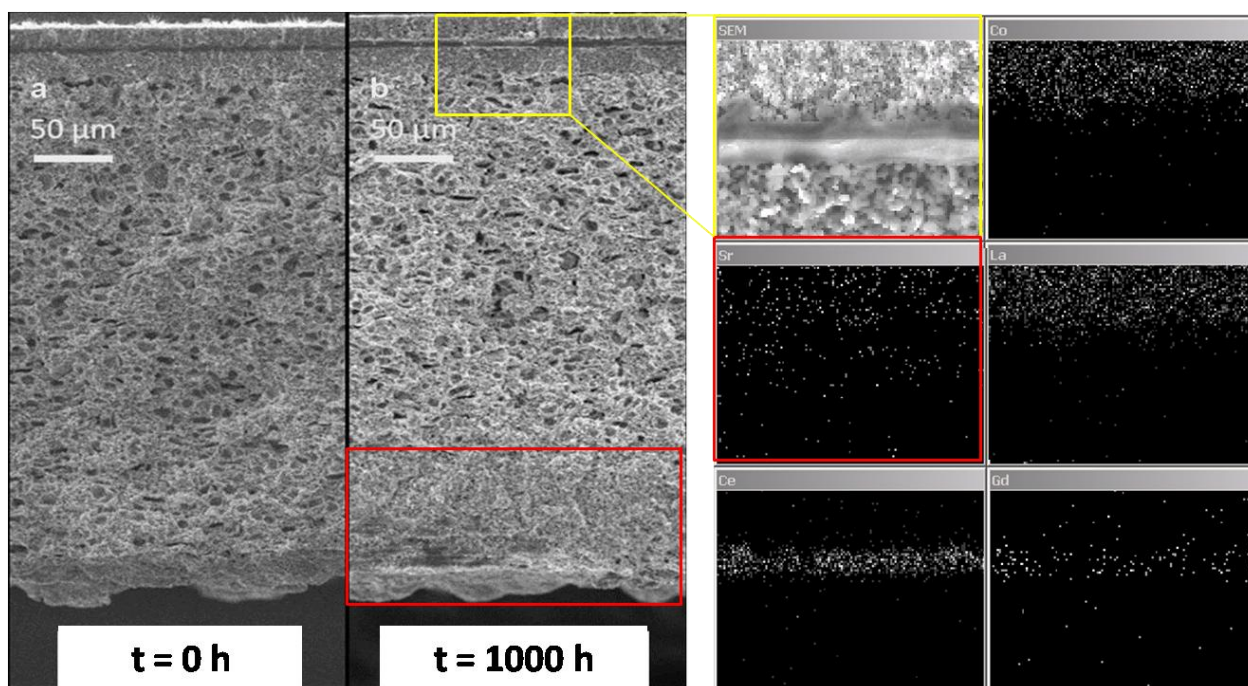


Figure 5.36. (left) SEM images of the cross section of a sample at $t = 0$ hours of operation, taken as reference, and of the sample operated in syngas fuel with a constant current load for $t = 1000$ h. EDX analysis of the cathode/electrolyte/anode functional layers interfaces (right): only the elements of the cathode layer and of the diffusion barrier layer are shown.

5.3.3. Resume of endurance performances in syngas

Considering the results obtained from both in-operando DRT/EIS measurements and post-mortem analysis, the following considerations about the degradation phenomena emerge.

On the anode side, a densification was observed of Ni particles upon the bottom part of the anode support layer. As previously assessed, the process P_2 is related to the charge transfer mechanism occurring in the AFL, which is catalyzed by Ni dispersed particles, while both processes P_4 and P_5 possess the typical behavior related to mass transport phenomena. According to what is observed, it can be hypothesized that a migration of Ni particles from the AFL to the anode support occurred, followed by a subsequent densification, thus explaining the dramatic increase

in P_2 contribution to the impedance, due to the depletion of catalytic active sites, and the concurrent increase in both P_4 and P_5 intensities, due to a reduction of the open porosity within the anode substrate. A known anode degradation phenomenon is the Ni agglomeration and the loss of Ni-Ni contact, which reduces the Three Phase Boundary length, thus increasing the anode polarization resistance^{91, 92}.

For what concerns the cathodic process P_3 , the increment of the impedance related to the charge transfer mechanism at the cathode side was caused by a migration of Sr from the cathode layer through the cell. Furthermore, it is extensively reported in literature that Sr-doped mixed oxides, such as LSC and LSCF, suffer from depletion of Sr content, followed by a subsequent migration toward the electrolyte layer, when employed as cathodes for SOFC, affecting to some extent their effectiveness for the cathode reaction and possibly forming insulating phases at the cathode/electrolyte interface^{93, 94}. Thus, the increase in P_3 impedance during long term operation may be attributed to the depletion of Sr content at the cathode side.

It is worth noting that both degradation phenomena observed for this cell are not directly ascribable to the operation in syngas; the reduced operating temperature does not seem to impede the application of IT-SOFC cells with syngas sources.

5.4. Tar contamination

5.4.1. Effects of tar concentrations

A preliminary electrochemical characterization was carried out in order to evaluate the effect of different concentrations of toluene, taken as a model tar, in the fuel stream.

Polarization curves and EIS spectra in OCV conditions were carried out for the four different tar concentrations on one button cell sample (hereafter BC_tar), and compared to those obtained from a sample fed with the sole syngas and humidified hydrogen (hereafter BC_syngas). The cell was operated at $T = 650$ °C.

All the four different concentrations of toluene are lower than those employed in other experimental works reported in literature, that may reach values up to $10 \text{ g}\cdot\text{m}^{-3}$ for real product gas from biomass gasification systems directly coupled to an SOFC. However, considering the low water content in the fuel stream, the low operating temperature of the IT-SOFCs tested samples and the reduced dimensions of the cells, few hundreds $\text{mg}\cdot\text{m}^{-3}$ of toluene in the anode

flow caused an important drop in the immediate performances of the cell, as evident from the polarization curves depicted in Figure 5.37.

It is also important to note that there is not a clear trend between the performance drop and the concentration of the contaminant. The reason of this apparent discrepancy in the performance of the cell may be explained analyzing the EIS spectra.

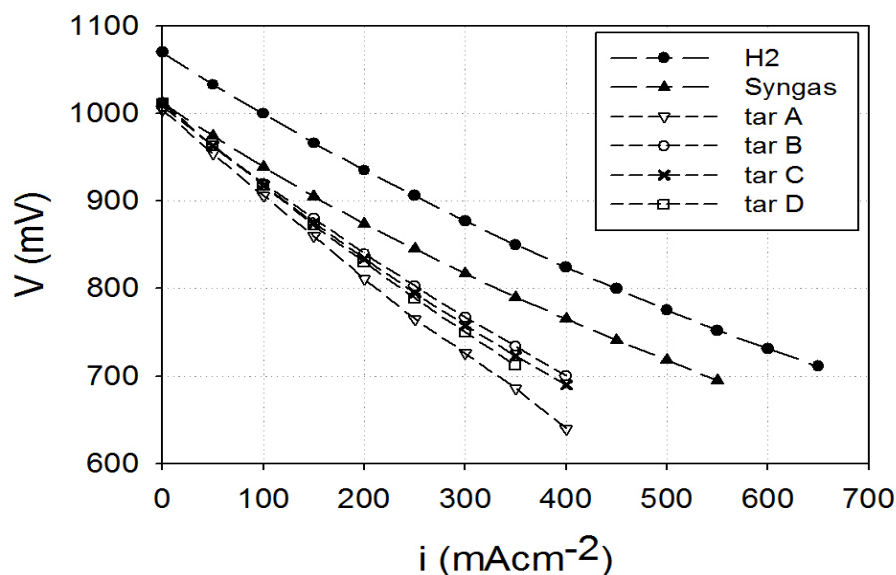


Figure 5.37. Polarization curves obtained from the sample BC_tar, exposed to the different fuel compositions and contaminant concentrations.

In Fig. 5.38.a, the experimental EIS spectra are reported, while in Fig. 5.38.b the impedance values for the internal resistance (R_{int}), the polarization resistance (R_{pol}), and the total resistance ($R_{tot} = R_{int} + R_{pol}$) are plotted against the increasing toluene concentration.

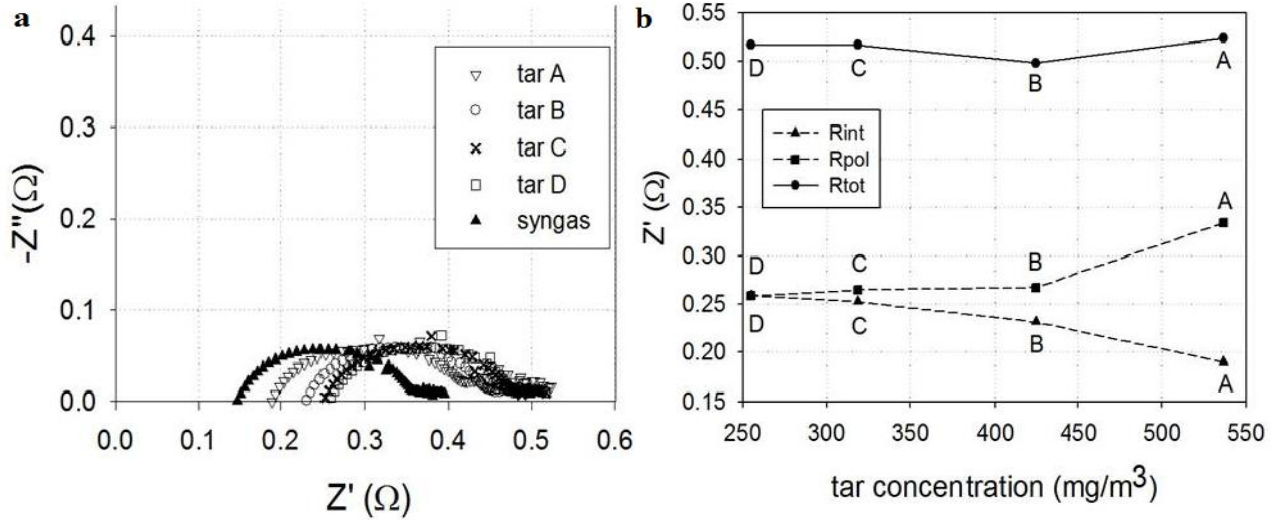


Figure 5.38. (a) Nyquist plots of the EIS spectra. The spectra were recorded in OCV conditions, at $T=650^\circ\text{C}$ for all the compositions. In figure (b), the values of R_{int} , R_{pol} , and R_{tot} , extracted from the experimental spectra, are plotted against the tar concentration in the fuel stream.

Going from composition A to D, the internal resistance R_{int} , related to the ohmic conduction of the cell, increases; an opposite trend emerges for the polarization resistance R_{pol} , which is in turn related to all the charge transfer mechanisms and mass transport phenomena occurring within the cell.

Since the A composition was the first tested, and the D composition the last, the trend of R_{int} may be explained with an initial, very fast deposition of carbonaceous species between the surface of the anode and the anodic current collector, which induced the creation of a resistive layer on the active surface. This phenomenon may have been caused by the OCV condition in which the cell was operated during the EIS measurements. Singh et al.⁹⁵ reported that the OCV condition may cause a very fast carbon deposition on the anode side, if a tar contaminant, such as toluene, is present in the fuel stream.

However, considering these two opposite behaviors of R_{int} and R_{pol} , the trend of the R_{tot} results in good agreement with the trend of the polarization curves reported in Figure 5.37.

5.4.2. Degradation of cell performances

The BC_tar sample was then exposed to the composition Tar D, and operated with a constant current density of $i = 0.4 \text{ A}\cdot\text{cm}^{-2}$ for more than 150 hours. The voltage drop was monitored during time, and the obtained results have been compared to the performance of another identical button cell, namely BC_syngas, operated with the same composition and gas flows, with a constant current density of $i = 0.5 \text{ A}\cdot\text{cm}^{-2}$. The voltage trend of BC_syngas and BC_tar is reported in Figure 5.39. Due to the lower performances of BC_tar, caused by the exposition of the cell to the toluene, the current density was reduced in order to have an initial value of the cell voltage similar to the voltage of BC_syngas at $i = 0.5 \text{ mA}\cdot\text{cm}^{-2}$ ($V_{\text{BCsyngas}} = 0.745 \text{ V}$, $V_{\text{BCtar}} = 0.712 \text{ V}$). However, as represented in Figure 5.39, during the first 10 hours of operation, a fast recovery effect of the voltage of BC_tar occurred, which brought the voltage to be similar to that of BC_syngas.

This recovery effect was probably caused by the intense flow of O^{2-} ions from the cathode side due to the application of the high current density, which most likely helped to liberate and oxidize carbon deposits formed during the preliminary characterization in OCV, and thus enhancing the cell voltage.

This experimental evidence is coherent with the hypothesis of an initial carbon deposition due to the OCV condition, in line with what was stated by Singh et al. with their thermodynamic analysis⁹⁵.

After the first 10 hours, a very rapid degradation of the voltage of BC_tar occurred, compared to that of the BC_syngas. After 150 hours, the voltage reached the value of 600 mV and the long term test was stopped.

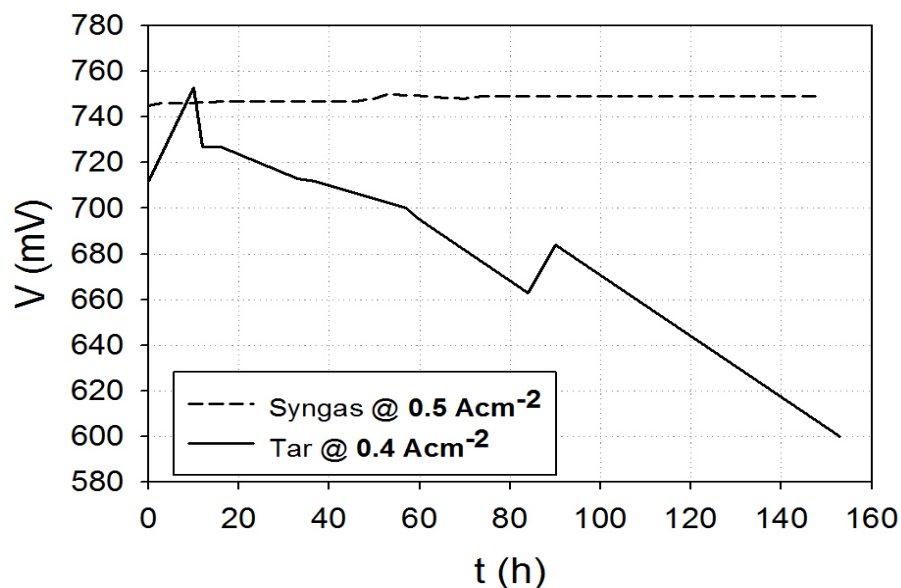


Figure 5.39. Cell voltages (mV) at fixed current density, as a function of time (hours). Tar operating cell performance is compared to that obtained from a cell operating in clean syngas with the same composition and flows.

The very fast degradation observed for the tar-fed sample has been related to the aggravated conditions in which the cell has been operated, rather than the concentration of toluene itself; in fact, the operating temperature of $T = 650^{\circ}\text{C}$ and the low steam content in the fuel stream are critical conditions for a cell operating with tar containing fuels. However, the measured degradation effects are expected to be exacerbated with higher concentrations of tar. Moreover, it is reported in literature that model tars, especially those with a low molecular weight, such as benzene and toluene, have an enhanced reactivity in forming carbon deposits, compared to the mixtures of tars typically contained in real product gasses from gasification of biomass^{48, 96, 97}. It is worth noting that the sample operating with the clean simulated syngas (BC_syngas) operated for more than 1000 hours, at a higher current density, with an overall loss in the voltage of about 10%.

These observations are confirmed also by the evolution of the EIS spectra as function of time, as depicted in Figure 5.40.

In fact, the long term operation in aggravated conditions, in presence of the model tar, caused an important increase in the polarization resistance R_{pol} , resulting in a worsening of the overall performance.

Moreover, the recovery effect for the first 10 hours of operation is also observable from the drop of R_{int} , together with a slight increase of this parameter during the rest of the test.

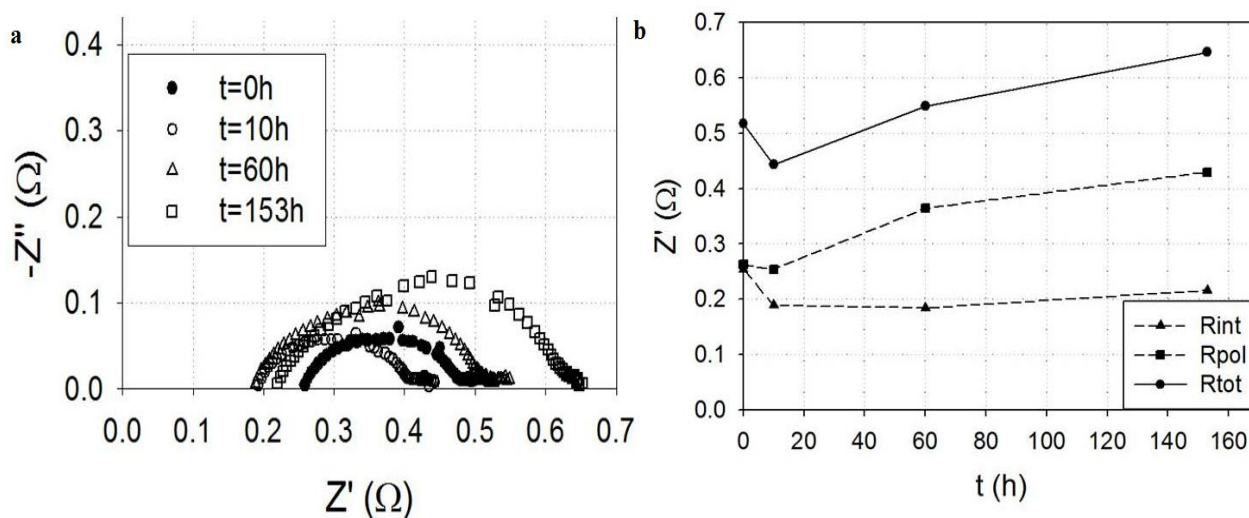


Figure 5.40. The EIS spectra, in Nyquist plots, are reported in figure (a). The spectra have been recorded in OCV condition, at $T=650^{\circ}\text{C}$ during the long-term test. In figure (b), the values of R_{int} , R_{pol} , and R_{tot} extracted from the experimental spectra, are plotted as a function of time in hours.

In order to deeply investigate the effect of the tar contaminant on the electrochemical processes, the EIS spectra were analyzed with the DRT method and the values of resistances related to each process were extracted from the experimental measurements by means of the CNLS fitting procedure described in the previous Sections, using the same ECM model.

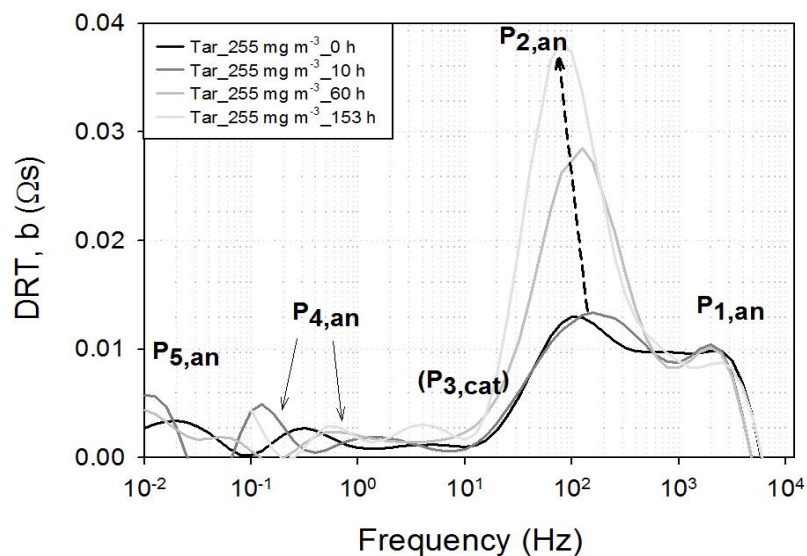


Figure 5.41. DRT functions obtained at different operating times during the long term exposure to toluene.

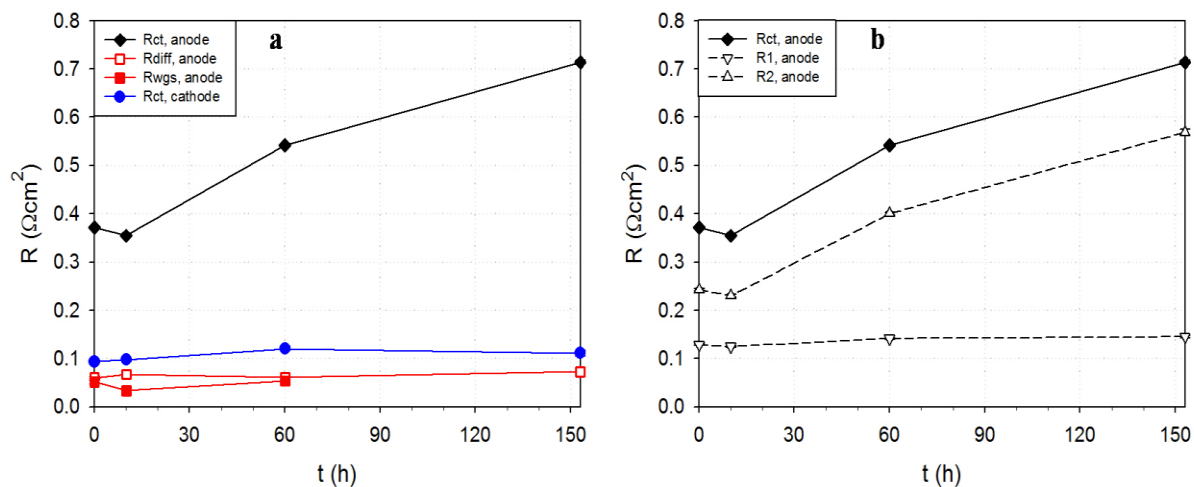


Figure 5.42. Polarization resistances of the button cell sample during the long-term exposure to toluene at 650°C. (a) Extrapolated resistances values for the operating processes within the cell; (b) charge transfer resistance at the anode resistances associated to its constituent processes P_1 and P_2 .

From both the DRT plots and the quantitative analysis of cell resistances, it appears clear that the sole process dramatically affected by the presence of tar is the anodic process P_2 related to the charge transfer mechanism involved in the fuel electrochemical oxidation, which is, as previously

mentioned, catalyzed by the Ni particle. As in the case of the endurance test in clean syngas, an increase of the impedance of this process may suggest a reduction in the kinetic of this reaction ascribable to a reduction of the catalytic effect of the Ni particle; in the case of the endurance test in clean syngas, it was demonstrated that this was caused by a diffusion of nickel particle from the anode functional layer towards the anode support, followed by Ni clustering, which effectively resulted in a reduction of the active surface of the TPB.

The post mortem analysis presented hereafter will shed light on the phenomena that caused the fast increase in the impedance of the charge transfer mechanism.

5.4.3. Post-mortem analysis

With the aim of investigating the effects caused by the presence of toluene in the fuel stream of the BC_tar operating under aggravated conditions (low T, low steam partial pressure), the sample has been extensively analyzed by means of a deep post-mortem characterization.

In this section, results coming from XRD analysis, Raman spectroscopy and SEM/EDS analysis are reported, along with the discussion of the results obtained.

XRD analysis

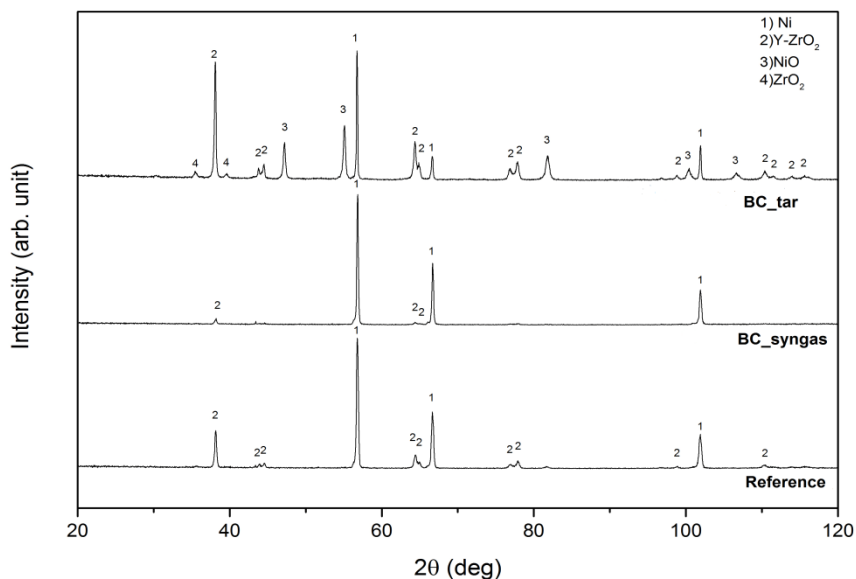


Figure 5.43. XRD spectra obtained from the anodes of BC_tar (top), BC_syngas (middle), and of a cell which has been only reduced under manufacturer conditions, taken as reference (bottom).

In Figure 5.43 are reported the results of the XRD analysis on the tested cells. As reference, a cell was reduced in the measurement housing. Phase identification was performed on collected patterns using the PDF-2 database as reference data ⁹⁸. After the reduction phase, peaks ascribable to the presence of Ni (JCPDS card n. 4-850) and tetragonal yttrium zirconium oxide (JCPDS card n. 48-224) are evident.

The sample exposed for 1000 hours in syngas atmosphere exhibits peaks ascribable to the same phases. It is noteworthy to observe that the intensity of the Y-ZrO₂ peaks is significantly reduced, suggesting that nickel segregation and densification at the surface has occurred.

The cell exposed for 150 hours in the tar contaminated syngas shows instead significant differences: beside the presence of Ni and Y-ZrO₂ phases, peaks ascribable to NiO (JCPDS card n. 47-1049) and monoclinic ZrO₂ (JCPDS card n. 37-1484) are evident, suggesting Zr oxide segregation from the mixed YSZ phase and Ni oxidation arose during the 150 hours experiment.

XRD results suggest that the re-oxidation of Ni to NiO and the phase segregation of ZrO₂ from YSZ are both phenomena related strictly to the presence of the model tar in the fuel stream, since the sample BC_syngas, which operated with the clean syngas in similar operating conditions as BC_tar for 1000 hours, does not show signs of these effects.

Raman spectroscopy

In order to confirm the XRD results Raman measurements were performed on the anode of the sample BC_tar. In Figure 5.44 the Raman spectra measured in the centre and near the boundary of the anode are reported, with assignments of relevant peaks. Raman spectra of YSZ ⁹⁹, ZrO₂ ¹⁰⁰, Y₂O₃ ¹⁰¹ and NiO ¹⁰² reported in the literature were used to assign the observed peaks. In the region below 800 cm⁻¹, data measured near the centre of the electrode show clear presence of pure ZrO₂ and possibly also of Y₂O₃ besides the YSZ phase. The wide band observed above 800 cm⁻¹ is assigned to nickel oxide. Differently, data measured near the electrode boundary show only the YSZ phase and a relatively weaker nickel oxide band. These results clearly confirm and strengthen what was suggested by the results obtained from the XRD analysis: the centre of the sample, which is the portion of the anode immediately in contact with the fuel stream, and thus where the local concentration of the tar contaminant is the highest, shows enhanced degradation effects, in terms of nickel oxidation and phase segregation of YSZ, compared to the edge of the

sample, where the gas diffuses from the centre through the anode porosity. The formation of these phases clearly explains the fast drop in cell performances, as they dramatically affect the charge transfer related to the fuel oxidation, due to the re-oxidation of the Ni catalyst. It is to mention, however, that the possible disruption of the anode porosity caused by the formation of NiO and segregation of ZrO₂ from the YSZ phase had no significant effect on the mass transport mechanisms (gas diffusion, water gas shift reaction) occurring within the cell.

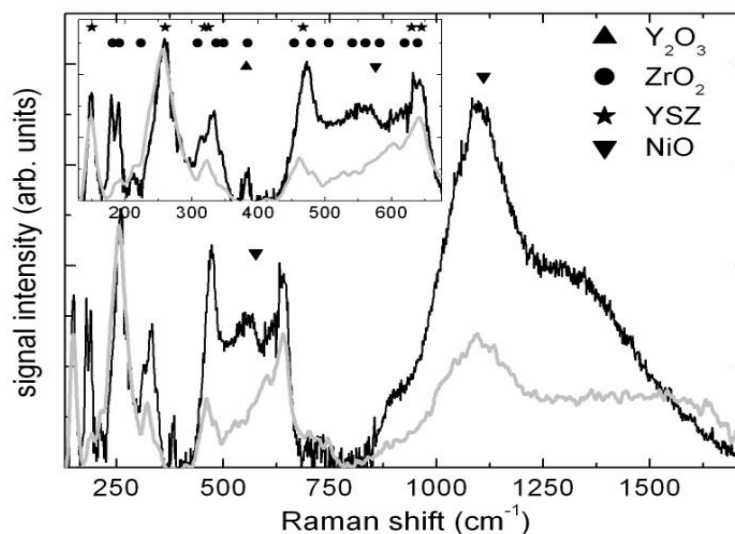


Figure 5.44. Raman spectra of anode material measured near the anode centre (black line) and at the anode boundary (grey line). Data were normalized at the 255 YSZ line. Inset: close up of the low-frequency region. Also shown the peak assignments as discussed in the text.

SEM/EDS analysis

In Figure 5.45 is reported a comparison between the cross sections of the reference sample (a), BC_syngas (b), and BC_tar (c). It can be observed that the only notable morphology change for the BC_syngas appears to be a densification of the structure on the anode surface (bottom part of the image), which is coherent with what was suggested by XRD results.

On the contrary, BC_tar shows profound morphological modifications, particles growth, pore size reduction and a generalized disordered structure, especially near the anode surface.

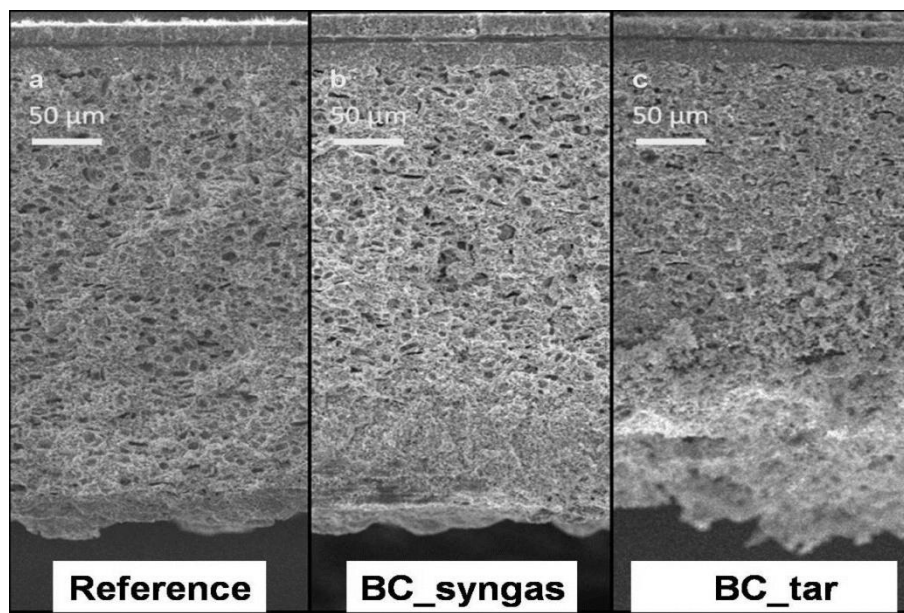


Figure 5.45. SEM images of the cross section of (a) the reference sample, (b) of the sample BC_syngas and (c) of the sample BC_tar.

Moreover, large carbon deposits were found to be distributed in proximity of the anode surface of the BC_tar sample: Figure 5.46 reports the SEM image of one of these carbon aggregates on the left side, while on the right side, a close-up of the carbon deposit is shown. An EDX analysis has been carried out on different spots located over the surface: the elementary composition, reported in Table 5.1, confirms the presence of carbon on the anode side.

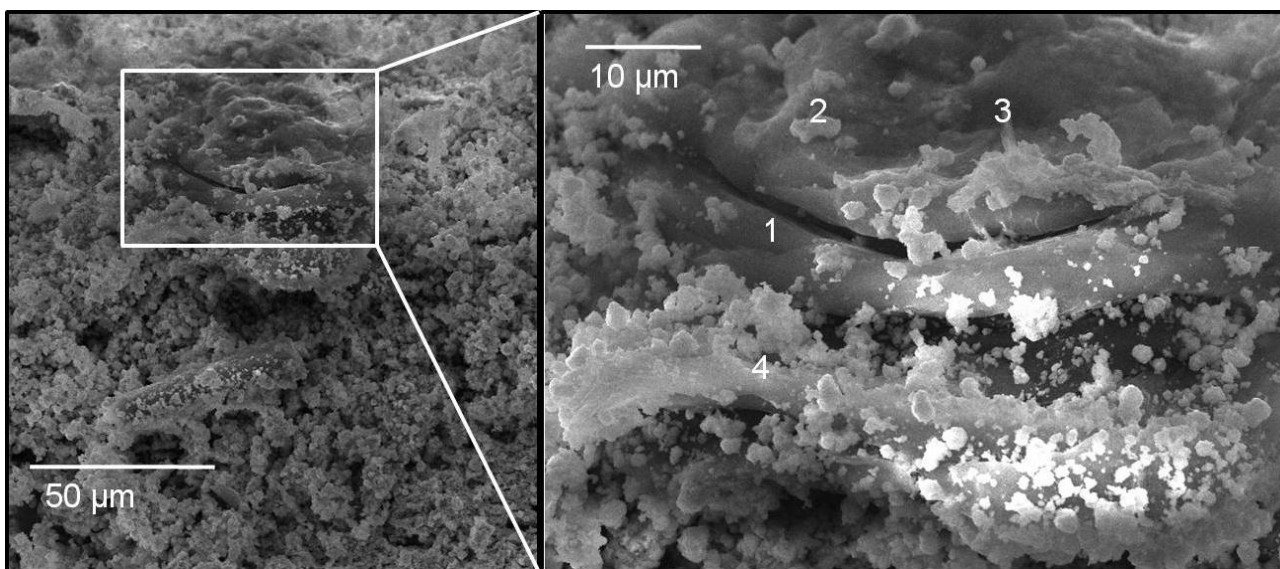


Figure 5.46. SEM image of a carbon deposit on the anode of BC_tar (left). Magnification of the carbon deposit (right); numbers indicate the spots where EDS analysis has been carried out, and the compositions obtained are reported in Table 4 below.

Elements	1 (wt%)	2 (wt%)	3 (wt%)	4 (wt%)
C	57.427	36.846	47.027	43.966
O	27.538	41.063	38.818	21.732
Ni	9.046	5.341	4.928	20.479
Y	0.211	0.712	0.567	0.621
Zr	5.383	15.134	8.261	12.600

Table 5.1. Elementary composition obtained from EDX analysis. Numbers refer to different spots located on the surface of the carbon aggregate, as shown in Figure 5.46.

5.4.4. Resume of tar contamination

Experimental results, obtained from *in-operando* electrochemical characterization and *post-mortem* analysis, highlight the formation of carbon deposits within the anode layer. As suggested

from the electrochemical behavior of the cell, this impedes an effective supply of H₂ to the active sites.

It is likely to suppose that an unbalanced accumulation of oxygen ions occurring in proximity of the clogged Ni particles may result locally in thermodynamical conditions favorable to nickel oxidation. This transformation is associated to significant volume expansion, and may cause uneven stresses propagation, possibly enhanced by carbon particles blocking pores and thus reducing voids, with the formation of cracks. The propagation of fractures results finally in the significant and widespread delamination phenomena observed with SEM analysis.

Nevertheless, in terms of operating processes, the disruption of the anode porous structure did not greatly affect the mass transport phenomena, while a dramatic increase in the anode charge transfer resistance was the result of Ni clustering and oxidation, which effectively caused the fast drop of the cell performances.

The presence of monoclinic zirconia phase suggests that significant mechanical stresses are built locally: it is well known that tetragonal-monoclinic phase transformation can occur in the yttrium stabilized zirconia systems as a result of stress application, in particular as consequence of cracks propagation¹⁰³. Similar behaviour is retained in composite materials with stabilized zirconia inclusions, as far as the tetragonal phase particles have been subjected to appropriate stresses¹⁰⁴. It is likely that the observed significant degradation phenomena are originated by local carbon deposition due to the presence of tar contaminants.

5.5. Reactions evolution on anode surface

In the main part of the experimental campaign reported so far in this work, the principal focus was to address a complete and in-depth characterization of the chemical and electrochemical processes occurring in an IT-SOFC cell when it is operated with a syngas fuel or part of it (H₂/H₂O and CO/CO₂ only). To do so, an advanced approach was presented to the electrochemical analysis involving a novel methodology for the deconvolution of the EIS spectra, the distribution of relaxation times method (DRT). It proved to be very instrumental in the identification of the processes, in the calculation of fundamental physicochemical quantities related to them, thanks to a synergic and systematic application of CNLS fitting of the experimental data with an ECM model based on the information obtained from the analysis of the

DRT plots at different operating conditions, and for the investigation of the degradation phenomena occurring in IT-SOFC samples coupled with clean syngas, or tar contaminated one.

Nevertheless, all the properties investigated so far by means of EIS/DRT/CNLS method are bulk properties; moreover, in order to simplify and generalize the results obtained from the electrochemical investigation, the samples tested were of reduced size (2 cm^2 active area), in order to ensure the homogeneity of the conditions, in terms of chemical and thermal gradients, on the tested samples.

Obviously, the real size of SOFC cells employed in power generating systems are at least 50 times larger than the sample analyzed with the DRT method in this work. For realistic cell dimensions, SOFC cells can experience significant performance degradation due to the concentration gradients over the anode where the fuel is diluted by its own reaction products during fuel cell operation. This causes a non-homogeneous distribution of the temperature and electrochemical performance, which penalizes the efficiency and durability of the fuel cell. Other surface effects, such as non homogeneous distribution of reactants, localized hot spots, deactivation of part of the cell due to the presence of contaminant in the fuel stream and so on, may drastically reduce the lifespan of realistic systems.

Thus, the access to experimental information coming directly from different spots on the anode surface of a cell results of crucial importance in order to optimize the operating condition experienced by the cell, in order to extend the durability of the entire system.

For this reason, in this work, the novel, in-house, multisampling set-up presented in Chapter 4 was employed to carry out an investigation about the progress of the reactions occurring in an IT-SOFC *in-operando* and in real time. IT-SOFC single cells of realistic dimensions were tested, as explained in Chapter 4, on both hydrogen and syngas fuel, coming from the external steam reforming of natural gas.

Thanks to the novel set-up, it was possible to perform concentration and temperature measurements with a spatial resolution, that allowed to obtain a complete thermo-chemical mapping of the operating cell.

Interesting information about the evolution of the processes along the anode surface were thus obtained in both cases; however, the main goal of this experimental investigation is to present the potentiality of this innovative investigating tool developed within this work.

5.5.1. Validation of the multisampling set-up

The first goal of this work is to evaluate the performance of this new set up comparing the polarization curve obtained from two cells of different size ($10 \times 10 \text{ cm}^2$ and $12 \times 12 \text{ cm}^2$), with those obtained from an Elcogen 15-cell stack, tested by a project partner, CUTEC, using the same operating condition, scaled for the testing of a single cell.

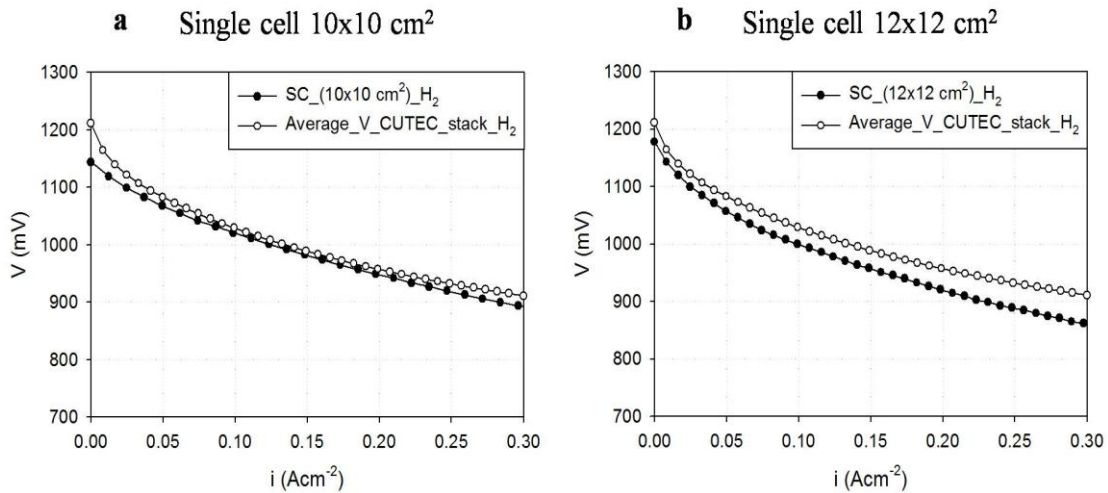


Figure 5.47. Performance comparison between tested single cells and 15-cell stack.

In the figure above (Figure 5.47.a) the comparison is shown between the polarization curves of the $10 \times 10 \text{ cm}^2$ single cell with the average i - V response obtained from the cells within the Elcogen's stack. It is evident from the plot that the curves are broadly similar, presenting very similar values of the voltage for most of the current densities applied. Only a slight difference in OCV value is evident. This result validates to some extent this set up, proving that the obtainable performances are globally good.

However, in the Figure 5.47.b, where the comparison with the $12 \times 12 \text{ cm}^2$ single cell is shown, the difference between the obtained curve and the reference one results more pronounced than that obtained in the case of the $10 \times 10 \text{ cm}^2$ cell. This evidence is however imputable to the enhanced ohmic resistance of the anodic current collectors, made of Crofer 22H stainless steel. In fact, the distance between the single cell curve and the reference coming from the Elcogen's

stack is more pronounced in the ohmic part of the polarization curve, where it can be appreciated that the slopes of the two curves, that are related to the ASR of the system, are different. This effect was caused by the previous experiments carried out on other samples in order to optimize the experimental set-up; the numerous exposures of the Crofer current collectors to high temperatures and ambient air probably caused the growth of a thin chromium oxide scale over its surface. Even if the chromium oxide possesses a good conductivity (compared to that of YSZ electrolytes) at high temperature (up to 750 °C), it decreases by more than one order of magnitude when the operating temperature is reduced to 650 °C.

Excluding the effect of the surface oxidation of the Crofer current collector, the novel set-up proved that the obtainable performances are globally good also for the 12x12 cm² cells.

5.5.2. Hydrogen operation

In this Section, the results obtained from the multisampling set-up employed in the study of an IT-SOFC single cell sample fed with dry H₂ are presented.

The composition and temperature distributions on the anodic surface are presented along 3 axes: the central horizontal axis of the cell, namely X axis, the vertical axis close to the anodic inlet and the vertical axis close to the anodic outlet, namely Y axis and Y' axis respectively. Every graph shown in this work has a sampling point map on the top to show the position of the sampling points to which the graph itself is referred.

Figures 5.48.a, 5.48.b and 5.48.c represent the gas composition analysis, in OCV and under a current load of 30 A, obtained from the spots along the X, Y, and Y' axis respectively.

Figures 5.48.d, 5.48.e and 5.48.f represent the values of the temperature obtained during the stabilization of cell conditions under a constant current load of 30 A. Since in OCV condition, for hydrogen operation, no reactions occur, the temperature profiles recorded showed no significant result, and are not presented.

Comparing plots 5.48.a, 5.48.b and 5.48.c, it is evident that the chemical gradient variation is more significant along the X axis compared to the vertical ones; for this reason all the assessments are referred to X axis (Figure 4a). The only information that can be deduced from plots 5.48.b and 5.48.c is that along the Y and Y' axis the gas composition results quite homogeneous, suggesting a uniform distribution of the species perpendicularly to the flow direction.

In OCV conditions, the composition is the same in all the sampling points, so the chemical gradient inside the cell can be considered negligible. Since N_2 is an inert gas, its molar fraction remains unaltered under current respect to the OCV condition. Instead, when current flows through the cell, there is a gradual decrease of H_2 along the X axis, corresponding to the increase of the molar fraction of H_2O , due to the electrochemical oxidation reaction of the hydrogen shown below.



The presence of this exothermic reaction is confirmed by the temperature analysis shown in Figure 5.48.d, where it is possible to observe a general increase of temperature going from the inlet to the outlet of the cell. In the first 300 seconds, in which the current was increased from OCV up to 30 A, the increment is more pronounced and rapid for the thermocouples located close to the inlet, as evident from the steepness of the inflection located at approximately 300 s. Moreover during the equilibrium time it is possible to observe that the increment of temperature in the sampling point located close to the anodic inlet (Y axis) is greater than the increment of those located close to the anodic outlet (Y' axis). In this phenomenon plays an important role the depletion of H_2 in the part close to the anodic outlet, due to the evolution of the electrochemical oxidation reaction.

In fact, in the zones close to the outlet of the cell, the increase of the reaction product (H_2O) causes a decrease of the Nernst potential (Equation 5.31) and, considering the cell voltage as the difference between the Nernst potential and the voltage drop caused by the whole resistance of the cell (Equation 5.30), the local current density results lower with respect to that distributed closest to the inlet.

$$V_{cell} = E_n - ir \quad (5.30)$$

$$E_n = E_0 + \frac{RT}{nF} \ln \frac{p[C]^c p[D]^d}{p[A]^a p[B]^b} \quad (5.31)$$

In Equations 5.30 and 5.31 V_{cell} is the cell voltage in V (constant), E_n is the Nernst potential in V, i is the current in A, r is the cell resistance in Ω , E_0 is the standard reduction potential in V, R is

the ideal gas constant, T is the temperature in K, n is the number of electrons, and p are the partial pressures of gas species for the general reaction $aA + bB \rightarrow cC + dD$.

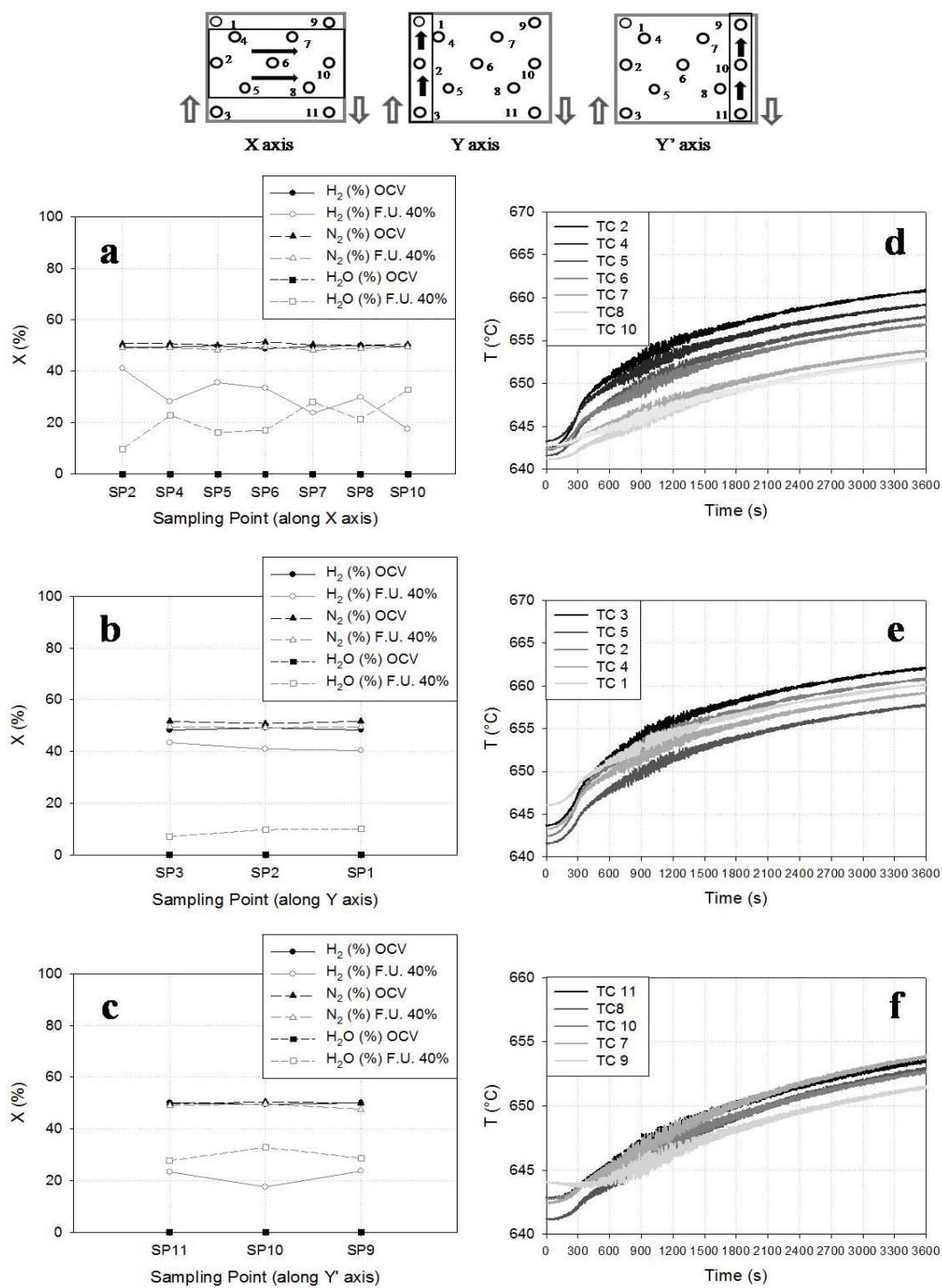


Figure 5.48. Composition (a, b, c) and temperature (d, e, f) analysis along the axes.

This decrease of the current density in the anodic outlet part is probably the cause of the decrease of the temperature measured. This non homogeneous distribution of the current density inside the cell has also been verified in another work by DLR (Deutsches Zentrum für Luftund Raumfahrt) with a different experimental apparatus. In their work the local behaviour of current and voltage in a segmented cell was studied, highlighting a considerable variation of current density for different cell segments. In particular, for the segment located close to the fuel outlet, the current density results lower than the current density of segment located at the fuel inlet¹⁰⁵.

5.5.3. Syngas operation

In this Section, the results are presented obtained from the multisampling set-up employed in the study of an IT-SOFC single cell sample fed with a syngas. The simulated syngas fuel represents a nominal composition that may result from the steam reforming of the natural gas.

In Figure 5.49 there are reported the results of the gas analysis carried on the sampling spots located on the Y axis (Figures a, b and c) and on the Y' axis (Figures d, e, and f). Figures 5.49.a and 5.49.d refer to the gas sampling performed in OCV conditions. Figures 5.49.b and 5.49.e refers to the gas sampling carried out under a current of 15 A (corresponding to a Fuel Utilization of the 20 %) flowing through the cell. Figures 5.49.c and 5.49.f reports the results of the gas sampling performed while the cell was producing a current of 30 A (corresponding to a Fuel Utilization of the 40 %).

If the plots reported in Figure 5.49 are compared in couples (a with d, b with e and c with f), the gas sampling depicts the initial and final phase of the reaction developing along the gas flow through the anode surface.

However, in all the plots it is confirmed the homogeneous distribution of the gas species, thus confirming again a uniform distribution of the species perpendicularly to the flow direction.

Starting from the OCV measurements, it is evident that from the beginning to the end of the cell, there is an important production of H₂ and CO and a concomitant consumption of CH₄ and H₂O. The CO₂ content remains almost unaltered.

A similar behaviour is also observable in the case of 15 A of current (F.U. 20%): even if the cell is consuming H₂ to produce the current, an increase in H₂ content is still observable. Being the product of the H₂ electrochemical oxidation, the H₂O content in the anode mixture slightly increases at the end over the anode length. Again, CH₄ is consumed exactly as it happened in the

OCV case, while the production of CO appears reduced with respect to the case with no current. This time, a slight increase in the CO₂ molar fraction is observed in proximity of the anode outlet. Considering the case of 30 A, the H₂ expected consumption is observable, but still restrained respect to what expected from a fuel utilization of 40 %; nevertheless, along with the same consumption of CH₄, this time also the CO content seems to reduce. A net increase in both H₂O and CO₂ is now evident.

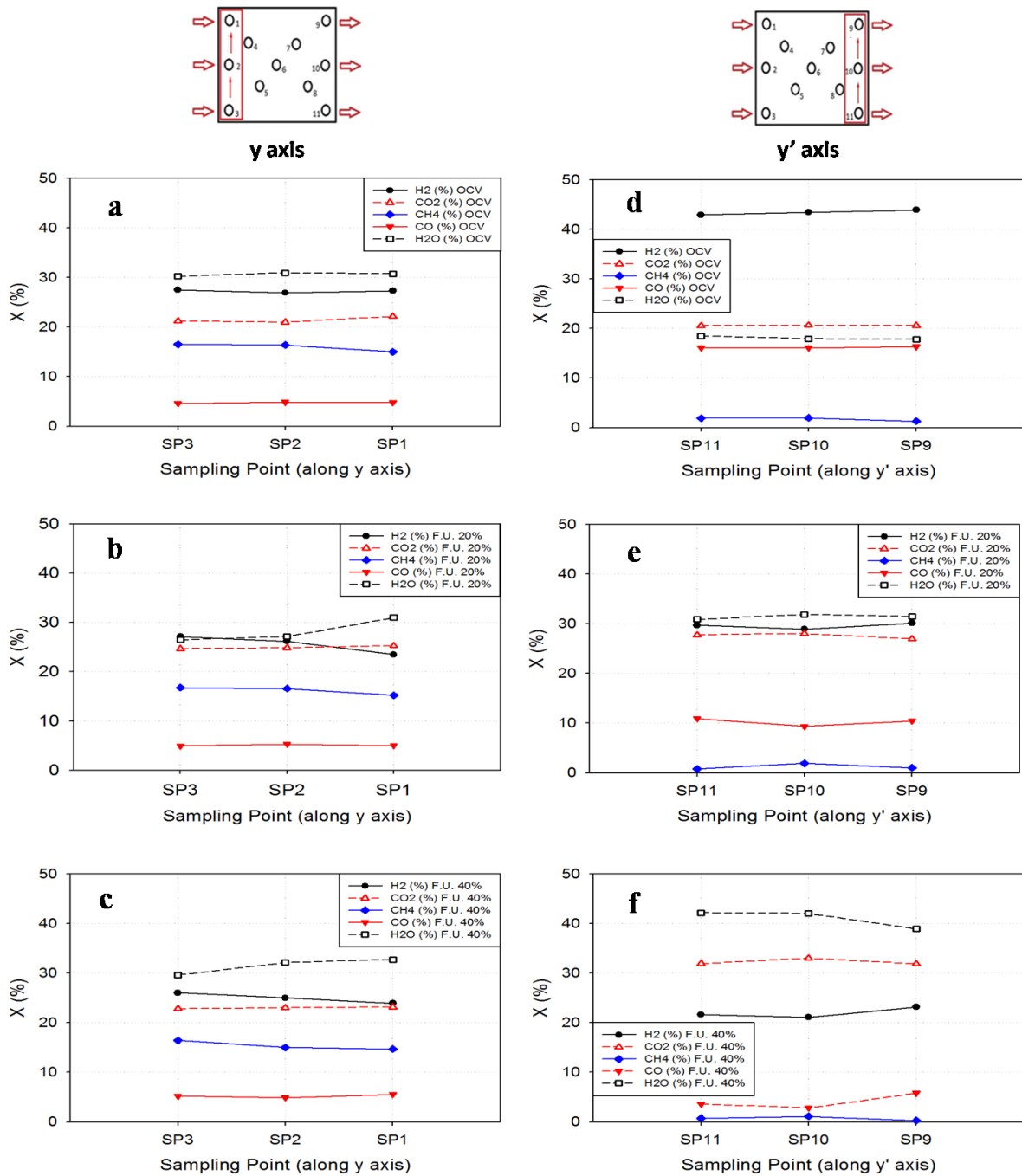


Figure 5.49. Gas composition analysis along the Y axis (a, b, c) and Y' axis (d, e, f) in OCV (a, d), under a constant current of 15 A (b, e) and under a constant current of 30 A (c, f).

These results suggest that there are 3 different reactions driving the local concentration gradients along the anode surface: the electrochemical oxidation of H₂, the methane steam reforming reaction (MSR) and the water gas shift reaction (WGS).

A clearer picture of what is occurring in each of the case studied can be obtained from the analysis of the gas compositions along the X axis (parallel to the gas flow field), and from the temperature analysis reported hereafter.

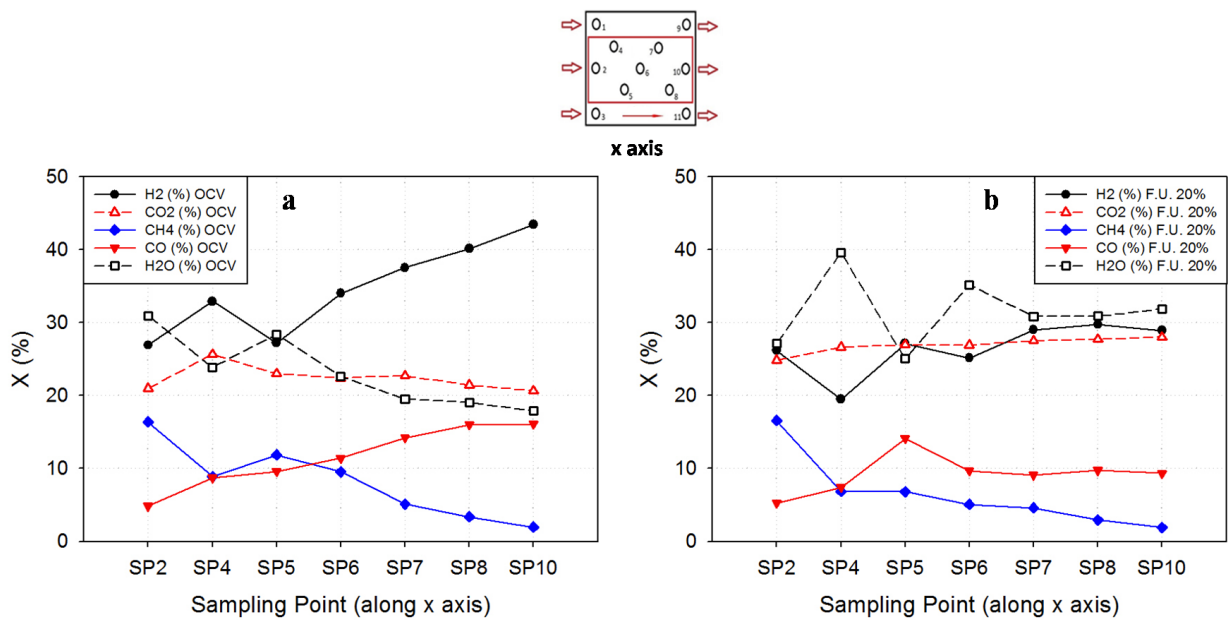


Figure 5.50. Gas composition analysis along the X axis in OCV (a) and under a constant current of 15 A (b).

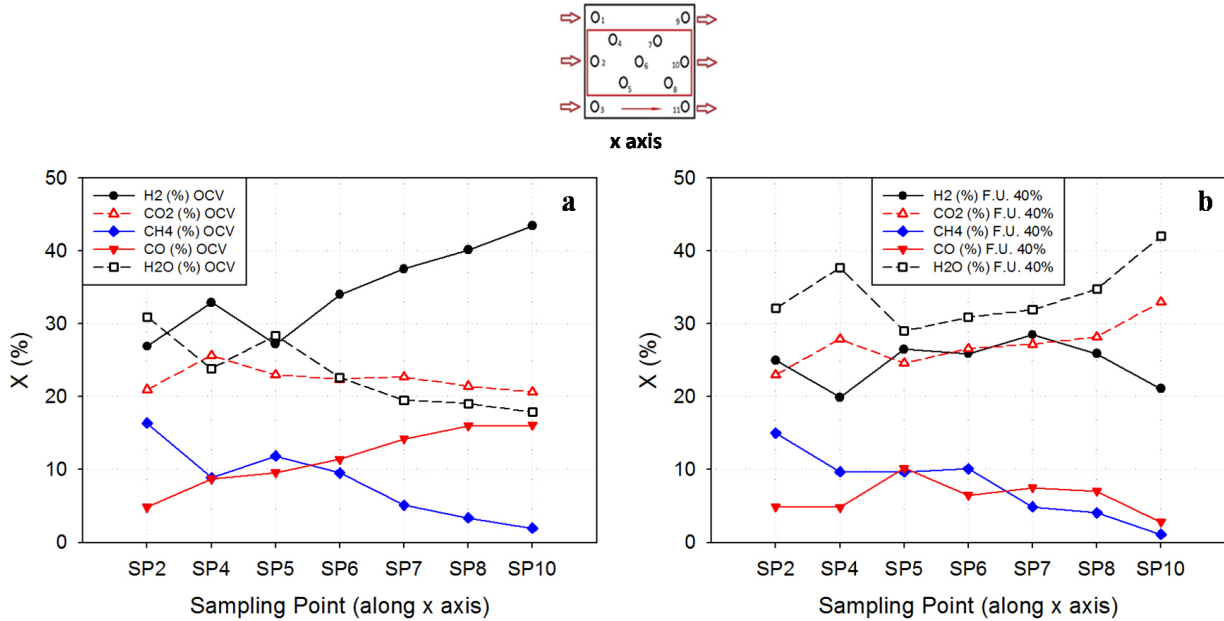


Figure 5.51. Gas composition analysis along the X axis in OCV (a) and under a constant current of 30 A (b).

Observing the trend of the compositions along the gas flow field direction, a number of considerations arise.

At OCV conditions it can be clearly seen that the evolution of the gas composition must be ascribed to the sole effect of the methane steam reforming reaction (MSR) which progressively consumes water and methane, to produce hydrogen and carbon monoxide. The constant value of CO₂, which is a product of the water gas shift reaction, implies that this process is not occurring or is at a very low degree of progress.

At 15 A, while the MSR reaction seems not affected by the current flow, the degree of progress of the WGS reaction start to increase, as demonstrated from the progressive increase of the CO₂ and the reduced increase in the CO content. Hydrogen is consumed and water is now produced as a reflection of the electrochemical oxidation reaction, but the H₂ consumed is rapidly restored from the occurrence of both MSR and WGS reactions; as a result H₂ slightly increases along the flow field direction.

At 30 A the driving process is clearly the electrochemical oxidation of H₂, as proven from the net increase in the H₂O content. However, even if the current density is high, the consumption of H₂ results still mitigated; even though the MSR reaction appears again unaffected from the increase

of the current density, the WGS reaction is strongly pushed towards a higher degree of progress, as confirmed from the trend of CO₂.

It is to be noted that in both cases under constant current, the electrochemical oxidation of CO can be excluded, due to the results obtained from the in-depth electrochemical investigation presented for the button cell samples (EIS/DRT analysis).

To further confirm what is stated above, Figure 5.51. reports the temperature analysis at OCV (Figures a, b, and c) and at 30 A (Figures d, e, and f).

Observing the temperature profile in OCV conditions, all the thermocouples show a reduction in the measured temperature during the 3600 seconds of stabilization of the syngas composition. This implies that the dominant reaction is the MSR reaction, which is the only process to be strongly endothermic ($-\Delta H^0_{298} = -206 \frac{kJ}{mol}$). Some temperature steps can be observed, especially from the thermocouples located in the spots in proximity to the anode inlet, which may be the manifestation of the dynamic re-equilibration of the WGS reaction caused by the evolution of the dominating MSR reaction.

When the cell is producing 30 A of current, the temperature profile is completely the opposite, denoting that the dominant reaction is, this time, the electrochemical oxidation of H₂, which is strongly exothermic. Moreover, it can be again observed that the temperature in proximity of the outlet of the cell is notably lower than that measured at the beginning, exactly as in the case presented for the H₂ fuel: again, this must be the effect of the depletion of the fuel (or its dilution in its products) which locally decreases the current density, and thus decreasing also the temperature. Some fluctuation are again measured, maybe caused by the dynamic equilibria of both WGS and MSR reactions.

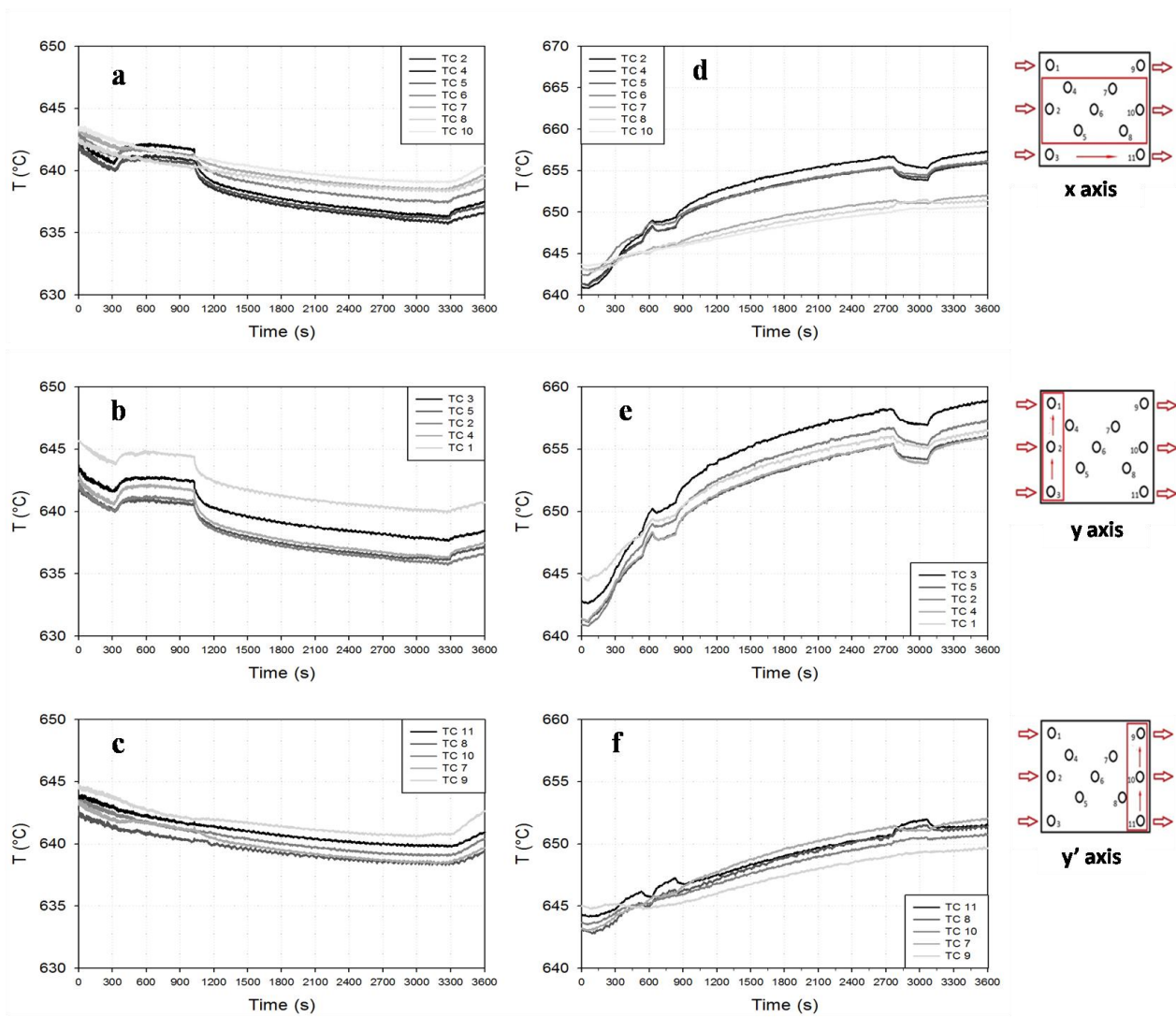


Figure 5.51. Temperature analysis at OCV (a, b, c) and under a constant current of 30 A (d, e, f).

5.5.4. Resume of the reactions evolution on anode surface

The novel multisampling set-up proved that good performances are obtainable from cells tested with it.

By means of spatially resolved sampling of both gas concentrations and temperature it has been possible to deeply study the course of the reaction *in operando*.

From the study in dry hydrogen fuel, it was observed how the sole electrochemical oxidation reaction evolves along the anode surface. Its occurrence causes an increase in the cell temperature

due to its exothermic nature, but the depletion of the fuel, and its dilution in its product along the gas flow field direction, causes a cooling effect towards the proximity of the anode outlet, which is probably related to the reduction of the local current density.

In the case of the syngas fuel, it was observed how, depending on the current generated from the cell, the three principal reactions, namely the electrochemical oxidation of H_2 , the methane steam reforming (MSR) and the water gas shift (WGS) reactions affect the concentration and the thermal gradients.

In OCV conditions, the MSR reaction dominates the concentration and thermal profile of the anode, while the WGS reaction appears to be almost in equilibrium. At high current (30 A), the electrochemical oxidation of H_2 is the preponderant reaction, and both the MSR and the WGS (the latter being this time at a higher degree of progress) provide further H_2 for the electrochemical reaction, resulting in a net reduced consumption of the fuel. At 15 A, the situation is a combination of the two, resulting in a slight production of H_2 even if the cell is producing current. The thermal profile shifts from a the cooling effect of the endothermic MSR reaction at OCV to the heating effect related to the exothermic oxidation reaction.

This profound analysis of the processes may result very instrumental for the optimization of the operating conditions when IT-SOFC based systems are coupled with syngas sources, allowing to study the best conditions for co-generative and tri-generative application, or to reduce the occurrence of degradation phenomena such as carbon deposition, and it will also provide precious information for the build-up of reliable predicting 2D computational models based and validated on experimentally available thermo-chemical mapping of the cell.

6. CONCLUSIONS

Fuel flexibility is one of the most interesting features of SOFCs systems, especially to achieve first entry of this technology into the market of heat and power generating systems.

Thanks to the high operating temperatures and to the presence of catalytic nickel particles, this type of electrochemical devices can produce power starting from syngas fuels, such as those produced from the reforming of natural gas or from the gasification of coal and biomasses, with a very high conversion efficiency.

Nevertheless, if the next generation of solid oxide fuel cells aims to achieve a sensible cost reduction and enhanced life-span of the systems by decreasing the operating temperature, the possibility of the convenient integration of syngas sources with IT-SOFC-based systems needs to be verified starting from a profound knowledge of the single chemical and electrochemical processes that affect the final performances of the system.

The simultaneous occurrence of a large number of phenomena that can positively or negatively affect the performances of syngas-fed SOFC systems, demands innovative investigation tools able to distinguish and deeply analyze the nature and the evolution of the reactions, in order to establish the best conditions for safe, reliable, and effective energy production.

For these reasons, in this work it has been presented a profound characterization of the processes related to the operation of IT-SOFC samples fed with simulated syngas.

The experimental campaigns has been divided in two main parts. The first one was aimed to identify the number, the nature and the evolution of the different physicochemical processes and to extrapolate useful physical quantities related to the fundamental equations regulating each type of phenomena from experimental data. The second one was aimed to study the thermal and chemical gradients generating along the anode surface due to the different evolution of both chemical and electrochemical equilibria at different operating conditions. In both cases, novel tools of analysis were specifically employed to study these phenomena.

In the first part of the experimental work, the distributed relaxation times (DRT) method was performed on the experimental EIS spectra obtained from several button cell samples fed with

three different fuel mixtures: H₂-H₂O, CO-CO₂ and simulated syngas. From the variation of a single operating parameter each time, the observed response of DRT peaks was ascribed to different electrochemical processes occurring at the anode or at the cathode side.

Up to six different processes were identified. The high-frequency processes P₁ and P₂ were both ascribed to the electrochemical oxidation of the fuel occurring at the anode side, due to their prominent dependency on the operating temperature, and being modestly influenced by the fuel composition. In particular, process P₁ is related to the transport of O²⁻ ions within the YSZ matrix of the anode functional layer. Process P₂ is in turn identified with the charge transfer mechanism of the electrochemical oxidation of the fuel occurring within the anode functional layer, in the three phase boundary (TPB) region.

Even though the process P₃ resulted often convoluted with the anodic process P₂, it was successfully ascribed to the charge transfer mechanism for the reduction of O₂ to O²⁻ at the cathode side, due to its thermal activation behavior, independency on the fuel composition and being slightly affected by the O₂ content in the cathode stream.

The evident dependency on the composition of the fuel gas and the relatively low or null sensitivity to temperature variations for process P₄ suggest that this process is associated to gas diffusion through the open porosity of the anode substrate.

Process P₅ appears only when the sample is fed with a syngas mixture. It is clearly affected by a change in the molar fractions of the fuel, and barely influenced by temperature variation: it has been thus attributed to the water gas shift reaction (WGS).

Finally, process P₆ in the lowest frequency region can be associated to the diffusion of the cathodic gas in the MIEC porous structure.

By the application of the synergic approach of *in-operando* impedance spectroscopy measurements under a wide number of different and pre-defined operating conditions, the DRT method, and CNLS fitting of the experimental EIS measurements with an equivalent circuit model defined from the identification of the processes, it was possible to estimate activation energies, reaction orders, pre-exponential factors and effective diffusion coefficients for the three fuels tested: H₂/H₂O, CO/CO₂ and syngas.

Comparing the obtained results in this work in the three cases between them, and with what has been reported from other authors in literature, it was possible to hypothesize that in the case of a syngas fuel, the oxidation mechanism of the fuel is similar to that occurring in the case of humidified hydrogen, suggesting that H₂ is preferentially oxidized at the anode side. The carbon

monoxide is rather involved in the Water Gas Shift reaction, in order to produce more H₂ to be further oxidized; this evidence resulted strongly supported in literature.

The same methodology was then applied to study the evolution of the identified processes during a long term operation of the samples in clean syngas, and in a syngas contaminated with the presence of tar species, which is known to be one of the most harmful class of species contained in the syngas produced by gasification systems.

The results of the DRT/CNLS fitting approach showed, in the case of the long term test (1000 hours) with clean syngas, that the processes being most affected from this endurance test were the anodic process P₂ and the cathodic process P₃, followed by a minor increase of the other low frequency anodic processes P₄ and P₅. By means of a post mortem characterization, it was observed a depletion of Ni particles from the AFL and a subsequent migration and densification to the bottom part of the anode supporting layer, explaining the increase of the contribution of the anodic processes to the overall impedance of the cell, while the observed slow down of the kinetics for the cathodic electrochemical reaction was ascribed to the depletion of the Sr content in the cathode layer.

In the case of tar contamination, experimental results, obtained from *in operando* electrochemical characterization and *post-mortem* analysis, highlight the formation of carbon deposits within the anode layer. As suggested from the electrochemical behavior of the cell, this impedes an effective supply of H₂ to the active sites.

It was supposed that an unbalanced accumulation of oxygen ions occurring in proximity of the clogged Ni particles may result locally in thermodynamical conditions favorable to nickel oxidation. This transformation is associated to significant volume expansion, and may cause uneven stresses propagation, possibly enhanced by carbon particles blocking pores and thus reducing voids, with the formation of cracks. The presence of a tar contaminant, even in low quantities, in the fuel stream of an IT-SOFC cell resulted in a dramatic drop of the cell's performances, which underwent to a failure within approximately 150 hours.

In the second part of the experimental investigations, the novel multisampling set-up developed in this work proved that good performances are obtainable from cells tested with it.

By means of spatially resolved sampling of both gas concentrations and temperature it was possible to deeply study the course of the reaction *in operando*.

From the study in dry hydrogen fuel, it was observed how the electrochemical oxidation reaction causes an increase in the cell temperature due to its exothermic nature; but the depletion of the fuel, and its dilution in its product along the gas flow field direction, causes a cooling effect towards the proximity of the anode outlet, which is probably related to the reduction of the local current density.

In the case of the syngas fuel, it was observed how, depending on the current generated from the cell, the three principal reactions, namely the electrochemical oxidation of H_2 , the methane steam reforming (MSR) and the water gas shift (WGS) reactions affect the concentration and the thermal gradients.

In OCV conditions, the MSR reaction dominates the concentration and thermal profile of the anode, while the WGS reaction appears to be almost in equilibrium condition. At high current (30 A), the electrochemical oxidation of H_2 is the preponderant reaction, and both the MSR and the WGS (the latter being this time at a higher degree of progress) provides further H_2 for the electrochemical reaction, resulting in a net reduced consumption of the fuel. At 15 A, the situation is a combination of the two, resulting in a slight production of H_2 even if the cell is producing current. The thermal profile shifts from a the cooling effect of the endothermic MSR reaction at OCV to the heating effect related to the exothermic oxidation reaction.

This profound analysis of SOFC processes, by means of the EIS/DRT/CNLS synergic approach for the electrochemical bulk properties and by means of the novel multisampling set up for the investigation of thermochemical gradients and surface evolution of the reactions, may result very instrumental for the optimization of the operating conditions when IT-SOFC based systems are coupled with syngas sources, allowing to study and assess the best condition for co-generative and tri-generative application, or to reduce the occurrence of degradation phenomena such as the carbon deposition, and it will also provide precious information for the build-up of reliable predicting 2D computational models based on and validated by experimentally available thermochemical mapping of the cell.

PUBLICATIONS

- D. Pumiglia, S. Vaccaro, A. Masi, S. J. McPhail, M. Falconieri, S. Gagliardi, L. Della Seta, M. Carlini, “Aggravated test of Intermediate temperature solid oxide fuel cells fed with tar-contaminated syngas” *Journal of Power Sources* 340 (2017) 150-159.
- D. Pumiglia, F. Santoni, E. Viceconti, B. Conti, C. Boigues Muñoz, B. Bosio, M. Carlini, S. J. McPhail, “SOFC Anode Process Characterization by Means of a Spot-Sampling Set-up for in-Operando Gas Analysis”, *ECS Transaction*, *Accepted*.
- C. Boigues Muñoz, D. Pumiglia, S. J. McPhail, D. Montinaro, G. Comodi, G. Santori, M. Carlini, F. Polonara: “More accurate macro-models of solid oxide fuel cells through electrochemical and microstructural parameter estimation e Part I: Experimentation”, *Journal of Power Sources* 294 (2015) 658-668.
- C. Boigues-Muñoz, D. Pumiglia, S. J. McPhail, G. Santori, D. Montinaro, G. Comodi, M. Carlini, F. Polonara, “More accurate macro-models of solid oxide fuel cells through electrochemical and microstructural parameter estimation e Part II: Parameter estimation”, *Journal of Power Sources* 286 (2015) 321-329.
- A. Mehmeti, S. J. McPhail, D. Pumiglia, M. Carlini, “Life cycle sustainability of solid oxide fuel cells: From methodological aspects to system implications”, *Journal of Power Sources* 325 (2016) 772-785.
- C. Boigues-Muñoz, D. Pumiglia, F. Santoni, S. J. McPhail, G. Comodi, M. Carlini, “Performance Degradation Prediction of a Low-Temperature SOFC via Impedance Spectroscopy and CFD Modelling”, *ECS Transaction*, 68 (1) (2015) 2227-2235.
- A. Masi, M. Bellusci, M. Carlini, S. J. McPhail, D. Pumiglia, P. Reale, A. Rinaldi, F. Padella, “Protective Coating from Manganese Cobalt Oxide Powders Obtained by High Energy Ball Milling: Materials Characterization and Cell Environment Testing”, *ECS Transactions*, 68 (1) (2015) 2671-2678.
- A. Masi, S. Frangini, D. Pumiglia, L. Della Seta, A. Masci, S. J. McPhail, M. Carlini, “LaFeO₃ perovskite conversion coatings grown on a 13Cr ferritic stainless steel: a corrosion degradation study in simulated solid oxide fuel cell (SOFC) interconnect conditions at 700 °C”, *Materials and Corrosion* (2016), *In Press*.
- A. Masi, S. Frangini, L. Della Seta, S. McPhail, D. Pumiglia, M. Carlini, “Composite Cu-LaFeO₃ Coating on High Cr Ferritic Stainless Steels for IT-SOFC Interconnects”, *ECS Transaction*, *Accepted*.

BIBLIOGRAPHY

-
- [1] IPCC: special report on carbon capture and storage (SRCCS), 2005
- [2] EU: the 2020 climate and energy package, the European Commission, 2014.
- [3] A. Boudghene Stambouli, E. Traversa, Solid oxide fuel cells (SOFCs): a review of an environmentally clean and efficient source of energy, *Renewable and Sustainable Energy Reviews* 6 (2002) 433–455.
- [4] S.J. McPhail, L. Leto, C. Boigues-Munoz, *The Yellow Pages of SOFC Technology, International Status of SOFC Deployment* (2013). Report IEA, Annex 24.
- [5] O'Hayre RP, Cha S-W, Colella W, Prinz FB. *Fuel cell fundamentals*. New York: John Wiley & Sons (2006) 290-292.
- [6] V. Cigolotti, S. McPhail, A. Moreno, Nonconventional fuels for high-temperature fuel cells: status and issues, *Journal of Fuel Cell Science and Technology* 6 (2009) 021311-1- 021311-8.
- [7] S. J. McPhail, V. Cigolotti, A. Moreno, *Fuel Cells in the Waste-to-Energy Chain – Distributed Generation Through Non-Conventional Fuels and Fuel Cells*, Springer (2012).
- [8] P. Holtappels, S. Steinberger-Wilckens, Realising reliable, durable energy efficient and cost effective SOFC systems (Real-SOFC), *Fuel Cells* 9 (6) (2009) 783-784.
- [9] S. C. Singhal and K. Kendall, editors. *High temperature solid oxide fuel cells: fundamentals, design, and applications*. Elsevier Advanced Technology, Oxford, UK, 1. edition, (2003).
- [10] EG&G Technical Services, Inc., *Fuel Cell Handbook*, 7th Edition, U.S. Department of Energy Office of Fossil Energy National Energy Technology Laboratory, (2006).
- [11] J. Larminie, A. Dicks, *Fuel Cell Systems Explained*, 2nd Edition, Wiley (2003).
- [12] I. R. Gibson, G. P. Dransfield, J. T. S. Irvine, Sinterability of commercial 8 mol% yttria-stabilized zirconia powders and the effect of sintered density on the ionic conductivity, *Journal of Materials Science* 33 (1998) 4297-4305.
- [13] S. P. S. Badwal, Zirconia-based solid electrolytes: microstructure, stability and ionic conductivity, *Solid State Ionics* 52 (1992) 23-32.
- [14] O. Yamamoto, Y. Arati, Y. Takeda, N. Imanishi, Y. Mizutani, M. Kawai, Y. Nakamura, Electrical conductivity of stabilized zirconia with ytterbia and scandia, *Solid State Ionics* 79 (1995) 137-142.
- [15] S. P. S. Badwal, F.T. Ciacchi, D. Milosevic, Scandia–zirconia electrolytes for intermediate temperature solid oxide fuel cell operation, *Solid State Ionics* 136–137 (2000) 91–99.
- [16] H. Inaba, H. Tagawa, Ceria-based solid electrolytes, *Solid State Ionics* 83 (1996) 1- 16.
- [17] M. Mogensen, N. M. Sammes, G. A. Tompsett, Physical, chemical and electrochemical properties of pure and doped ceria, *Solid State Ionics* 129 (2000) 63–94.
- [18] S. P. Jiang, S. H. Chan, A review of anode materials development in solid oxide fuel cells, *Journal of Materials Science* 39 (2004) 4405 – 4439.
- [19] O. A. Marina, C. Bagger, S. Primdahl, M. Mogensen, A solid oxide fuel cell with a gadolinia-doped ceria anode: preparation and performance, *Solid State Ionics* 123 (1999) 199–208.
- [20] M. Mogensen, T. Lindegaard, U. R. Hansen, Physical Properties of Mixed Conductor Solid Oxide Fuel Cell Anodes of Doped CeO₂, *Journal of Electrochemical Society* 141 (8) (1994) 2122-2128.
- [21] S. P. Jiang, Development of lanthanum strontium manganite perovskite cathode materials of solid oxide fuel cells: a review, *Journal of Materials Science* 43 (2008) 6799–6833.
- [22] O. Yamamoto, Y. Takeda, R. Kanno, M. Noda, Perovskite-type oxides as oxygen electrodes for High Temperature Oxide Fuel Cells, *Solid State Ionics* 22 (1987) 241-246.
- [23] J. W. Stevenson, I. It Armstrong, R. D. Carneim, L It Pederson, and W. J. Weber, Electrochemical Properties of Mixed Conducting Perovskites La_{1-x}M_xCo_{1-y}Fe_yO_{3-δ} (M = Sr, Ba, Ca), *Journal of Electrochemical Society* 143 (9) (1996) 2722-2729.
- [24] A. Aarva, S. J. McPhail, A. Moreno. "From energy policies to active components in solid oxide fuel cells: state-of-the-art and the way ahead." *ECS Transactions* 25.2 (2009): 313-322.
- [25] S.P. Jiang, X. Chen. Chromium deposition and poisoning of cathodes of solid oxide fuel cells – A review, *International Journal of Hydrogen Energy* 39 (2014) 505-531.
- [26] W.Z. Zhu, S.C. Deevi, Opportunity of metallic interconnects for solid oxide fuel cells: a status on contact resistance, *Materials Research Bulletin* 38 (2003) 957–972.

-
- [27] V. A. C Haanappel, V. Shemet, I. C. Vinke, S. M. Groß, T. Koppitz, N. H. Menzler, M. Zahid, W. J. Quadackers, Evaluation of the suitability of various glass sealant—alloy combinations under SOFC stack conditions, *Journal of Materials Science* 40 (2005) 1583-1592.
- [28] N. Lahl, K. Singh, L. Singheiser, K. Hilpert, D. Bahadur, Crystallisation kinetics in AO-Al₂O₃-SiO₂-B₂O₃ glasses (A = Ba, Ca, Mg), *Journal of Materials Science* 35 (2000) 3089-3096.
- [29] Y. S. Chou, J. W. Stevenson, L. A. Chick, Ultra-low leak of hybrid compressive mica seals for solid oxide fuel cells, *Journal of Power Sources* 112 (2002) 130-136.
- [30] J. T. S. Irvine, P. Connor, *Solid Oxide Fuels Cells: Facts and Figures*, Springer, (2013).
- [31] M.C. Tucker, Progress in metal-supported solid oxide fuel cells: A review, *Journal of Power Sources* 195 (15) (2010) 4570-4582.
- [32] B. C. H. Steele. Fuel-cell technology: Running on natural gas. *Nature* 400 (1999) 619–620.
- [33] J. Jewulski, M. Stepien, M. Blesznowski, K. Gallucci, D. Barisano, Biomass gasification and syngas production for the use in solid oxide fuel cells: gas clearing and conditioning, and performance tests, 20th European Biomass Conference and Exhibition, 18-22 June 2012, Milan, Italy.
- [34] J. Van herle, Y. Membrez, O. Bucheli, Biogas as a fuel source for SOFC co-generators, *Journal of Power Sources* 127 (2004) 300–312.
- [35] Y. Zhao, C. Xia, L. Jia, Z. Wang, H. Li, J. Yu, Y. Li, Recent progress on solid oxide fuel cell: Lowering temperature and utilizing non-hydrogen fuels, *International Journal of Hydrogen Energy* 38 (2013) 16498-16517.
- [36] F. Joensen, J. R. Rostrup-Nielsen. Conversion of hydrocarbons and alcohols for fuel cells, *Journal of Power Sources* 105 (2002) 195-201.
- [37] E. Bocci, A. Di Carlo, S. J. McPhail, K. Gallucci, P.U. Foscolo, M. Moneti, M. Villarini, M. Carlini, Biomass to fuel cells state of the art: A review of the most innovative technology solutions, *International Journal of Hydrogen Energy* 39 (36) (2014) 21876-21895.
- [38] Y. Matsuzaki, I. Yasuda, The poisoning effect of sulfur-containing impurity gas on a SOFC anode: Part I. Dependence on temperature, time, and impurity concentration, *Solid State Ionics* 132 (2000) 261–269.
- [39] P.V. Aravind, W. de Jong, Evaluation of high temperature gas cleaning options for biomass gasification product gas for solid oxide fuel cells, *Progress in Energy and Combustion Science* 38 (2012) 737-764.
- [40] J. P. Trembly, A. I. Marquez, T. R. Ohrn, D. J. Bayless, Effects of coal syngas and H₂S on the performance of solid oxide fuel cells: Single-cell tests, *Journal of Power Sources* 158 (2006) 263–273.
- [41] J.P. Trembly, R.S. Gemmen, D.J. Bayless, The effect of coal syngas containing HCl on the performance of solid oxide fuel cells: investigations into the effect of operational temperature and HCl concentration, *Journal of Power Sources* 169 (2007) 347-354.
- [42] K. Haga, S. Adachi, Y. Shiratori, K. Itoh, K. Sasaki, Poisoning of SOFC anodes by various fuel impurities, *Solid State Ionics* 179 (2008) 1427–1431.
- [43] F. N. Cayan, M. Zhi, S. R. Pakalapati, I. Celik, N. Wu, R. Gemmen, Effect of coal impurities on anodes of solid oxide fuel cells, *Journal of Power Sources* 185 (2008) 595–602.
- [44] P.C.A. Bergman, S.V.B. van Paasen, H. Boerrigter, The novel “OLGA” technology for complete tar removal from biomass producer gas, in: *Pyrolysis and Gasification of Biomass and Waste*, Expert Meeting, Strassbourg, France, 2002.
- [45] D.J. Stevens, *Hot Gas Conditioning: Recent Progress with Larger-scale Biomass Gasification Systems*, NREL/SR-510-29952, 2001.
- [46] M. Liu, P.V. Aravind, The fate of tars under solid oxide fuel cell conditions: A review, *Applied Thermal Engineering* 70 (2014) 687-693.
- [47] M. Liu, A. van der Kleij, A.H.M. Verkooijen, P.V. Aravind, An experimental study of the interaction between tar and SOFCs with Ni/GDC anodes, *Applied Energy* 108 (2013) 149–157.
- [48] E. Lorente, M. Millan, N.P. Brandon, Use of gasification syngas in SOFC: Impact of real tar on anode materials, *International Journal of Hydrogen Energy*, 37 (2012) 7271-7278.
- [49] J. Mermelstein, M. Millan, N.P. Brandon, The interaction of biomass gasification syngas components with tar in a solid oxide fuel cell and operational conditions to mitigate carbon deposition on nickel-gadolinium doped ceria anodes, *Journal of Power Sources* 196(11) (2011) 5027–5034.
- [50] S. J. McPhail, A. Aarva, H. Devianto, R. Bove, A. Moreno, SOFC and MCFC: Commonalities and opportunities for integrated research, *International Journal of Hydrogen Energy*, 36 (2011) 10337-10345.
- [51] R. Jain, B. Mandal. Studies on Ideal and Actual Efficiency of Solar Polymer Electrolyte Fuel Cell.
- [52] A. Lasia, *Electrochemical Impedance Spectroscopy and Its Applications*, *Modern Aspects of Electrochemistry*, B. E. Conway, J. Bockris, and R.E. White, Edts., Kluwer Academic/Plenum Publishers, New York, Vol. 32 (1999).

-
- ^[53] E. Barsoukov, J. R. Macdonald, *Impedance Spectroscopy Theory, Experiment, and Applications*, Second Edition, John Wiley & Sons, Inc., Hoboken, New Jersey (2005).
- ^[54] C. Gabrielli, *Identification of Electrochemical Processes by Frequency Response Analysis*, Technical Report number 004/83 (1998).
- ^[55] Q. Huang, R. Hui, B. Wang, J. Zhang, A review of AC impedance modeling and validation in SOFC diagnosis, *Electrochimica Acta* 52 (2007) 8144–8164.
- ^[56] N. Wagner, W. Schnurnberger, B. Müller, M. Lang, Electrochemical impedance spectra of solid-oxide fuel cells and polymer membrane fuel cells, *Electrochimica Acta* 43 (24) (1998) 3785–3793.
- ^[57] J. Nielsen, J. Hjelm, Impedance of SOFC electrodes: A review and a comprehensive case study on the impedance of LSM:YSZ cathodes, *Electrochimica Acta* 115 (2014) 31–45.
- ^[58] H. Schichlein, A. C. Müller, M. Voigts, A. Krügel, E. Ivers-Tiffée, Deconvolution of electrochemical impedance spectra for the identification of electrode reaction mechanisms in solid oxide fuel cells, *Journal of Applied Electrochemistry* 32 (2002) 875–882.
- ^[59] B. A. Boukamp, A linear Kronig-Kramers transform test for immittance data validation, *Journal of Electrochemical Society* 142 (6) (1995) 1885–1894.
- ^[60] B. A. Boukamp, Electrochemical impedance spectroscopy in solid state ionics: recent advances, *Solid State Ionics* 169 (2004) 65–73.
- ^[61] A. N. Tikhonov, V. Y. Arsenin, *Solutions of Ill-posed Problems*, J. Wiley, New York, 1977.
- ^[62] C. W. Groetsch, *The Theory of Tikhonov Regularization for Fredholm Equations for the First Kind*, Pitman, London, 1984.
- ^[63] D. Calvetti, S. Morigi, L. Reichel, F. Sgallari, Tikhonov regularization and the L-curve for large discrete ill-posed problems, *Journal of Computational and Applied Mathematics* 123 (2000) 423–446.
- ^[64] A. Leonide, V. Sonn, A. Weber, E. Ivers-Tiffée, Evaluation and Modeling of the Cell Resistance in Anode-Supported Solid Oxide Fuel Cells, *Journal of The Electrochemical Society*, 155 (1) (2008) B36–B41.
- ^[65] C. Boigues Muñoz, D. Pumiglia, S. J. McPhail, D. Montinaro, G. Comodi, G. Santori, M. Carlini, F. Polonara, More accurate macro-models of solid oxide fuel cells through electrochemical and microstructural parameter estimation - Part I: Experimentation, *Journal of Power Sources* 294 (2015) 658–668.
- ^[66] A. Kromp, A. Leonide, A. Weber, E. Ivers-Tiffée, Electrochemical Analysis of Reformate-Fuelled Anode Supported SOFC, *Journal of The Electrochemical Society*, 158 (8) (2011) B980–B986.
- ^[67] A. L. Smirnova, K. R. Ellwood, G. M. Crosbie, Application of Fourier-Based Transforms to Impedance Spectra of Small-Diameter Tubular Solid Oxide Fuel Cells, *Journal of The Electrochemical Society*, 148 (6) (2001) A610–A615.
- ^[68] C. Endler-Schuck, A. Leonide, A. Weber, S. Uhlenbruck, F. Tietz, E. Ivers-Tiffée, Performance analysis of mixed ionic–electronic conducting cathodes in anode supported cells, *Journal of Power Sources* 196 (2011) 7257–7262.
- ^[69] C. Boigues-Muñoz, D. Pumiglia, F. Santoni, S. J. McPhail, G. Comodi, M. Carlini, Performance Degradation Prediction of a Low-Temperature SOFC via Impedance Spectroscopy and CFD Modelling, *ECS Transactions*, 68 (1) (2015) 2227–2235.
- ^[70] J. R. Selman, Y. P. Len, Application of AC impedance in fuel cell research and development, *Electrochimica Acta*, 38 (14) (1993) 2063–2073.
- ^[71] Zview for Windows. Scribner Associates Inc.
- ^[72] D. R. Franceschetti, J. R. MacDonal, *Electrode Kinetics, Equivalent Circuits, and System Characterization: Small-Signal Conditions*, *Journal of Electroanalytical Chemistry* 82 (1977) 271–301.
- ^[73] J-B. Jorcin, M.E. Orazem, N. Pébère, B. Tribollet, CPE analysis by local electrochemical impedance spectroscopy, *Electrochimica Acta* 51 (2006) 1473–1479.
- ^[74] H. Schichlein, *Experimentelle Modellbildung für die Hochtemperatur-Brennstoffzelle SOFC*, ph.D. Thesis, Universität Karlsruhe (TH), Verlag Mainz, Aachen (2003).
- ^[75] D. R. Franceschetti, J. R. MacDonal, R.P. Buck, Interpretation of Finite-Length-Warburg-Type Impedances in Supported and Unsupported Electrochemical Cells with Kinetically Reversible Electrodes. *Journal of Electrochemical Society* 138 (5) (1991) 1368–1371.
- ^[76] A. Leonide, *SOFC Modelling and Parameter Identification by Means of Impedance Spectroscopy*, PhD Thesis, KIT Scientific Publishing (2010).
- ^[77] R. Barfod, M. Mogensen, T. Klemmense, A. Hagen, Y.L. Liu, P.V. Hendriksen, Detailed Characterization of Anode-Supported SOFCs by Impedance Spectroscopy, *Journal of the Electrochemical Society* 154 (4) (2007) B371–B378.
- ^[78] M. Lang, C. Auer, A. Eismann, P. Szabo, N. Wagner, Investigation of solid oxide fuel cell short stacks for mobile applications by electrochemical impedance spectroscopy, *Electrochimica Acta*, 53 (2008) 7509–7513.

-
- ^[79] A. Kromp, Model-based Interpretation of the Performance and Degradation of Reformate Fueled Solid Oxide Fuel Cells, PhD Thesis, KIT Scientific Publishing (2013).
- ^[80] SOFC Single Cell Performance and Endurance Test Modules, Test Modules TM SOFC 01-04LD/ 05-08HD. (<http://iet.jrc.ec.europa.eu/fuel-cells/downloads-0>).
- ^[81] H. Zhu, A. Kromp, A. Leonide, E. Ivers-Tiffée, O. Deutschmann, R. J. Kee, A Model-Based Interpretation of the Influence of Anode Surface Chemistry on Solid Oxide Fuel Cell Electrochemical Impedance Spectra, *Journal of The Electrochemical Society* 159 (7) (2012) F255-F266.
- ^[82] A. Leonide, Y. Apel, E. Ivers-Tiffée, SOFC Modeling and Parameter Identification by means of Impedance Spectroscopy, *ECS Transactions*, 19 (20) (2009) 81-109.
- ^[83] V. Sonn, A. Leonide, E. Ivers-Tiffée, Combined Deconvolution and CNLS Fitting Approach Applied on the Impedance Response of Technical Ni_{0.8}YSZ Cermet Electrodes, *Journal of The Electrochemical Society*, 155 (7) (2008) B675-B679.
- ^[84] S. Primdahl, and M. Mogensen, Gas Diffusion Impedance in Characterization of Solid Oxide Fuel Cell Anodes, *Journal of The Electrochemical Society*, 146 (8) (1999) 2827-2833.
- ^[85] A. Leonide, S. Ngo Dinh, A. Weber, E. Ivers-Tiffée, Performance limiting factors in anode supported SOFC, in: R. Steinberger-Wilckens, U. Bossel (Eds.), *Proceedings of the 8th European Solid Oxide Fuel Cell Forum* (2008) A0501.
- ^[86] A. Kromp, A. Leonide, A. Weber, E. Ivers-Tiffée, Hydrogen Oxidation Kinetics in Reformate-Fuelled Anode Supported SOFC, *ECS Transactions*, 35 (1) (2011) 665-678.
- ^[87] A. Leonide, S. Hansmann, E. Ivers-Tiffée, A 0-Dimensional Stationary Model for Anode-Supported Solid Oxide Fuel Cells, *ECS Transactions*, 28 (11) (2008) 341-346.
- ^[88] P. Costamagna, K. Honegger, Modeling of solid oxide heat exchanger integrated stacks and simulation at high fuel utilization, *Journal of Electrochemical Society*, 145 (11) (1998) 3995-4007.
- ^[89] S. Campanari, P. Iora, Definition and sensitivity analysis of a finite volume SOFC model for a tubular cell geometry, *Journal of Power Sources*, 132 (2004) 113-126.
- ^[90] R. Suwanwarangkul, E. Croiset, M.W. Fowler, P.L. Douglas, E. Entchev, M.A. Douglas, Performance comparison of Fick's, dusty-gas and Stefan–Maxwell models to predict the concentration overpotential of a SOFC anode, *Journal of Power Sources* 122 (2003) 9–18.
- ^[91] A. Hagen, R. Barfod, P. V. Hendriksen, Y. L. Liu, S. Ramousse, Degradation of Anode Supported SOFCs as a Function of Temperature and Current Load, *Journal of The Electrochemical Society*, 153 (6) (2006) A1165-A1171.
- ^[92] D. Simwonis, F. Tietz, D. Stöver, Nickel coarsening in annealed Ni/8YSZ anode substrates for solid oxide fuel cells, *Solid State Ionics* 132 (2000) 241–251.
- ^[93] S. P. Simner, M. D. Anderson, M. H. Engelhard, J. W. Stevenson, Degradation Mechanisms of La–Sr–Co–Fe–O₃ SOFC Cathodes, *Electrochemical and Solid-State Letters*, 9 (10) (2006) A478-A481.
- ^[94] A. Mai, M. Becker, W. Assenmacher, F. Tietz, D. Hathiramani, E. Ivers-Tiffée, D. Stöver, W. Mader, Time-dependent performance of mixed-conducting SOFC cathodes, *Solid State Ionics* 177 (2006) 1965–1968.
- ^[95] D. Singh, E. Hernandez-Pacheco, P. N. Hutton, N. Patel, M. D. Mann, Carbon deposition in an SOFC fueled by tar-laden biomass gas: a thermodynamic analysis, *Journal of Power Sources* 142 (2005) 194–199.
- ^[96] T. Namioka, T. Naruse, R. Yamane, Behavior and mechanisms of Ni/ScSZ cermet anode deterioration by trace tar in wood gas in a solid oxide fuel cell, *International Journal of Hydrogen Energy* 36 (2011) 5581-5588.
- ^[97] R. Coll, J. Salvadó, X. Farriol, D. Montané, Steam reforming model compounds of biomass gasification tars: conversion at different operating conditions and tendency towards coke formation, *Fuel Processing Technology* 74 (2001) 19-31.
- ^[98] ICPDS.ICDD, PCPDF-WIN Version 2.01, 1998.
- ^[99] M. Yashima, K. Ohtake, M. Kakihana, H. Arashi, M. Yoshimura, Determination of tetragonal-cubic phase boundary of Zr_{1-x}R_xO_{2-x/2} (R = Nd, Sm, Y, Er and Yb) by Raman scattering, *Journal of Physics and Chemistry of Solids* 7 (1996) 17-24.
- ^[100] T. Hirata, E. Asari, M. Kitajima, Infrared and Raman Spectroscopic Studies of ZrO₂ Polymorphs Doped with Y₂O₃ or CeO₂, *Journal of Solid State Chemistry* 110 (1994) 201-207.
- ^[101] Y. Repelin, C. Proust, E. Husson, J. M. Beny, Vibrational Spectroscopy of the C-Form of Yttrium Sesquioxide, *Journal of Solid State Chemistry* 118 (1995) 163-169.
- ^[102] N. Mironova-Ulmane, A. Kuzmin, I. Steins, J. Grabis, I. Sildos, M. Pärs, Raman scattering in nanosized nickel oxide NiO, *Journal of Physics: Conference Series* 93 (2007) 012039.
- ^[103] R.H.J. Hannink, P.M. Kelly, B.C. Muddle, Transformation Toughening in Zirconia-Containing Ceramics, *Journal of American Ceramic Society*, 83 (2000) 461–487.

^[104] N. Simha, L. Truskinovsky, Shear induced transformation toughening in ceramics. *Acta Metallurgica et Materialia*, 42 (1994) 3827–3836.

^[105] W. G. Bessler, S. Gewies, C. Willich, G. Schiller, K. A. Friedrich, Spatial Distribution of Electrochemical Performance in a Segmented SOFC: A Combined Modeling and Experimental Study *Fuel Cells* 10, 3 (2010).